Gas phase cluster aggregation and its application to the deposition of functional thin films

Dissertation

zur Erlangung des akademischen Grades
Doktor der Naturwissenschaften
(Dr. rer. nat.)
der Technischen Fakultät
der Christian-Albrechts-Universität zu Kiel

vorgelegt von
Tilo Peter

Kiel 2013

1. Gutachter	Prof. Dr. Franz Faupel
2. Gutachter	Prof. Dr. Holger Kersten
Datum der mündlichen Prüfung	31. Mai 2013

In memory of a friend, scientist, my tutor

Dr. Vladimir Zaporojtchenko

Kurzfassung

In dieser Arbeit werden mehrere Aspekte der Gasphasenclusteraggregation und ihrer Anwendungen untersucht. In dieser Technik wird mittels Magnetronsputtern eine hohe Dichte von einzelnen Atomen in einer Gasatmosphäre erzeugt. Diese Atome bilden Cluster, die mit einem Gasstrom zu einer Düse getragen werden. Hinter der Düse bildet sich nun ein fokussierter Clusterstrahl, der zur Probenherstellung genutzt werden kann.

Im ersten Teil wird ein System zu Abscheidung von Nanoclustern und Kompositmaterialien konstruiert. Es basiert auf einem kommerziellen Magnetron und nutzt das Prinzip üblicher Gasaggregationsquellen (GAS), allerdings besitzt es keine Düse. Dieses spezielle Design erlaubt es in-situ-Plasmadiagnostik zu nutzen. Als Material für die Clusterherstellung wird Silber verwendet. Es werden eine Vielzahl von Untersuchungen durchgeführt, um die genauen Prozesse während der Gasphasenclusteraggregation besser zu verstehen. Dazu werden Experimente mit in-situ-Diagnostik durchgeführt und Proben abgeschieden, deren Strukutr und Zusammensetzung analysiert wird.

Zur Herstellung von Kompositschichten wird ein Monomer, Hexamethyldisiloxan (HMDSO), zur Plasmapolymerisation in das Magnetronplasma eingespritzt. Dadurch wächst gleichzeitig zu der Clusterabscheidung ein Polymer auf dem Substrat auf. Die Experimente an diesem System beschäftigen sich insbesondere mit der Wechselwirkung zwischen diesen beiden Abscheidungsprozessen in dem Magnetron.

Im zweiten Teil der Arbeit wird ein weiteres Abscheidungssystem entwickelt und konstruiert, das auf einer geschlossenen GAS basiert. Im Unterschied zum ersten System werden die beiden Prozesse in separaten Vakuumbereichen durchgeführt und können weitgehend unabhängig voneinander gesteuert werden. Die Cluster werden unter anderem mit einem Massenspektrometers und einem Systems zur elektrostatischen Ablenkung untersucht. Durch Einbettung dieser Cluster in das Polymer werden Nanokomposite abgeschieden, die besondere optische Eigenschaften aufweisen.

Im letzten Teil werden mit der neuen Quelle Titancluster abgeschieden. Dies ist nur mit einer relativ jungen Technik möglich, die auf der Zugabe von reaktiven Gas beruht. Hierbei werden die Nukleationskeime aus Titanoxid, statt purem Titan, gebildet. Durch zahlreiche Experimente wird der Mechanismus auf dem dieser Effekt basiert untersucht. Weitergehende Untersuchungen führen zu einer neuartigen Methode, bei der die Abscheidungsrate der Titancluster auf mehr als das Zwanzigfache erhöht werden kann. Dies wird durch eine gepulste, statt der üblichen konstanten, Gleichspannung für das Magnetron erreicht. Der Grund für den starken Anstieg der Abscheidungsrate scheint hierbei die verstärkte Zerstäubung von Titan-Sauerstoff-Dimeren zu sein. Abschließend werden diese Cluster zur Photokatalyse eingesetzt.

Abstract

Several aspects of gas phase cluster aggregation and its potential applications are explored in this work. In this technique, magnetron sputtering is used to create a high density of single atoms in an inert gas atmosphere. These atoms then aggregate to nanoclusters and are carried by an inert gas flow to an orifice. Behind the orifice, a directed beam of clusters is formed and can be used for sample deposition.

At first, a system for cluster and nanocomposite deposition is built. It is based on a commercial magnetron and uses the same working principle as common gas aggregation cluster sources (GAS). However, it does not use a strict laminar inert gas flow and lacks an orifice, but instead offers the possibility for plasma diagnostics. Silver is used as cluster material and numerous investigations are done to better understand the specifics in the gas phase cluster aggregation process. These experiments are done using in-situ diagnostics, such as calorimetric probes and optical emission spectroscopy, but also by analyzing deposited samples with X-ray photoelectron spectroscopy and transmission electron microscopy.

The deposition of composite materials using this system is realized by injecting a precursor for plasma polymerization into the magnetron plasma. This leads to the simultaneous growth of nanoparticles and an polymer matrix. For these experiments hexamethyldisiloxane (HMDSO) is used as a precursor for the matrix material. The investigation of this system mainly focuses on the interaction between the two deposition processes in the source.

After this, a second deposition system with a new closed GAS is developed and built. It also uses cluster aggregation and plasma polymerization as deposition processes. In comparison with the previous system, it offers independent control over these processes by placing them in two separate vacuum chambers with different gas flow control units and plasma discharges. The clusters produced by this system are characterized using electrostatic deflection and a commercial quadrupole mass spectrometer. Subsequently, it is used for the deposition of nanocomposite samples with peculiar optical properties.

Lastly, this closed GAS is used for the formation of titanium nanoclusters. This is only possible using a new technique relying on a reactive gas admission. Here, the seeds for the nanoclusters are formed from titanium and oxygen, rather than pure titanium. The underlying mechanics of this effect are studied and a basic model is found. Further study reveals a novel technique, that increases the deposition rate of the titanium nanocluster by a factor of twenty. This is done by pulsing the, otherwise continuous, DC power of the magnetron inside the GAS. The reason for this increase is the sputtering of titanium oxide dimers from the target surface. An application in photocatalysis with promising results for future development is shown for the these clusters.

Contents

List of used acronyms

au	Absorbance Units
a.u.	Arbitrary Units
CS	Cluster Source
CVD	Chemical Vapor Deposition
DC	Direct Current
EDX	Energy-Dispersive X-Ray Spectroscopy
eV	Electron Volt
FWHM	Full Width at Half Maximum
GAS	Gas Aggregation Cluster Source
HMDSO	Hexamethyldisiloxane
HV	High Vacuum
MS	Mass Spectrometer
ML	Mono Layer
OES	Optical Emission Spectroscopy
PECVD	Plasma Enhanced Chemical Vapor Deposition
PVD	Physical Vapor Deposition
QMB/QCM	Quartz Micro Balance / Quartz Crystal Monitor
QMF	Quadrupole Mass Filter
RF	Radio-Frequency
SEM	Scanning Electron Microscope
SCCM	Standard Cubic Centimeter per Minute
SPR	Surface Plasmon Resonance
TEM	Transmission Electron Microscope
TMP	Turbomolecular Pump
UHV	Ultra High Vacuum
UV-Vis	Ultra-Violet/Optical/Near-Infrared Spectroscopy
VPD	Vapor Phase Deposition
XPS	X-Ray Photoelectron Spectroscopy

List of used symbols

C	Heat capacity
c	Speed of light in vacuum
d, D	Distance, Diameter
E	Energy
f	Frequency
G	Chemical free energy
H	Enthalpy
I	Current, Intensity
k_B	Boltzmann constant
l, L	Length, Thickness
m	Mass
N	Number of atoms
n	Refractive index
$\tilde{n}$	Complex refractive index
P	Power, Pressure
q	Charge
R	Gas constant
r, R	Radius
r_w	Wigner-Seitz radius
S	Supersaturation
T	Temperature, Transmittance
t	Time
U	Voltage
v	Velocity
Z	Atomic number
α	Polarization
γ	Interfacial energy per area, Surface tension
ϵ	Dielectric constant
$\tilde{\epsilon}$	Complex dielectric constant
κ	Absorption coefficient
Φ	Gas flow into the vacuum chamber
Ω	Atomic volume

Chapter 1

Introduction

In the recent years, nanocomposite materials have gained a lot of interest in many aspects of technology. A composite material consists of two or more different known materials that are combined in a way that offers new functional properties. If one or more dimensions in this composite material have a scale in the range of 1 to 100 nm, it is considered a nanocomposite material. Due to the designable functionality this class of materials offer countless new possibilities through their novel properties.

A very old and famous use of nanocomposites is the production of colored glass in medieval times, for example for church windows. These windows were created by mixing small amounts of metal in glass, which forms nanocluster and gives the glass a characteristic coloring. Though this process was widely used, the mechanisms behind it were not understood until 1908. At this time Gustav Mie published his theory on light scattering [45], which explained one part of the puzzle: The coloring effect from small particles. Of course as science advanced in this field, many applications emerged. Today nanoclusters and nanocomposites can be found in a broad field of products, for example in medical devices [59], optical coatings and paint.

The second part however, the question about homogeneous nucleation of metals, is not completely solved until now. As Popok et al. pointed out in 2011 [57]: "For now, it can be stated that homogeneous nucleation theory still has not reached a clear understanding after about 100 years of research." The current work is a step on the way to solved this puzzle: The production of silver nanoparticles, their interaction with other materials and the resulting optical and electrical properties are the main focus. To get a better understanding of the growth mechanisms of nanoparticles, titanium is investigated under similar conditions.

Nanoparticles can be produced in a number of different ways [11]. The most common techniques use wet chemistry to form nanoparticles from a solution. Some more technologically advanced techniques require vacuum conditions, which is a considerable larger effort than the other alternatives. Nevertheless, they are very important for modern industry. These methods include evaporation and sputtering, where separate atoms are deposited on a substrate. From this expense the ability to deposit atoms in extremely precise way is gained, while minimizing contaminations at the same time. The deposited atoms may then form nanoclusters by surface aggregation, depending on the surface energy of the deposited atoms and the substrate. With this level of control, composite materials with very high concentrations of metal clusters and concentration gradients can be deposited, which would be impossible with other methods.

To free this process from the interaction with the substrate, and gain more flexibility in the choice of the materials, the technique of gas phase cluster aggregation was developed [63]. This method is based on the mentioned physical vapor deposition techniques, but here the material is not directly deposited on a substrate. It will first form nanoclusters during the flight in a controlled gas atmosphere, and afterwards the already formed nanoclusters will reach the substrate. By this the cluster formation is freed from interaction with the substrate, and allows precise control over the cluster properties, mostly independent of the used substrate.

One technological interesting example is the combination of metal nanoparticles in a polymer matrix. Depending on the desired polymer, different deposition methods have to be employed. For the creation of nanocomposite materials, physical vapor deposition in vacuum is the most suitable way. It allows simultaneous deposition of two materials onto one substrate, creating a nanocomposite sample. In this case, the creation of a nanocomposite maybe easy, but it offers only a very limited control on the exact structure of the composite. Again by diffusion and aggregation, which mostly depend on the material combination, nanoparticles may or may not be formed, and there is little room to influence this. At this point, nanoclusters grown in the gas phase offer an improvement, as their size and concentration can easily be controlled independent of each other, and also independent of the substrate material. This is true even for cases where the atomic metal may have a high diffusivity, as the mobility of nanoclusters consisting of thousands of atoms is much lower.

With this method, a whole class of new composite materials, which was unavailable before [80], is now possible to be produced. Of course a major point for making this technique attractive for industry, is to understand the processes during the deposition. In a normal gas aggregation nanocluster source, it is hard to investigate these processes. The reason for this is, that the whole cluster growth process happens in a closed device, that allows little intrusion. Therefore, a model system was built in this work, that combines the nanoparticle and polymer growth in one plasma. With this system, it is possible to create nanocomposite samples and monitor the plasma processes at the same time. Using optical emission spectroscopy and thermal probe measurements, the polymer growth and the interaction between metal nanoclusters and polymer could be studied. However this system is limited in regard to the independent control over the metal clusters properties, metal concentration, matrix composition, and matrix structure.

To further study the deposition of nanocomposite samples, a second deposition system was built. This consists of a gas aggregation cluster source that produces the nanoclusters separately. The nanoclusters are then deposited as a beam into a secondary plasma, in which a polymer matrix is grown. Matrix growth is done by plasma polymerization of hexamethyldisiloxane (HMDSO), which yields a $\mathrm{Si_XO_YC_ZH}$-polymer. This setup allows better control over the clusters properties, metal concentration, and at the same time matrix composition.

At first the two parts of the deposition system were tested and characterized individually. First experiments of the newly designed Cluster Source focused on deposition Silver nanoclusters, in order to avoid oxidation and other chemical effects. Since the principle for this source was already known in the literature, only characterization and calibration was needed for silver. plasma polymerization of HMDSO was not studied in detail, because it is an already established and well known technique.

In the next step, the build up deposition system was used to create nanocomposites from silver clusters and the $\mathrm{Si_XO_YC_ZH}$-polymer matrix. Since both deposition techniques were now already tested and employed, the focus was put onto the interactions between both methods. As an example of possible applications, samples with varying optical properties were deposited and analyzed.

Further investigations using the Cluster Source were done using titanium, which was sputtered as cluster material. Using an additional flux of oxygen gas, chemical driven cluster growth was observed. Using this new concept of gas phase cluster aggregation, unusual high deposition rates could be achieved. Employing pulsed DC power for sputtering, this could even be enhanced by more than an order of magnitude, giving rise to before unknown extremely high cluster deposition rates. The titanium oxide cluster-films that were created this way, proved to be interesting for applications in photocatalysis, which were investigated subsequently.

These investigations were done in a joint project with Prof. Holger Kersten from the Institute for Experimental and Applied Physics of the Kiel University. The project was part of the Collaborative Research Center Transregio 24 *Fundamentals of Complex Plasmas*.

Chapter 2

Theory

In this chapter the underlying theory of this work is discussed. It is divided in four main parts: The first part deals with the physics of thin films, their growth and properties. The second part is about the different deposition techniques, that were employed in this work. This part includes a detailed discussion about the nanoparticle growth in the gas phase, which was the center of this work. And the last two parts are dealing with analytical methods for sample characterization and in-situ methods for process monitoring, which were important for this work.

2.1 Thin Film Properties

Nanoscale materials can exhibit extraordinary properties in comparison to their behavior in the bulk. The main reasons for this, are the extremely high surface to volume ratio of this materials, and the importance of atomic behavior and quantum effects. This part will focus on thin film growth and optical properties of nanoparticles. As this is well established knowledge, most of the following was taken from textbooks and can be found there in greater detail [51, 68].

2.1.1 Thin Film Growth

The growth of a thin film with dimensions in the nanometer scale has to be treated differently from the case of bulk materials. In thin film deposition, material is deposited atom by atom or in our special case nanocluster by nanocluster. This means that diffusion and chemical bonding govern the structure of the whole material.

If a material is deposited on a substrate surface, three different growth modes can be differentiated. These depend on the surface tension γ_s of the substrate, γ_f of the film and γ_i of the interface between substrate and film. If

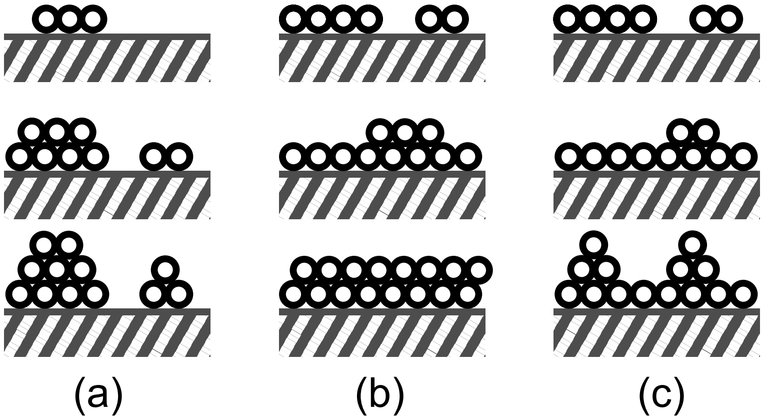

FIG. 2.1: Comparison of the three growth modes of thin films: (a) Island (Volmer-Weber) growth, (b) layer-by-layer (Frank-van der Merwe) growth, (c) crossover (Stranski-Krastanov) growth.

$\gamma_i \approx \gamma_f + \gamma_s$ or $\gamma_i > \gamma_f + \gamma_s$ (Fig. 2.1(a)), the material will prefer to grow islands, or clusters, which is commonly called Volmer-Weber growth. However if $\gamma_i + \gamma_f < \gamma_s$ (Fig. 2.1(b)) is true, the material will grow layer-by-layer, which is know as Frank-van der Merwe growth. At the border of these two cases lies Stranski-Krastanov growth, which starts with layer-by-layer growth, but changes to island growth after some layers (Fig. 2.1(c)). This happens due to change in the crystalline structure of the film while growing: The lattice of the newly deposited material does not fit on the substrate it is deposited on and thus has a changed lattice constant. After some layers, the lattice constant relaxes to the equilibrium value and thus changes the surface of the material. At one point, the surface tension will have changed enough for newly deposited material to continue to grow as islands. When noble metal atoms are deposited on a polymer surface they will usually follow Volmer-Weber growth. This is the base of creating nanocomposite materials with vacuum deposition techniques, by depositing the metal phase atom by atom and let it aggregate on or in the matrix. The main disadvantage lies in the high dependency on the used materials, as their surface tension decide the growth mode.

2.1.2 Homogeneous Nucleation

The base of all nanocluster formation that is used in this work is homogeneous nucleation. Homogeneous nucleation happens in a supersaturated vapor, a vapor with a pressure higher than the vapor pressure of the given material. At this point, a solid or liquid phase will form. This can be modeled by considering homogeneous solid spheres that can nucleate to spheres with the joined volume. Such a process leads to a reduction of the chemical free energy by

$$4\pi r^3/3\,\Delta G_V\ , \tag{2.1.1}$$

where ΔG_V is the change in chemical free energy per volume. Generally, the change in free energy of a reaction

$$aA \rightarrow bB \tag{2.1.2}$$

can be written as

$$\Delta G = bG_B - aG_A\ , \tag{2.1.3}$$

where a and b are the stoichiometric coefficients. The free energy can be expressed as

$$G_i = G_i^0 + RT\ \ln\ a_i\ , \tag{2.1.4}$$

where R is the gas constant and G_i^0 is the free energy of the species in the standard state at $298\,K$ and 1 atmosphere. The activity a_i is an effective thermodynamic concentration: It reflects the change in free energy of the species when it is not in its standard state. Combining these yields:

$$\Delta G = \Delta G^0 + RT\,ln\,\frac{a_B^b}{a_A^a}\ , \tag{2.1.5}$$

where

$$\Delta G^0 = bG_B^0 - aG_A^0\ . \tag{2.1.6}$$

In equilibrium $\Delta G = 0$ must be true, which leads to:

$$0 = \Delta G^0 + RT\ \left(\frac{a_{B(eq)}^b}{a_{A(eq)}^a}\right) \tag{2.1.7}$$

For the case of homogeneous nucleation, the reaction is from vapor (v) to solid (s). Using this the free energy per volume, ΔG_V can be expressed as:

$$\Delta G_V = \frac{k_B T}{\Omega}\ \ln\ \frac{P_S}{P_V} = -\frac{k_B T}{\Omega}\ \ln\ \frac{P_V}{P_S} \tag{2.1.8}$$

Here, P_V is the pressure of the vapor, P_S is the pressure above the solid, and Ω is the atomic volume. Defining a supersaturation $S = (P_V - P_S)/P_S$, this can written as:

$$\Delta G_V = -k_B T/\Omega\ \ln\left(1 + S\right) \tag{2.1.9}$$

This shows that without supersaturation ($S = 0$), no nucleation is possible ($\Delta G_V = 0$). In the case of supersaturation ($P_V > P_S \Rightarrow S > 0$) ΔG_V becomes negative, which allows nucleation. Another effect of nucleation is the change

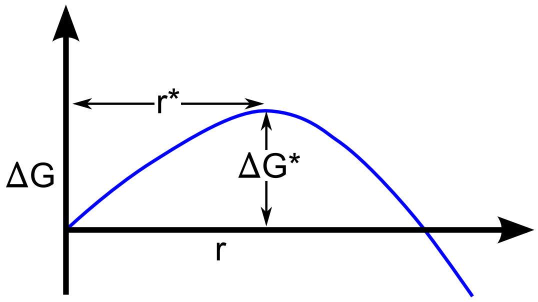

FIG. 2.2: Energy schematic of homogeneous nucleation: The change in free energy is plotted against the cluster radius. r^* is the critical radius after which nucleation occurs, ΔG^* is the corresponding energy barrier to create such a cluster.

in surface area: The free energy of the system is given by $4\pi r^2\gamma$, where γ is the interfacial energy per area. Thus the free energy is given by:

$$\Delta G = \frac{4}{3}\pi r^3 \Delta G_V + 4\pi r^2 \gamma \tag{2.1.10}$$

The minimum of ΔG with respect to r is given by the critical radius

$$r^* = -2\,\gamma / \Delta G_V\ , \tag{2.1.11}$$

which leads to the critical free energy barrier

$$\Delta G^* = 16\,\pi\gamma^3 / 3(\Delta G_V)^2\ . \tag{2.1.12}$$

These two quantities are plotted against each other in Fig. 2.2. From this graph we can get the general understanding of this process: If a formed cluster is smaller than r^*, it will be unstable and lose atoms. But if the radius is larger than r^*, it will be large enough to be stable and grow by collecting more atoms. In this work, mainly silver was used, which has a surface tension of 0.86 J/m [12] and an atomic volume of $1.25\ \cdot 10^{-29}\,\mathrm{m}^3$ [26]. By accepting ambient temperature of 298 K and a supersaturation of 0.1, the critical radius can be calculated to

$$\begin{aligned} r^* =&\ -2\,\gamma / \{-k_B T/\Omega\ \ln(1+S)\} && (2.1.13)\\ =&\ 2 \cdot 0.86\ \mathrm{J/m}\,/(1.38 \cdot 10^{-23}\,\mathrm{J/K} \\ &\quad \cdot 298\,\mathrm{K}\,/\{(1.25 \cdot 10^{-29}\,\mathrm{m}^3)\ \ln(1+0.1)\} && (2.1.14)\\ =&\ 54.9\,\mathrm{nm} && (2.1.15) \end{aligned}$$

Upon increasing the supersaturation to $S = 0.5$, the stable radius decreases drastically:

$$r^* = 12.9\,\mathrm{nm} \tag{2.1.16}$$

This calculation is the basis of the gas phase cluster aggregation technique that was used in this work. Even at ambient temperature it is possible to grow nano-sized silver clusters, if a high supersaturation is reached.

2.1.3 Optical Properties: Surface Plasmon Resonance

The optical properties of a material can be described by its complex dielectric constant [39]

$$\tilde{\epsilon} = \epsilon_1 + i\epsilon_2 \tag{2.1.17}$$

and the complex refractive index

$$\tilde{n} = n + i\kappa \,. \tag{2.1.18}$$

Here, κ is the absorption coefficient and n the refractive index. Since the complex dielectric constant and the complex refractive index vary with wavelength respectively frequency, it should be more precisely denoted as the dielectric function $\tilde{\epsilon}(\nu)$ and the refractive function $\tilde{n}(\nu)$. This is implicitly used and will be shortened to $\tilde{\epsilon}$ and $\tilde{n}$ in this section. The refractive index n is defined as the ratio between the speed of light in vacuum c and in a material v:

$$n = \frac{c}{v} \tag{2.1.19}$$

The complex refractive index can be expressed by the dielectric constant:

$$\tilde{n}^2 = \tilde{\epsilon} \tag{2.1.20}$$

Thus the real and imaginary part of the complex dielectric can be described by the refractive index and the absorption coefficient:

$$\epsilon_1 = n^2 - \kappa^2 \tag{2.1.21}$$

$$\epsilon_2 = 2n\kappa \tag{2.1.22}$$

In the case of nanocomposites, which were the center of this work, the optical properties mainly depend on the metallic particles. The polymer matrix material was chosen, to have a high transmittance over a broad spectral range from UV to visible light and even near infrared.

However metallic nanoparticles exhibit an effect know as surface plasmon resonance (SPR) [17], which is schematically shown in figure 2.3. The electrons in a metallic particle can vibrate against the ions. If an electromagnetic wave with a frequency matching the eigenfrequency of this electronic vibration reaches the nanoparticle, the vibration is excited and part of the electromagnetic wave absorbed. For nanometer-sized particles made from copper, silver and gold, the frequency of this resonance is the regime of visible light. In the description of this effect any influence from Rayleigh scattering can be neglected, as the particle size is much smaller than the wavelength of visible light. Taking only dipole interaction into account, the polarization α of the metal particle with the radius R can be written as

$$\alpha = 4\pi\epsilon_0 R^3 \, \frac{\tilde{\epsilon}_{me} - \tilde{\epsilon}_{po}}{\tilde{\epsilon}_{me} + 2\tilde{\epsilon}_{po}} \,, \tag{2.1.23}$$

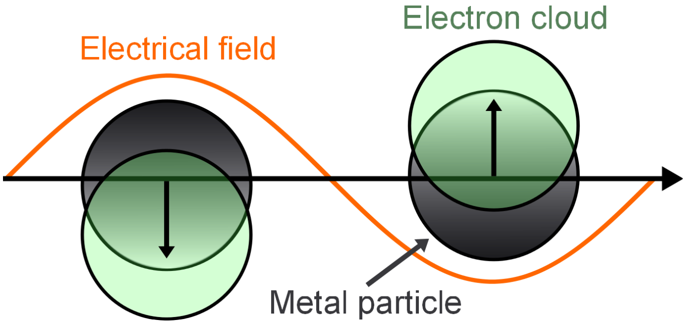

FIG. 2.3: Schematic of the surface plasmon resonance: The electrical field of an incoming electromagnetic wave drags the electrons from a metal particle and by this excites a vibration of the electrons against the the ions of the metal particle.

according to Heilmann [27]. Here $\tilde{\epsilon}_{me}$ and $\tilde{\epsilon}_{of}$ are the complex dielectric functions of the metal and the polymer respectively. As it can be seen from this, the polarization diverges, if

$$\tilde{\epsilon}_{me} + 2\tilde{\epsilon}_{po} = 0\,. \tag{2.1.24}$$

Using this equation, the position of the resonance can be predicted, if the complex dielectric functions are known. The exact frequency, however, not only depend on the material, size and shape of the particle, which is taken into account here. The resonance frequency also depends on the interaction between particles, which is controlled by the inter particle distance, and is not part of this calculation [83]. In order to take this factors also into account, the more complex Mie-theory has to be employed. Details about this approach can be found in other works [6]. Another problem in the theoretical description of metal nanoparticles is given by the fact that very small cluster with radii under 3 nm show quantum size-effects [38], which also the Mie-theory does not include. Still todays simulations are able to reproduces most of the effects observed in nanocomposites [3].

2.2 Deposition techniques

The center of this work was the development and investigation of a new method for thin film deposition. For this reason the different techniques of deposition will be discussed in this section: Plasma polymerization of HMDSO and magnetron sputtering. As this are well known methods, they will be only introduced briefly. The main focus is set on the specifics of the device and materials that were used. After the introduction of the underlying basic methods, the gas phase cluster aggregation will be presented in greater detail.

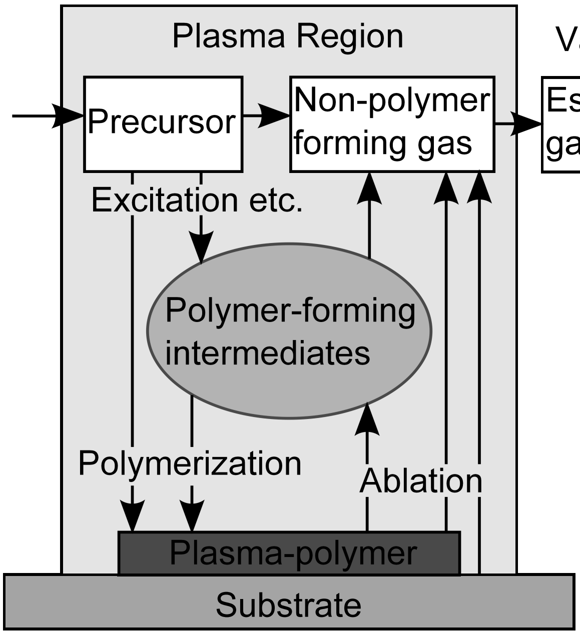

FIG. 2.4: Schematic of the processes that are involved during plasma polymerization.

2.2.1 Plasma Polymerization of HMDSO

The deposition of polymers in a low pressure plasma from a chemical inert precursor is a widespread method to create dielectric thin films. It is known as plasma polymerization. The working principle is the dissociation, ionization and excitation of a monomer precursor in a plasma, producing polymer forming intermediates. This intermediates then polymerize on a substrate, forming a highly cross-linked plasma-polymer.

The used precursors for plasma polymerization are quite complicated molecules from a plasma physics point of view. Also the different processes, that are triggered at the same time and compete for the available precursor and intermediates, are rather complex and their interaction cannot easily be modeled. Figure 2.4 shows a diagram of the processes and their interaction as described by Yasuda [85]. The main parameter influencing the processes, and by this the deposited polymer, are the pressure of the precursor and the inert gas, and the power density of the plasma that is used for activation. Typically the plasma discharge is run using capacitive coupled radio frequency (RF, 13.56 MHz[a]) power, as practically all deposited films are dielectric and thus prevent the use of DC power.

---

[a] 13.56 MHz is part of the industrial, scientific and medical (ISM) band defined by the International Telecommunication Union (ITU), which is used for applications with short range and high tolerance for interference such as heating and plasma excitation, but also data transfer in Radio-frequency identification (RFID) transponders.

When the precursor is brought into the reaction chamber, it is bombarded by photons, electrons, ions and neutrals from the plasma. As in most cases low temperature, low pressure plasmas are used for deposition, the influence from ions and neutrals on the precursor can be neglected. For most precursors UV-light and electrons are the leading cause for dissociation. By this fragments are formed, that can be molecules, atoms, ions, or radicals. Depending on the precursor and the energy density of the plasma, and thus the mean electron energy, different fragments can be formed. If the formed fragments are inert, or previously reactive fragments recombine to a stable molecule, they leave the reaction zone and are pumped out.

The reactive fragments, however, can directly polymerize on the substrate, or form further intermediate molecules that polymerize. All reactions involving intermediates can again lead to inert molecules, that leave the reaction, or they can reach the substrate. On the substrate some fragments or intermediates might directly connect to an existing branch of the growing polymer. Otherwise they will diffuse on the substrate, may still react with other fragments and intermediates, and then also react and connect to the polymer film. Of course during all steps of this deposition process dissociation, ionization, and excitation by electrons and radiation is still possible. Depending on the position of the substrate, the process is called direct or remote when the substrate is inside or outside the plasma region, respectively. In the case of a direct deposition the already grown polymer can be modified, or even ablated, by electron and ion bombardment. The highly inter-dependence of this steps in the deposition process leads to a vast variety of possible molecules, yielding a polymer thin film from which the structure of the precursor may not be recognizable.

Plasma polymerization has some major advantages over traditional wet chemical polymerization techniques. For industrial applications, one of the biggest differences involves the employed substances. In plasma polymerization only the monomer and an inert gas, for example argon, are involved, whereas wet chemical approaches rely on several other substance such as solvents, catalysts, or cleaning agents, which can be hazardous to the environment. Additionally plasma polymerization is possible for a number of precursors that can not be polymerized using wet chemistry, such as Silan SiH_4, Methan CH_4, or Ethan C_2H_6 [29]. Also for precursors, for which conventional polymerization is possible, the resulting film properties vary. Since plasma polymer films exhibit very strong cross-linking the films are denser and completely pinhole free, in contrast to traditionally deposited polymer thin films. On the other hand, plasma polymer films may contain internal stress, which can lead to delamination and cracking of films with thicknesses over 100 nm [85]. Of course, these advantages come at a price, which is mainly the actual price of machinery. As a low pressure plasma discharge is used, a vacuum system, gas flux controllers, and the discharge power supply and matching network are needed, which are an enormous investment compared

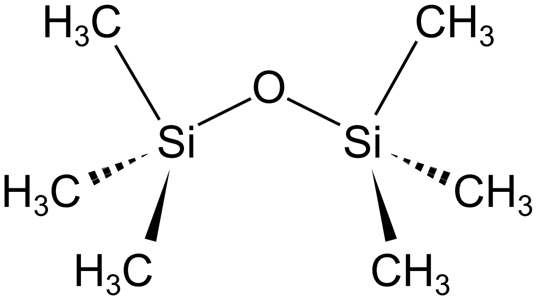

FIG. 2.5: Chemical structure of hexamethyldisiloxane (HMDSO).

with a lab for wet chemistry coating. Also the high complexity of the plasma polymerization process can pose a problem when a precisely controlled product with special properties is needed, as the influence from different outside parameters on the product can be unpredictable.

Due to this unique properties, plasma-polymers are important for several industrial applications, such as biomedicine [18], anti-fouling [13] and a wide range of microelectronics [28, 52, 73]. Another important example of plasma polymerization is the deposition of quartz-like thin films with varying concentration of hydrocarbons ($SiO_XC_YH_Z$) from siloxane monomers. This class of monomers is especially interesting because of their versatile properties, which makes them suitable for many applications. Their high relative permittivity [2, 31, 32, 66, 74] and high transparency in the optical range [15, 55, 76] qualifies them for use in electronics and optics. Also their high mechanical, thermal and chemical stability is needed in different types of barrier layers [32, 62, 64]. Another advantage of siloxanes is their easy use, as they are liquid, non-toxic, and non-explosive, but highly flammable.

One monomer of this type is hexamethyldisiloxane (HMDSO, $C_6H_{18}Si_2O$), which is a silicon-oxygen-silicon core with 3 methyl groups attached to each silicon, shown in figure 2.5. As the binding energies of the carbon-hydrogen (9 eV [26]) and the silicone-carbon (11.9 eV [26]) bindings are much lower than the binding energy of silicone-oxygen (21.3 eV [26]), the latter binding is rarely broken during plasma polymerization, and thus is directly incorporated into the deposited film [7, 50]. For this reason, properties, and the easy use, it was used in this work as model material for nanocomposite deposition. The composition of the produced $SiO_XC_YH_Z$ plasma-polymer films was investigated using XPS and EDX, both of this methods are unable to detect hydrogen. Since this was not the main focus of this work, the hydrogen content was also not determined with other methods. Models and empirical data of the hydrogen content can easily be found in the literature [16, 46, 69].

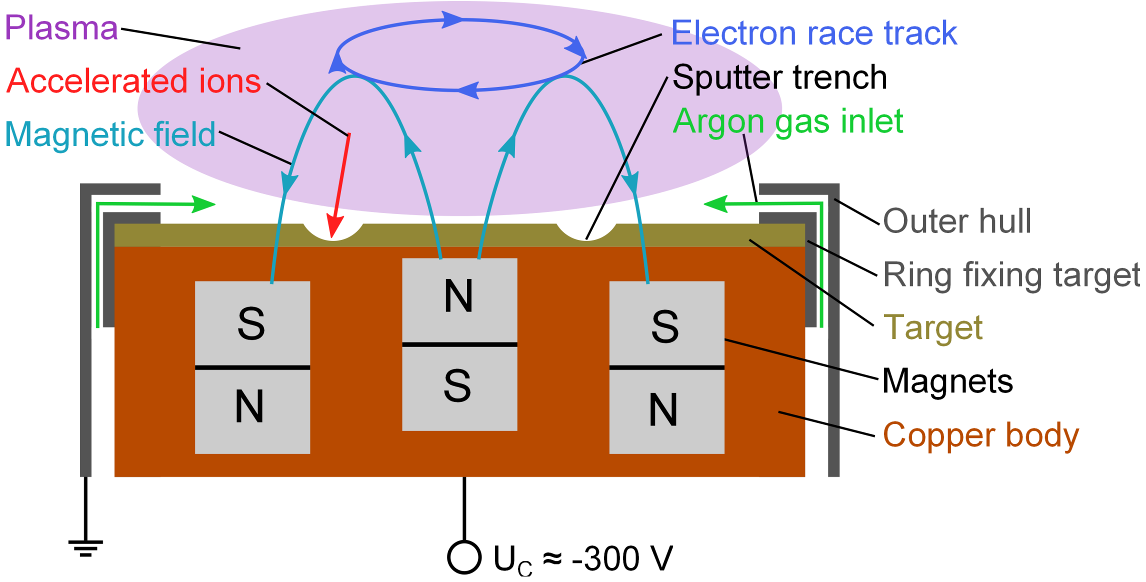

FIG. 2.6: Schematic of the magnetron type used in this work.

2.2.2 Magnetron Sputtering

Sputtering is an established and widely applied physical vapor deposition (PVD) technique for deposition of thin films. Ions are accelerated onto a target where they release atoms from the target by collisions. These atoms then travel through the vacuum chamber onto the substrate where they are deposited. Different methods can be used to generated ions, and also different geometries for the target and substrate are known. One of the main properties of sputtering for application is the high energy in the range of few electronvolts of the sputtered atoms [30] in comparison with other PVD techniques such as evaporation. In this work, a planar DC magnetron was used for sputtering, and accordingly the following discussion will not cover the alternatives. Further information and a more detailed discussion including reactive and pulsed sputtering can be found in the literature [51, 68].

In magnetron sputtering, a plasma is ignited using a noble gas, that produces ions used for sputtering. This is achieved by a negative bias voltage on the target, which is also used to accelerate the ions onto the target. A schematic of the design of the magnetron used in this work is shown in figure 2.6. This magnetron uses a flat circular target with a diameter of 50 mm and a thickness of 6 mm, to which typically a voltage of 150 to 400 V is applied for sputtering. The inert gas is led in through channels at the side of the cathode, which have a width of ≈ 1 mm, to avoid ignition of a plasma at this point. The final part of the gas channel leads the gas horizontally over the target, and has a width of 1.5 mm, to promote the discharge ignition at this point. Permanent magnets under the targets are used to generate magnetic field over the target that traps electrons in a circular drift motion, called the race track. This leads to a higher electron density, which in turn leads to a higher ion density that is available for sputtering. Now, it is possible to achieve the same ion flux using a lower inert gas pressure, reducing the number of collision of sputtered atoms in the gas phase. With this setup typically inert gas pressure down to $1 \cdot 10^{-2}$ Pa can be used. Another effect of the concentration of ion density is the inhomogeneous erosion of the target, which is the highest directly under the race track, causing a ring of erosion, called the sputter trench.

Not all energy from the impinging ions is used for the acceleration of sputtered atoms, also the target is heated up, which can cause cracks or even melting. Additionally, the permanent magnets in a magnetron have typical Curie-temperatures of $310°$ to $370°$ C and hence are sensitive to heat. To counter this, water cooling is used on the copper cathode near the magnets. In the case of a metal target, this is also enough to cool the target. As the water cooling is grounded at some point in the pump or heat exchanger, a small ion current is flowing though the water. For this reason, the water lines are built from insulating materials, because the water near the cathode is under considerable voltage. Also de-ionized water is used to minimize the leak current.

The number of atoms sputtered from the target per incoming ion is called sputtering yield, it depends on the species of ions, energy of the ions, impact angle, and the species of the target. As the sputtering process is a mechanical collision, a high ion mass is advantageous. But as the cost for pure heavy noble gases is another factor, argon is used in most cases. A rise in ion energy leads to a higher sputtering yield for energies up to 10 keV for argon. Above this value the ions are implanted deeply into the target and consequently cause less sputtering. The impact angle of the ions comes into play in interaction with the formation of the sputter trench: For a new target the mean impact angle is $0°$. When the sputter trench develops and grows, ions hit the sides of the trench at increasing angles of incidents. This causes a gradual rise in sputtering yield up to 2 times, depending on target material, and after a maximum at $\approx 70°$ a steep drop below the $0°$-value. If the ion parameters are know, the sputtering yield for a given target material can be calculated with good accuracy using simulation software [88].

Magnetron sputtering using a commercial source (ION'X 2UHV, Thin Film Consulting) and a DC power supply (MDX 500, Advanced Energy) was used for silver and titanium in this work. However a high pressure gas atmosphere was employed in order to promote cluster growth in the gas phase, instead of atom-by-atom deposition on a substrate. The next section will cover reactive sputtering, which was employed for titanium, while the details of gas phase cluster growth is the topic of the section after that.

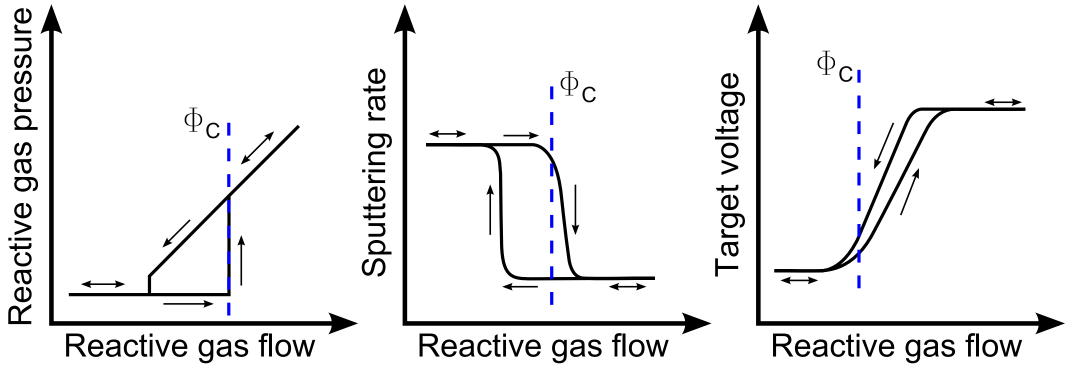

FIG. 2.7: Schematic hysteresis curves in a reactive sputtering process, for titanium/oxygen with the critical oxygen flow Φ_C [14, 51].

2.2.3 Pulsed Reactive Sputtering

Magnetron sputtering with DC power, as described in the previous section, can only effectively be used for metallic materials. Non-conducting targets would charge up positively, due to the incoming ion flux, negating the applied voltage until ions are no longer accelerated to the target. Additionally this promotes arcing, where at a highly charged spot the insulating layer suffers from electrical breakdown, and releases a lot of material in one bunch, which can lead to roughness and defects in the deposited film. To counter this, RF powered sputtering may be used to deposit non-conducting materials, such as polymers and ceramics, but at the cost of much lower sputtering rates. To overcome this issue, without compromising the high deposition rate of DC sputtering, reactive sputtering was developed. It is a standard technique for todays industry, and is for example used for the deposition of titanium oxide and aluminum nitride films [68].

In reactive sputtering, a metallic target is used, and a reactive gas flow Φ is added to the inert gas, which reacts with the metal to form a ceramic on the substrate. There are 3 regions where the reactive gas will interact with the metal: On the target with material before sputtering, in the gas phase with sputtered atoms on their way to the substrate, and on the substrate with the forming film.

The interaction with the target is most important part, as this not only helps depositing the desired ceramic, but also poisons the target by building up an insulating layer. With growing amount of reactive gas, the poisoned area of the target grows, and also its thickness increases. Because target poisoning is using up most of the reactive gas, its partial pressure in the gas phase does not increase with increasing flow at first. This state is called metallic mode, since the target is mostly conducting. Here, most of the sputtering operation still works like before, and there is enough non-poisoned area of the target to keep a high sputtering rate. Once the reactive gas flow reaches a critical value Φ_C, the sputtering rate suddenly drops sharply. In this new state, called ceramic mode, the sputtering rate is too low to clean the target, which causes wide areas to be poisoned. Since there is no free area on the target, the gas is not used up in poisoning the target anymore, thus the partial pressure rises drastically. An easy indicator for the state of the process is the target voltage. In normal operation the power supply is set to keep a constant power, because the power is roughly proportional to the sputtering rate. When ionization yields for the plasma species, the secondary electron emission yields for the ions impinging on the target, and the charge on the insulating layer change, it will have an effect on the voltage-current characteristics of the plasma and by this ultimately on the voltage. However, the change in voltage is not trivial for all materials [14]. For the case of titanium, which was used in this work, the bias voltage will rise with growing oxidation of the target. The evolution of the deposition rate, the partial pressure, and the voltage with respect to reactive gas flow are shown in figure 2.7, for the case of titanium/oxygen.

If the target is in metallic mode, the film deposited on the substrate may not be fully stoichiometric. In this case reactive gas can be adsorbed and built into it. This is another effect triggering the discussed hysteresis: With low poisoning of the target, more metallic material is sputtered can bind reactive gas on the substrate, keeping the target in metallic mode. On the other hand, when the target gets poisoned, the sputter rate drops and thus less material is deposited on the substrate, that could use up the reactive gas. This causes an even higher partial pressure of reactive gas, which in turn leads to a more severe target poisoning.

The last possibility is the interaction of reactive gas with sputtered atoms in the gas phase. This effect can be neglected in most cases of low pressure magnetron sputtering, because the mean free path for a sputtered atom for a collision with a reactive gas atom is ≈ 30 m, while the target-substrate distance is only 20 cm. It will however change drastically when the partial pressure of reactive is much higher, like it is the case in the gas aggregation source, which will be discussed in the following section.

Since this process has proven to be effective, but hard to stabilize, pulsed DC power was introduced. With this change the transition from metallic to ceramic mode is smoother, and a partly poisoned target can be sputtered more easily [8]. The key of this technique is that the target is not held at a constant voltage, but it is set to a positive bias or left floating for a short period of time. In this time, the positive charges on the poisoned part of the target attract electrons that compensate the positive charge. Another side effect is the prevention of arcs, as no charge can build up over longer periods of time. The frequency has to be chosen in a way that allows the electrons to negate the charge exactly, and thus depends on the ion and electron fluxes. Typical values for the frequency are in the range from 10 to 400 kHz. Pulsed DC sputtering

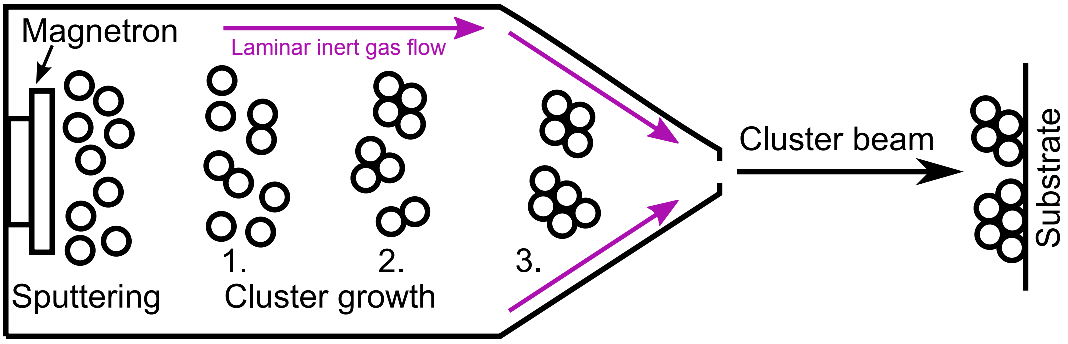

FIG. 2.8: Schematic of a GAS and the gas phase cluster aggregation process.

was realized in this work by using a switching device to pulse an otherwise continuous DC power supply.

2.2.4 Gas Phase Cluster Aggregation

Nanoclusters, or nanoparticles, are an intermediate state between single atoms, or molecules, with typical sizes of a few ångström to a few nanometers, and bulk material with dimensions of several microns. This gives them unique properties that are interesting for a wide range of applications. The production of such nanoclusters in a controlled fashion and under vacuum conditions is important for thin film technology. One way to achieve this, is the use of gas phase cluster aggregation. Here, nanoclusters are formed in the gas phase from atomic vapor, and are subsequently directed as a cluster beam onto a substrate. Such cluster sources were first reported 1980 by Sattler et al. [63], using thermal evaporation as source for metal vapor. Twelve years later Haberland et al. [24] published the design of a cluster source based on magnetron sputtering for the production of metal clusters of different sizes. Magnetron sputtering has since then been used for gas aggregation cluster sources (GAS) of different types [80].

Many designs differ in geometry and their methods for vapor generation, but the principle of cluster formation is common in all of them. The main interesting features are the deposition of the nanoclusters as a beam, which can be focused using, for example, supersonic gas expansions [54]. Another specialty of magnetron based GAS is the fact that a high amount of the produced clusters is charged, and thus can be guided or accelerated using electric fields [25].

The details of the homogeneous nucleation of metal atoms in the gas phase is not completely understood yet for this sources, however a rough models exists and current investigations aim to develop this knowledge. In the following a basic model taken from the literature [35, 67] will be discussed.

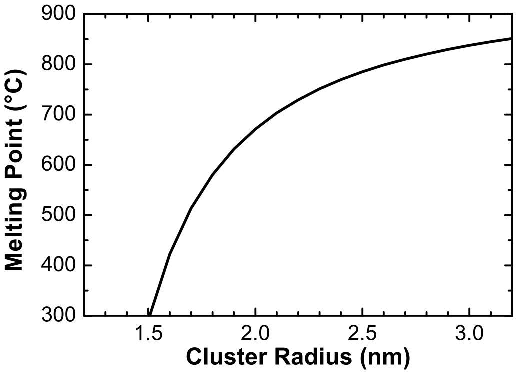

FIG. 2.9: Melting point temperature for silver nanoparticles in dependence of their radius. According to simulations by Zhao et al. [87].

Figure 2.8 shows the schematic design of such a cluster source and the cluster aggregation process. At first, a magnetron sputtering source is used to create free metal atoms. Again, mostly argon is used as sputtering gas, which also fulfills the roll of an inert carrier gas in this case. Additionally helium is used in some designs, as its high thermal conductivity can be used to help the cluster seed stabilization, and thus change the resulting cluster size distribution [23, 25, 58]. The pressure of the inert gas in the GAS is usually between 10 and 200 Pa, which leads to a thermalization of the sputtered atoms by collisions in a distance of ≈ 1 cm from the target. If the density of the atoms is high enough, they form a supersaturated vapor and start to form nanoclusters. The process of cluster formation and growth can be divided in 3 steps: Dimer formation as cluster nucleation seeds, cluster growth, and lastly cluster coagulation.

In the first step a dimer M_2 is formed from 2 free metal atoms M in a three-body collision with an inert gas atom A:

$$2M + A \rightarrow M_2 + A \tag{2.2.1}$$

The inert gas atom is mainly needed to take up the heat of condensation from the formed dimer, to stabilize it. Once a stable dimer is formed, the second step is the growth by collisions with free atoms:

$$M_n + M \rightarrow M_{n+1} \tag{2.2.2}$$

As this collision has a much higher probability than the three-body collision (equation 2.2.1), every stable dimer will grow and form a cluster. Bigger clusters are subsequently stabilized by collisions with inert gas atoms, that work as a thermal conductor from the metal clusters to the wall of the GAS. For this reason most GAS designs employ liquid nitrogen or water cooling on the wall of the GAS [25, 56]. A lower inert gas temperature will promote nucleation by a faster cooling and therefore stabilization of the clusters. At this stage, most cluster are in liquid form, because of the effect of melting point depression in nanoparticles [34, 72, 87]. Figure 2.9 shows the melting temperature for silver clusters in dependence of their radius. It can be seen, that the melting point drops significantly for clusters with small radii. With continuous cooling, the clusters solidify quickly before they reach a radius of about 2 nm.

The design of the cluster source forces the inert gas to form a laminar flow from the target to the end of the source. In this part the cluster seed formation and cluster grows continues, as the clusters and free metal atoms travel in the inert gas stream. Due to the high mass and size of clusters, they are effectively captured by collisions with the inert gas in their flow. Of course not all atoms and cluster can follow the flow and some will diffuse to the sides and stick on the wall of the GAS. With more and more atoms getting are bound into clusters, the cluster growth by single atom attachment (equation 2.2.2) diminishes. At the same time the third step of cluster formation starts: The coagulation of clusters.

$$M_n + M_m \rightarrow M_{m+n} \tag{2.2.3}$$

This process is especially effective in the last part of the GAS, where its diameter decreases and the clusters are accelerated towards the orifice. Since these processes depend on the inert gas pressure, free metal atom density and aggregation length, the amount, and size distribution of the clusters can be controlled with these parameters.

While the cluster move through the GAS during growth, they undergo collisions with ions and electrons from the magnetron plasma. This leads to ionization of clusters, and also possibly charge recombination during coagulation of clusters. The general approximation for charging of particles in a plasma is that they will charge up negative, because of the higher mobility of electrons in comparison to ions. However, in the case of the GAS, the metal atom and cluster density is too high to use this approximation. When a critical number of electrons from the plasma is bound in charged clusters, the quasi neutrality of the plasma is disrupted. The ion and electron density is much lower far away from the magnetron, where most of the cluster growth takes place. Consequently, cluster are charged positively and negatively, in both cases with most likely only single charges [35, 67].

The pressure in the deposition chamber behind the orifice has typically a pressure of under 1 Pa. Because of this, the clusters form a beam that travels linearly through the chamber. The speed of this clusters is the range of 20 to 200 m/s, depending on their size [56]. When they reach the substrate they keep their structure, because the kinetic energy of 0.2 meV per atom is small compared to the interatomic binding strength. This is called soft landing, and is the usually desired mode for cluster deposition. Like mentioned earlier, it is, however, possible to accelerated the clusters using a bias voltage, if a more dense film is needed. In addition to keeping their structure, clusters are also only weakly attached to the substrate in soft landing mode, and depending on the material of the clusters and the substrate can exhibit high diffusivity. This might be used to fill grain boundaries, or other defect sides, on the substrate, as these are usually traps for diffusing particles.

A GAS was designed and built during this work, details about it are presented in section 5.1.

2.3 Analytical techniques: Sample characterization

For the characterization of thin film samples a variety of analytic techniques can be employed. In the following sections, the methods that were used in this work will be presented.

2.3.1 Profilometry

Profilometry is a technique to determine the surface topography of a sample. The sample is scanned and the height is measured at each point, yielding a topographical map of it. Two different measuring principles are commonly used: Non-contact optical profilometers that use the reflectivity or transparency, and mechanical profilometers that use a stylus, to determine the thickness of the sample. In a mechanical profilometer the stylus is pressed down onto the sample with a constant force, following the height profile as it is moving along the sample. The main advantage of a mechanical measurement is the possibility to measure nearly all types of samples, no matter their optical properties. However, the minimum force of the profilometer is limited and can still pose a problem for very soft or instable samples, since they might get destroyed while scanning.

For the investigations done in this work a Dektak 8000 stylus profilometer from Veeco was used. The minimal possible force for this device was 0.5 mg, which was used in all measurements. The practical accuracy is in the range of a few nanometers, which is mostly limited by the roughness of the substrate and the film. To be able to measure the absolute film thickness, samples prepared for profilometry need an uncoated area on the substrate for comparison. To achieve this, either a part of the sample is covered during deposition and the cover is only removed before profilometry, or part of the sample is scratched of using a knife after deposition. The latter technique is mostly used for soft films and offers an advantage by allowing other analysis to be done beforehand, that require an undisturbed sample.

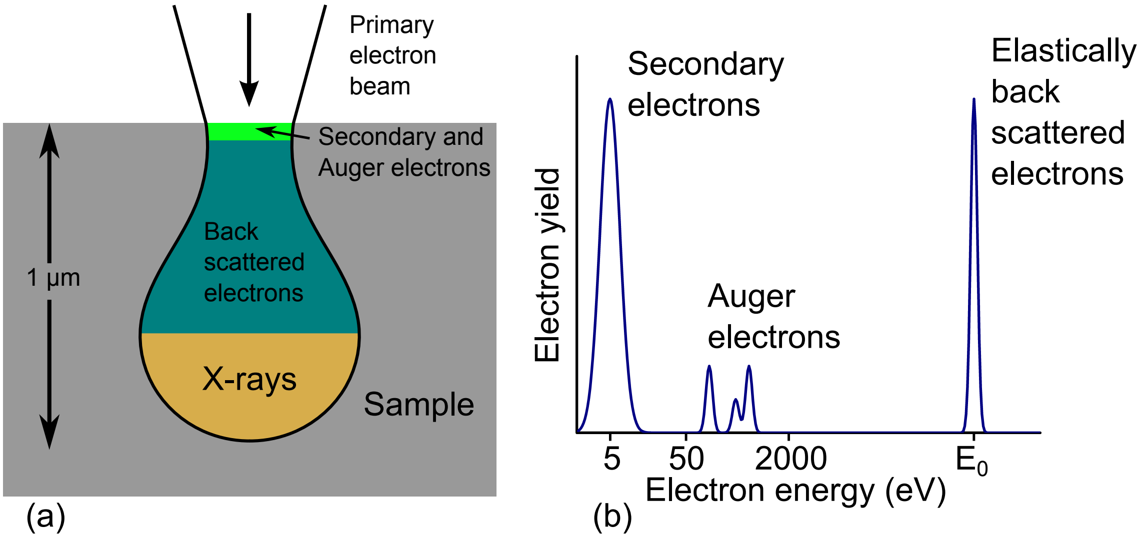

FIG. 2.10: (a) Schematic of the interaction of the primary electron beam of an SEM with the sample. (b) Resulting electron energy spectrum from the different interactions. [51]

2.3.2 Scanning Electron Microscopy (SEM)

If it is desired to get an image of a surface with resolution beyond the possibilities of traditional light microscopes, Scanning Electron Microscopy (SEM) is often employed. Here, an electron beam is produced from a cathode and accelerated to an energy between 1 and 50 keV. The beam is then focused to a fine area down to 1 nm in diameter. Now the beam is scanned across the sample, and for every single scanning point, the electrons emitted from the sample are analyzed. This electrons are created mainly by two processes: Secondary electron emission and elastic backscattering. While the primary electron beam travels through the sample, it is exciting and ionizing atoms, producing free electrons. This secondary electrons move through the sample in a random direction from the origin. Because their energy is in the order of 10 eV, their mean free path in matter is low, so only electrons from the first few atomic layers of the sample will leave it [65]. At this point the secondary electrons can be collected and analyzed using. The image that is generated by this scanning technique primarily includes information about the topography of the samples surface. The probed interaction space of the sample is given by the lateral size of the primary beam and the escape depth of the secondary electrons, thus resolutions down to 1 nm can be achieved. The detection of secondary electrons is the most common measuring mode, as it yields good resolution, without requiring an energy resolving detector. Figure 2.10 shows a schematic of the different interactions and their effective area.

The other main interaction of the primary electron beam with the sample is elastic backscattering. Because of their high energy, and thus high mean free path in the order of 1 µm, even electrons that are backscattered in the bulk of the sample can return to the surface and be detected. Since they can undergo multiple elastic scatter events on their path, the beam gets wider, the deeper it reaches into the sample. This widening effect is the ultimate limit for lateral resolution of an SEM using backscattering. Elastic backscattered electrons can be used to determine the sample chemical composition to some extend, as their intensity is a function of the atomic number Z: $I \propto \sqrt{Z}$. This dependence also leads to different penetration depths of the primary electron beam for different materials. Furthermore, the diffraction pattern of the backscattered electrons can be used to determine the crystallographic structure.

Additionally also more complicated electronic interactions can take place: Auger electrons are produced when a core-shell electron is emitted from the atom and an higher orbital electron takes its place. With the free energy from this transition a third electron from another high orbital is also emitted from the atom, the Auger electron. The kinetic energy of this electron is completely independent from the energy of the primary electron, it carries exactly the energy from the secondary electron transition. Because of this, it can be used to identify chemical species, if the electrons are collected using an energy analyzer. Since this energy is usually in the order of hundreds of eV, the escape depth for Auger electrons is between 1 and 10 nm, like secondary electrons.

Alternatively, when a core shell electron is emitted and a higher orbital electron does a transition to this shell, the free energy can be emitted as a photon. Because the energy of core levels range up to tens of keV, this emission has the form of X-Rays. The detection of this X-rays is know as energy-dispersive X-ray spectroscopy (EDX) and will be discussed in detail in section 2.3.4.

Lastly also a background of continuous X-rays originating from bremsstrahlung is excited by the impinging primary electron beam [60].

One of the drawbacks of the SEM are the effects of the electron beam on the sample: As the beam is scanned over a very small area with most interaction very close to the surface, the energy influx and thus the heating of the sample can be quite substantial. Also the secondary electron emission leaves the sample in a highly ionized state, which creates stray electric fields that deflect the primary beam and cause artifacts in the image. For this reasons samples with a high thermal and electric resistivity pose a problem. In the case of the here investigated polymer nanocomposites and titanium oxide samples this simply means the possible lateral resolution is impacted and will not reach the theoretical value of 1 nm.

In this work, measurements were done using different SEM devices, which will be mentioned in the corresponding sections.

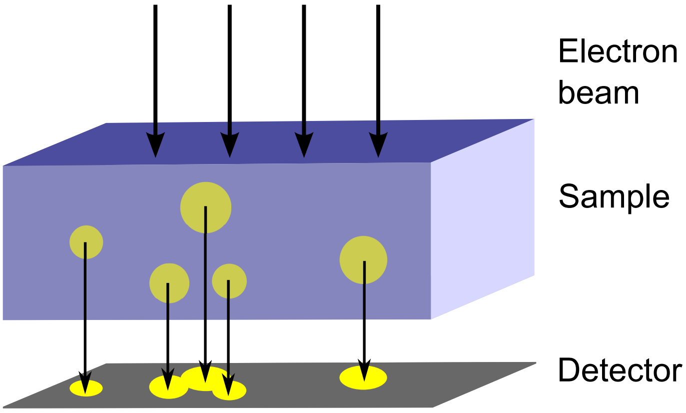

FIG. 2.11: Schematic explanation of a TEM image: The image is a projection of the sample along the measurement axis. Thus, particles that are in the same lateral position, but at different heights of the sample, appear to be joined.

2.3.3 Transmission Electron Microscopy (TEM)

A transmission electron microscope is a commonly used devices for the characterization of nanocomposites. It is one of the few instruments that offer an imaging capability with resolution below 0.2 nm, which makes direct images of crystal structure possible. Since the image is generated by electrons passing the sample, the sample has to be very thin. Depending on the materials used, a sample between 10 and 200 nm is already thick enough to absorb all electrons and hence prevent imaging. This poses a problem in sample preparation: Only very thin samples with low metal concentration can be imaged. Also the substrates suitable for this method are limited, usually a copper grid covered with a thin carbon film is used, which interaction with electrons is low evough to allow the required amount to pass it. In the acquired image a projection of the sample along the measurement axis can be seen. In the case of nanocomposite material containing particles, this leads to the problem that particles may overlap in the image, even if they are well separated in the Z-direction in the sample, like it is depicted in figure 2.11.

The general principle is similar to a traditional light microscope, replacing the beam of light with electrons. A beam of electrons is generated and accelerated to energies ranging from 100 keV to 3 MeV. Then, the beam is focused onto the sample using electrostatic lenses. In the sample, the electrons can be scattered, or can excite secondary electrons, X-rays and Auger electrons. After the beam passed through the sample, different detection modes are possible. In the simplest case, the bright-field imaging, the beam is magnified and projected onto a spacial resolving detector. This yields an image of the sample which shows contrast for chemical species. A second possibility is to detect the diffraction pattern instead of the image, which yields information about the crystal structure of the sample. It is also possible to block out the main beam behind the sample by the use of a aperture and only use one of the diffracted beams. This beam is then again magnified and projected onto a detector, which yields the dark field image. Again a direct-space picture of the sample is obtained, but the contrast is now based on the diffraction intensity, which is sensitive to crystallographic structure. [82]

The measurements in this work were done using a FEI Tecnai F 30 G2 high resolution TEM (FEG, 300kV). This microscope can also be used in combination with an EDX detector (Si/Li detector, EDAX System) for chemical analysis (cp. section 2.3.4). All investigations using TEM were done by the group of Prof. Kienle.

2.3.4 Energy Dispersive X-ray Spectroscopy (EDX)

Energy Dispersive X-ray Spectroscopy (EDX) is a method to determine the chemical composition of a sample. It makes use of the characteristic X-rays that are emitted from a sample, because they can be used to identify and quantify the constituents of the sample. In an electron microscope (SEM or TEM) an focused electron beam is directed onto the sample. It was explained in section 2.3.2 this electron beam can undergo a number of interactions with sample. One of these interactions is the ionization of an atom, which happens by removing one of the lower shell electrons. This is a metastable state, and an electron from a higher shell will undergo a transition to this empty state. The free energy from the difference in potential energy of these two states is then emitted as an photon. Because the energy of the emitted photon only depends on the energy levels of the involved atom, it can be used to identify the chemical species. If further the intensity is analyzed, the concentration of each species in the sample can be determined. Since the binding energy of core electrons increases with atomic number Z, a high primary electron energy is needed to excite X-rays for most species. Most elements have at least one X-ray emission line with an energy under 10 keV, and the usual ideal excitation energy is the triple of the ionization energy, therefore usually an electron beam with a maximum energy of 30 keV is employed. If the chemical species of the sample are known, the beam energy is often chosen to fit the triple of the X-ray line that will be investigated. To quantify the concentration, standards for the different species with varying thickness are compared to the unknown sample and from this the sample thickness is calculated.

Because the mean free path of the X-rays in the order of microns is longer than the penetration depth of the primary electron beam, nearly all emitted X-rays escape the sample. The electron beam is scattered and absorbed when passing the sample, so that the emission of X-rays is highly inhomogeneous. Depending on the elements in the sample, the amount of elastically backscattered electrons can vary from none to nearly the full intensity of the primary beam. This poses a problem for composite materials, as the intensity emitted from a produced standard can exhibit huge variation in comparison to a sample in which other elements are influencing the electron beam and by this the X-ray intensity. Another source for measurement errors is the absorption of X-rays in sample itself. If the X-rays emitted from one species have a suitable energy to cause fluorescence in another species of the sample. This effect causes an shift in the X-ray intensity from one species to another and thus distorts the measured composition.

Two different types of detectors can be used to analyze the X-rays, where both use the same working principle: A high bias is set on an doped semiconductor junction and the current is measured over time. When an X-ray hits the detector, it interacts with the sample and excites electrons-hole pairs, giving rise to a current. The current is proportional to the energy of the incoming photon, allowing the detection of photons of all energies simultaneously. To shield the semiconductor from contaminations in most design it is packed into beryllium foil, which is transparent for X-rays over 1 keV energy. This limits the detector to elements with an atomic number $Z \geq 11$ (sodium), as lighter elements only have emission lines with energies less than 1 keV.

2.3.5 X-ray Photoelectron Spectroscopy (XPS)

A common employed technique to determine the chemical structure of a samples surface is X-ray Photoelectron Spectroscopy (XPS). Similar to EDX, it uses the characteristic energy levels of atoms to determine the chemical composition of a sample. However, the order is reversed: X-rays are generated and sent onto the sample. Here, the X-rays are absorbed and can excite electrons that leave the sample and can be analyzed. In a usual lab experiment the X-rays are generated using a vacuum X-ray tube, where electrons are accelerated onto a metal specimen and generate characteristic X-rays. Most commonly used materials for the anode are aluminum with the main emission on the K_α line at 1486.6 eV and magnesium with the K_α line at 1253.6 eV. The X-rays can then be filtered using a monochromator, at the expense of intensity. Alternatively, the X-rays are used without monochromator, which yields a higher X-ray intensity, but limits the energy resolution. Without filtering, the natural line width of the characteristic X-rays in the order of 1 eV is the determining factor for the energy resolution.

When an X-ray hits the sample it can be absorbed and excite electrons. The electrons then travel through the sample, where they can excite other atoms or be scattered. Their kinetic energy is given by the difference between the X-ray energy $h\nu$ and the binding energy of the original state of the electron E_B:

$$E_{kin} = h\nu - \Phi - E_B \, , \tag{2.3.1}$$

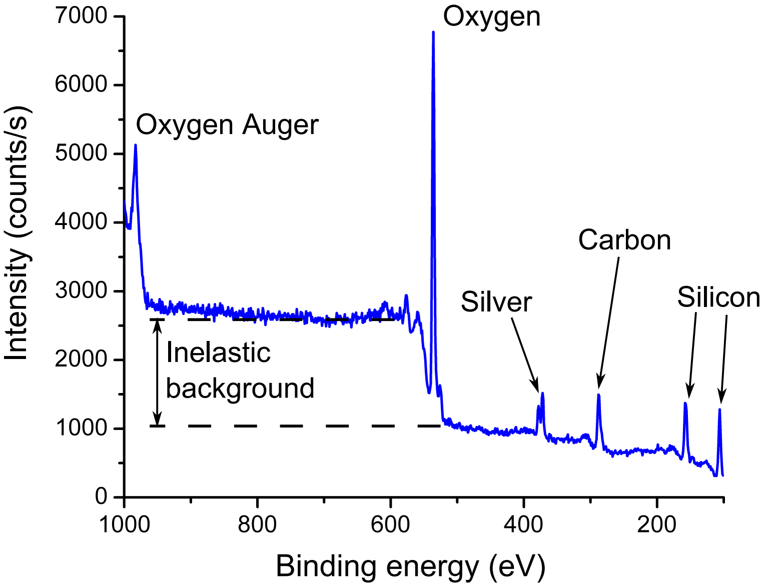

FIG. 2.12: Spectrum of a silver/$SiO_XC_YH_Z$ nanocomposite measured using XPS. The peaks of the constituents are labeled, as well as the inelastic background originating from the main oxygen line.

where Φ is the work function of the sample. An exception to this are Auger electrons (cp. section 2.3.2), as their kinetic energy is determined only by the electronic states of the originating atom and completely independent of the incoming X-ray.

This leads to typical kinetic energies for the electrons in the order of hundreds of eV, in which range they exhibit a short mean free path in the order of nanometers [65]. Therefore, only electrons that originate from a thin layer under the surface escape the sample without scattering and can be analyzed. The electrons that escape the sample are analyzed using a hemispherical electron energy analyzer. A typical spectrum of a thin film sample measured with XPS is shown in figure 2.12.

The binding energy E_B is the number of interest in most cases, accordingly the measured spectrum has to be corrected because of shifts in the energy scale by different work functions and possibly charging of the sample. If the sample is non-conducting it will charge up positively because of ionization from the incoming X-rays. This causes an electric field in between sample and analyzer that attracts electrons and lowers their kinetic energy, and therefore seemingly increases the binding energy of the respective material. Since this effect is constant for all energies, it can be corrected by comparing the binding energies with known values and subtracting the difference from the whole spectrum.

Two other effects cause artifacts in the measured spectrum: When no monochromation is used in the X-ray source, secondary weaker radiation lines are also present and irradiate the sample. They cause satellite peaks, that originate from the same binding energies as the main peaks, but are shifted by the difference in photon energy and have a much lower intensity. In most cases they can be easily identified and ignored, but in some cases they coincide with other possible main peaks and give rise to inaccurate determination of concentration, or even erroneous element identification. Secondly, electrons that undergo inelastic scattering may still escape the sample and reach the analyzer. Depending on their interaction in the sample they lose energy, for example due to plasmon excitation, and give rise to a broad background starting at each main peak and reaching to lower kinetic energies, that is to higher binding energies.

Once the peaks are identified, the composition of the sample can be calculated by integrating the area of each peak and dividing it by the corresponding sensitivity coefficients for this species and transition from literature. The peak positions and sensitivity coefficients used for analysis in this work were taken from the Handbook of X-ray Photoelectron Spectroscopy [47].

A specialty of XPS is the high energy resolution that opens the possibility not only to identifying atomic species, but also identifying their chemical binding states to some extend. Depending on the chemical surrounding of an atom and the type of its binding to the surrounding atoms, the electron binding energy can shift up to 5 eV from their value in the pure material. Through this, it is possible in most cases to differentiate between pure elements and their oxides, for example.

The system used for analysis in this work was an Omicron FullLab, employing an aluminum anode without monochromator for X-ray generation.

2.3.6 UV-Vis Spectroscopy

UV-Vis Spectroscopy can be used to determine the optical properties in the range from UV-light to near infrared of a sample. A beam of light is generated and is then alternating split into two paths by a chopper. One path is used as an intensity reference, while the second one is used to illuminate the sample. Afterwards, both beams are led onto a detector and their intensity is measured. The measured difference in intensity is used to determine transmittance and reflectivity of the sample, depending of the used geometry. If the transmittance and reflectivity are known, the absorbance can be calculated.

After the reduction by reflectivity, the process in the sample can be described using the Beer-Lambert law:

$$T(\lambda) = \frac{I}{I_0} = e^{-\alpha(\lambda) l}\,, \tag{2.3.2}$$

where $T(\lambda)$ is the transmittance, l is the thickness of the sample, $\alpha(\lambda)$ is the wavelength dependent absorption coefficient, and I_0 and I are the intensities of the beam before and after passing the sample. However, because the absorbance is defined as

$$A(\lambda) = -\ln T(\lambda) = -\ln \frac{I}{I_0}, \tag{2.3.3}$$

care must be taken when comparing absorbance and transmittance, since one is an logarithmic quantity while the other is not.

In this work, the spectrometer was used in transmission geometry and the absorbance was calculated neglecting reflectivity. For every measurement, a reference scan was taken from an empty substrate (glass or quartz) and subtracted from the samples spectrum. This also includes reflectivity, so that only the change in reflectivity between the pure substrate and the coated substrate is neglected. The main focus for measurements during this work was put on the optical properties of silver nanoclusters (see section 2.1.3). Only the position, size, and shape of the plasmon absorption peak of these nanoclusters was of interest, and under these circumstances the neglection of change in reflectivity is justified.

A Lambda 900 spectrometer from PERKIN ELMER was used for all investigations in this works. To cover the whole range from UV-light to near infrared it use two light sources: A deuterium lamp for UV-wavelengths and an halogen lamp for the optical and infrared part of the spectrum. Also two different system are used for detection: A Photomultiplier in the UV and visible range, and a lead sulfide detector for near infrared. The witching between the detectors takes place at 855 nm and can cause a disturbance in the spectrum. In most cases this region is not of interest for the samples presented in this work, and hence the disturbance can be ignored. If a spectral feature is located at this point, the switching of the detector can be shifted to a different wavelength.

2.4 Analytical techniques: In-situ diagnostics

Monitoring the plasma and the deposition in real time can be used to predict and control the properties of the generated samples. Additionally it plays an important role in understanding the processes that take place in the deposition source and on the substrate. The main methods that were used in this work for in-situ diagnostics will be discussed in this section.

2.4.1 Quartz Crystal Microbalance (QCM/QMB)

A quartz crystal microbalance is a tool for in-situ measuring of the deposition rate of a deposition source. It consists of a quartz plate that is driven to a mechanical vibration and electronics that measure the frequency of this vibration. The frequency depends on the mass and geometry of the quartz plate, and changes when material is deposited onto it, as it will gain mass. If the deposited mass is small in comparison to the mass of the original plate, the change in frequency is proportional to the deposited mass.

Using this principle, the deposition rate can be measured easily with a good time resolution in the order of a hundreds of milliseconds. The density of the deposited material needs to be known to calculate the deposited thickness, because this system only measures the mass of the deposited material. This leads to a thickness resolution in the order of a monolayer. Other influence on the frequency, that can contribute to errors in the measurement, are the quartz temperature and the elastic properties of the deposited material. Because of the small change in relative frequency the temperature can easily have a bigger influence than the deposited material. For this reason water cooling is employed to keep the temperature of the quartz plate as constant as possible. The assumed linear change in frequency with deposited material only holds true, if the vibrational properties of the material are known and do not change with the deposited thickness. In other cases, careful calibration is needed to get reliable results. [51]

The nanocluster thin films that are deposited on the quartz for investigation of the cluster deposition rate have quite complicated evolution of their mechanical properties. For this reason the exact calibration is an arduous task. This was avoided by frequent exchange of the active quartz plates, in order to always fulfill the assumption, that the deposited mass is small compared to the quartz mass. With this method reliable relative measurements of the deposition rates can be conducted. For exact absolute values ex-situ analysis, such as profilometry or EDX, is the best choice anyway. A STM-100/MF thickness and rate monitor in combination with a OSC-100A oscillator from Syron Instruments was employed in this work.

2.4.2 Mass Spectrometry (MS)

For the investigation of the different processes in the gas phase during deposition, it is important to have information about the different chemical species and their concentration that are involved. To obtain this, mass spectrometry can be used. It offers an easy and direct measurement of the concentration of the different atoms and molecules in the gas phase. A second application of mass spectrometry is the real-time characterization of the produced nanoclusters, which can be done using the same measurement principle, but at different parameters.

The most common principle of operation is a mass spectrometer of the quadrupole type. It consists of 3 main parts: First the incoming atoms and molecules have to be ionized, this can be achieved by a hot cathode or plasma discharge, for example. In the second step the atoms and molecules are filtered by mass. For this 4 metal rods in a square geometry are used. An RF voltage is applied between each two rods that are next to each other, while two rods opposed to each other are always at the same potential. Additionally a DC voltage is superimposed on the RF voltage. The ions which will enter the quadrupole at one side and travel along the rods will now be forced into oscillating trajectory. Depending on the frequency of the voltage modulation, only ions with a specific mass will be on a stable trajectory and reach the end of the quadrupole, all other will escape to the sides. In the last step, the ions that passed the quadrupole have to be detected and counted, which can be done using an channeltron or Faraday cup.

In this work two different devices were used. For plasma and deposition monitoring a Balzers QMS/QME 200 quadrupole mass spectrometer with channeltron detector was used, that is able to detect atoms and molecules with masses up to 200 amu. In cooperation with Marina Ganeva from the group of Prof. Rainer Hippler at the University of Greifswald, mass spectrometry was used to investigate the nanoparticle production of the GAS developed in this work. Here, a QMF 200 quadrupole mass spectrometer from Oxford Applied Research was used, with the possibility to detect ions with masses up to 3 million amu.

2.4.3 Optical Emission Spectroscopy (OES)

A non-invasive method to determine the chemical species and their concentration in a plasma is Optical Emission Spectroscopy (OES). Here, the optical emission from excited atoms and molecules in the plasma is detected and analyzed using a spectrometer. Since many species that are of interest in this work including argon, oxygen, helium and silver exhibit light emission in the optical spectrum, OES is a suitable technique to determine their concentration and excitation states.

Atoms and molecules get ionized and excited by radiation and collisions with ions and electrons in the plasma. Then a possible process for relaxation to the ground state is the emission of a photon. Depending on the species and the excited state, the energy of this photon can be in the range from infrared to UV-light. Using an optical feedthrough and a lens system the emitted light is directed into the spectrometer, where it is analyzed using a diffraction grating and a photomultiplier. From the obtained spectrum the species and their excitation state can immediately be found by looking up the measured wavelengths in a database and comparing them with the possible species. Also, the concentration can be determined, assuming the excitation probability for all species is the same, or it is know for all species. Otherwise, it is still possible to determine the relative change in concentration for each species.

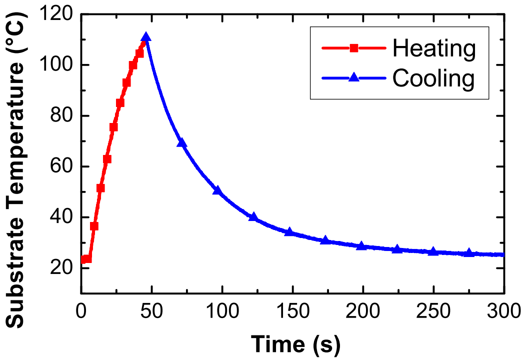

FIG. 2.13: Typical temperature evolution of the test substrate of a calorimetric probe while heating and cooling in a plasma.

In most cases a precise concentration measurement is not possible, but also not required. The main advantages of this method are the high temporal resolution up to 1 ms, the fact that it is non-invasive, and that it only requires a line of sight to the investigated plasma. Additionally, to some extend spacial resolution can achieved using pinholes or lenses, to only analyze the emission from a certain region of the plasma.

A HVR 2000+ spectrometer (OceanOptics) was used for OES measurements in this work. They were carried out in cooperation with Sven Bornholdt from the group of Prof. Holger Kersten from the Institute for Experimental and Applied Physics of the Kiel University.

2.4.4 Calorimetric Probe

A calorimetric probe is an instrument to measure the energy fluxes to and from a test substrate in a plasma. From this data conclusion can be made about the density and respective energy of the species in the plasma. Two principles of operation are commonly used: The active and the passive calorimetric probe. In an active probe the substrate is cooled or heated and the energy flux is determined from the needed power for cooling or heating. In an passive probe, the heating and cooling of the probe is observed and the energy fluxes are determined from the rate of heating and cooling. In this work a passive calorimetric probe was used and the further discussion will thus only include passive probes.

The instrument itself is very simple in design: A metal plate with a diameter of 2 cm and a thickness of 100 µm is used as a test substrate with known thermal capacity and thermal conductivity. It is mounted in a ceramic and contacted on the backside with a thermocouple and a wire. In the plasma, the front of the test substrate will be bombarded with electrons, ions ,and radiation, which leads to heating. During this process, the temperature of the test substrate is measured.By fitting of the heating and cooling curves to theoretical models the contributions of different processes can be distinguished. Additionally a voltage can be applied to the test substrate in order to resolve contributions from particles with different charges. A typical temperature curve of the test substrate is shown in figure 2.13.

Since heating from the equilibrium temperature is required for the analysis, the test substrate must be cooled down before a measurement can be performed. Once a stable temperature, without the influence of the plasma, is reached, the heating can be started. Depending on the investigated system, either the plasma discharge is started, or the discharge was already running and a shutter was brought in between the plasma and the probe is now opened. After a short heating time the discharge is switched off, or the shutter is closed again, and the cooling of the test substrate is observed until it reaches its equilibrium temperature again.

To understand the heating and cooling processes, a theoretical model is applied to the plasma-substrate interaction. The following theory of J. A. Thornton [75] is taken from M. Stahl [70], where the calorimetric probe that was used in this work is described in great detail, his work is also recommended for further study.

The change in enthalpy with time $\dot{H}_S$ can be described by

$$\dot{H}_S = C_S \cdot \frac{dT_S}{dt}\,, \tag{2.4.1}$$

where C_S is the heat capacity of the test substrate and T_S is its temperature. While heating by the plasma, the power P_{in} is acting on the test substrate. Additionally, it is constantly losing energy through the power flux P_{out}. From this we find expressions for the energy balance while heating (h)

$$\dot{H}_{S,h} = C_S \cdot \frac{dT_{S,h}}{dt} = P_{in} - P_{out} \tag{2.4.2}$$

and while cooling (c)

$$\dot{H}_{S,c} = C_S \cdot \frac{dT_{S,c}}{dt} = -P_{out}\,. \tag{2.4.3}$$

If the incoming power P_{in} is constant during heating and the outgoing power P_{out} only depends on the substrate temperature T_S, equation 2.4.2 and 2.4.3 can be substracted:

$$\dot{H}_{S,h} - \dot{H}_{S,c} = P_{in}(T_S)\,, \tag{2.4.4}$$

which is equal to

$$P_{in}(T_S) = C_S \cdot \left[\frac{dT_{S,h}}{dt} - \frac{dT_{S,c}}{dt}\right] = C_S \cdot F[T_S]\,. \tag{2.4.5}$$

where $F[T_S]$ is used as abbreviation for the difference of the derivatives. It has the dimension K/s and should be constant for all temperatures in the ideal case. If C_S is known the power flux P_{in} onto the sample can be calculated from this.

Expanding this, another method can be found that is related to the work of Kersten et al. [36]. Here, the outgoing power P_{out} is described as a function of the substrate temperature T_S. Without an additional incoming power, the test substrate will be at the equilibrium temperature T_{eq}. When the temperature shifts from the equilibrium the outgoing power flux rises, which can be described as

$$Pout(T_S) = a \cdot \Delta T = a \cdot (T_S - T_{eq}\,, \tag{2.4.6}$$

where a is a constant with the dimension W/K. This constant describes the different processes that contribute to the outgoing energy flux, such as heat conductivity, radiation and convection through the gas. For pressure higher than 10 Pa, the cooling by gas has to be taken into account [70]. By substituting equation 2.4.6 in equation 2.4.2 and equation 2.4.3, one gets linear differential equations of the first order describing the heating

$$\dot{H}_{S,h} = C_S \cdot \frac{dT_{S,h}}{dt} = P_{in} - a \cdot (T_S - T_{eq}) \tag{2.4.7}$$

and the cooling

$$\dot{H}_{S,c} = C_S \cdot \frac{dT_{S,c}}{dt} = -a \cdot (T_S - T_{eq})\,. \tag{2.4.8}$$

The solutions for this equations are exponential functions of time, for heating

$$T_{S,h}(t) = \left(\frac{P_{in}}{a} + T_{eq}\right) - T_1 \exp\left(-\frac{a}{C_S} \cdot t\right) \tag{2.4.9}$$

and for cooling

$$T_{S,h}(t) = T_{eq} - T_2 \exp\left(-\frac{a}{C_S} \cdot t\right)\,. \tag{2.4.10}$$

Here, T_1 and T_2 are constants of integration, that can be determined from the starting value and the continuity between heating and cooling. In figure 2.13 it is shown that the measured curves for heating (orange) and cooling (blue) can accurately be fit using exponential curves. The maximum temperature of the substrate T_{max} can be found from the heating function $T_{S,h}(t)$ for $t \to \infty$:

$$T_{max} = \frac{P_{in}}{a} + T_{eq} \tag{2.4.11}$$

Which can easily be solved for the incoming power:

$$P_{in} = a \cdot (T_{max} - T_{eq}) \tag{2.4.12}$$

From this the incoming power can be calculated, as all other quantities are known or can be determined from the exponential fit to the data. Care must be taken if the temperature is far away from the equilibrium temperature, as a linear dependence between the outgoing power and the temperature was assumed in equation 2.4.6.

All measurements during this work were realized with a calorimetric probe from the group of Prof. Holger Kersten from the Institute for Experimental and Applied Physics of the Kiel University. These investigations were done together with Sven Bornholdt, who especially did the calibration of the probe and the analysis of the data.

Chapter 3

Basic Experimental Setup

In the course of this work mainly two systems for nanocluster and nanocomposite deposition were developed and built, the *Open* (Cluster) *Source* and the (Closed) *Cluster Source*[a]. These sources were used to investigate the gas phase cluster aggregation of silver and to subsequently create nanocomposite materials using the silver nanoclusters and a $SiO_XC_YH_Z$ plasma-polymer matrix. Silver was chosen as metallic phase for the nanoclusters because of its high sputtering yield [44], which is needed to create a suitable density of free metal atoms for gas phase cluster growth. Additionally silver is chemically stable and is therefore compatible with the oxygen rich atmosphere which is used for plasma polymerization. The precursor that was used for plasma polymerization, to create the matrix, was HMDSO. It is widely used and well-known, which makes it a good model system for the deposition of nanocomposite materials.

The base for most experiments with these sources was a high vacuum (HV) chamber, shown in figure 3.1. This setup was modified and new components were built in many cases to meet the experimental requirements, especially the newly designed deposition sources were exchanged and repositioned. Figure 3.2 shows the inside of the chamber from the door, in a slightly different configuration than in figure 3.1. Here the DC magnetron for silver sputtering (3) is mounted instead of the Cluster Source. Additionally a sample holder (4) is mounted in the middle of the chamber and a gas ring for helium injection (19) is mounted in front of the magnetron. As most parts were unchanged or reused with only minor modification, this common parts will be described in this chapter first.

The central part of the experimental setup was the vacuum chamber, which was designed in the group by S. Rehders. It was equipped with a two-stage pumping system which consisted of a turbomolecular pump (11) (TMU 261, Pfeiffer Vacuum) and a scroll pump (16) (SH-110, Varian). A butterfly valve

---

[a] Designed in cooperation with S. Rehders

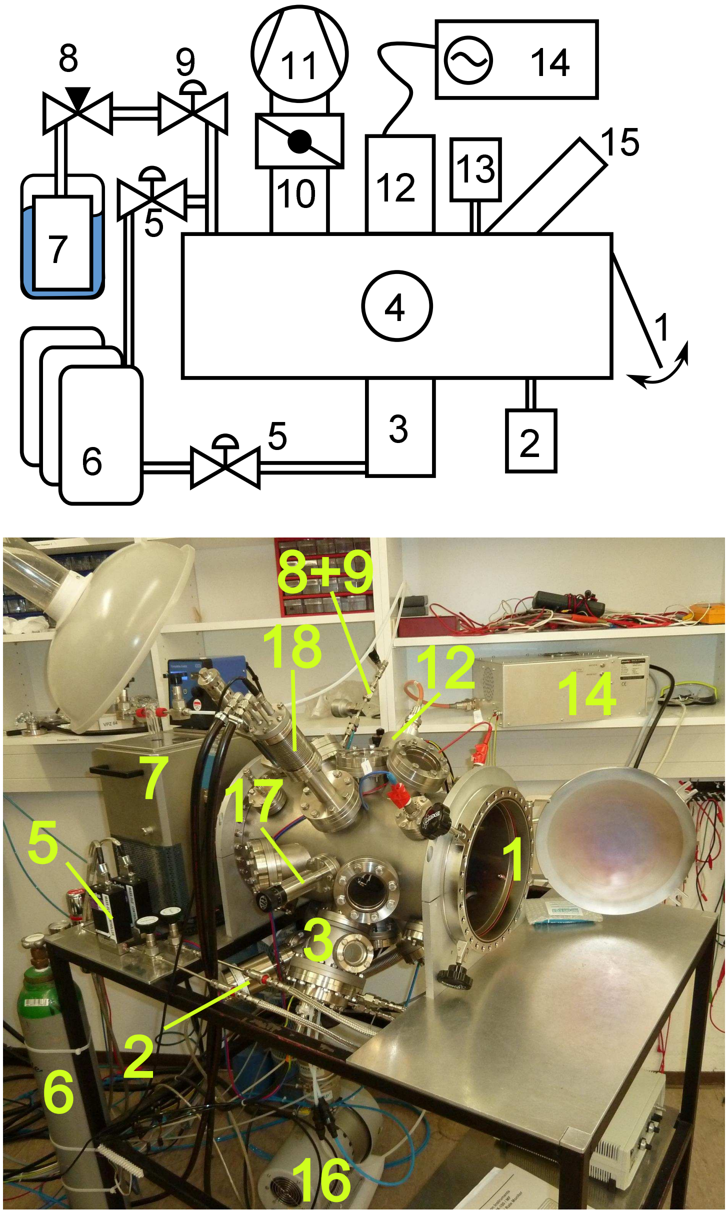

FIG. 3.1: (Top) Schematic and (Bottom) picture of the vacuum chamber used in this work. In this picture the Cluster Source is mounted as deposition source (3).

1	Door	7	HMDSO (temperated)	13	Vacuum gauge
2	Baratron	8	Needle valve	14	RF matching circuit
3	Cluster Source	9	Pulse valve	15	Sample shutter
4	Sample holder	10	Butterfly valve	16	Scroll pump
5	Gas flow controller	11	Turbo pump	17	Source shutter
6	Gas bottles	12	RF-Magnetron	18	QMB

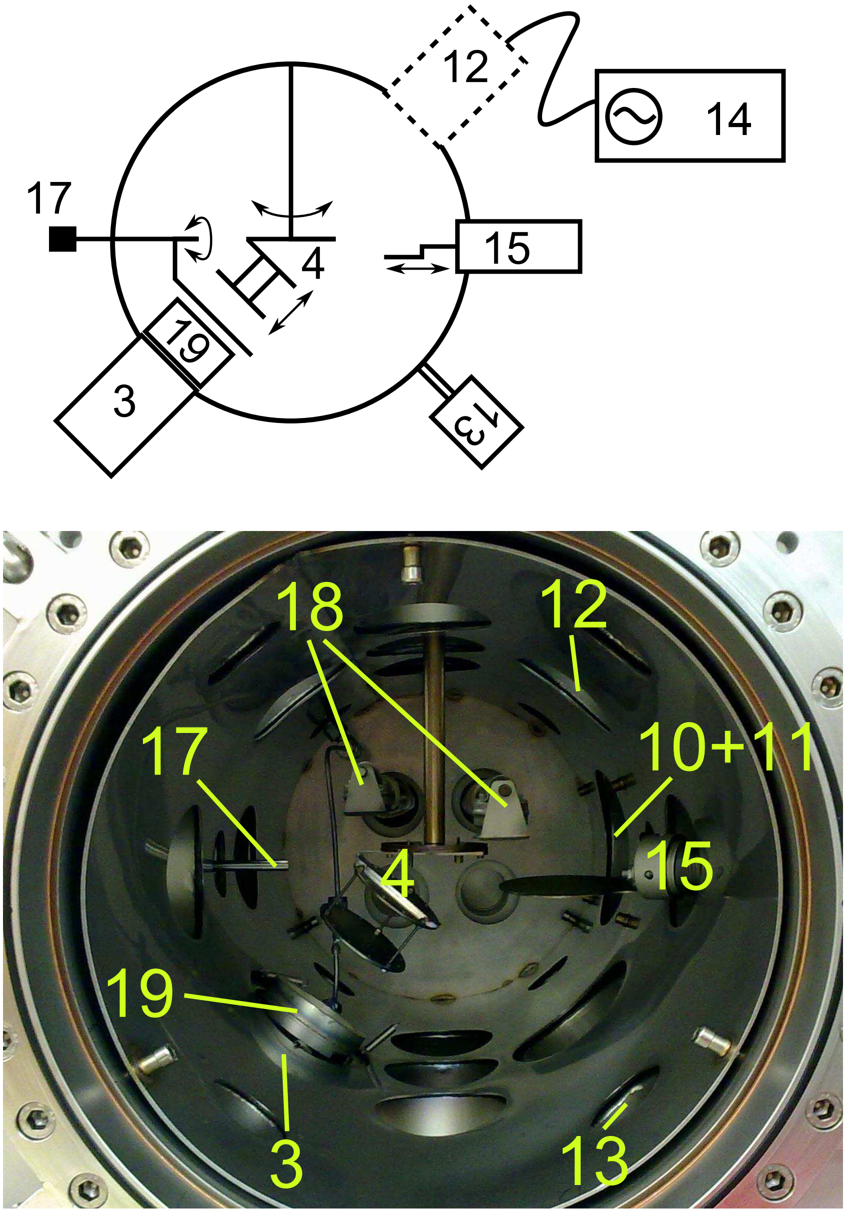

FIG. 3.2: (Top) Schematic and (Bottom) picture of the inside of the vacuum chamber. The dashed magnetron source (12) shows a possible mounting position, that is not occupied in the picture.

1 Door
2 Baratron
3 Magnetron
4 Sample holder
5 Gas flow controller
6 Gas bottles
7 HMDSO (temperated)
8 Needle valve
9 Pulse valve
10 Butterfly valve
11 Turbo pump
12 RF-Magnetron
13 Vacuum gauge
14 RF matching circuit
15 Sample shutter
16 Scroll pump
17 Source shutter
18 QMB
19 Helium injection ring

(10) was installed between the chamber and the pumps to be able to quickly adjust the effective pumping speed. Pressure monitoring was realized by 2 separate systems: A Baratron (2) (MKS, 200 Pa) with a working range from 0.05 to 200 Pa for process control, and a full-range gauge (13) (PKR 251, Pfeiffer Vacuum) with a range from $7 \cdot 10^{-7}$ Pa to atmospheric pressure for pumping and venting. The base pressure of the chamber was $1 \cdot 10^{-5}$ Pa after pumping.

Argon, helium and oxygen gas could be let into the chamber through different lines. Four gas flow controllers (5) (2 to 200 SCCM, MKS) were connected to a controlling unit (Multi Gas Controller 647C, MKS) and were used to control the flow of gas in each line. Two of these lines were connected to the DC magnetron (3), which was used for sputtering metals. Argon was brought into the chamber through the magnetron itself and entered the chamber directly above the target (cp. figure 2.6 in section 2.2.2). On top of the magnetron a gas injection ring (19) was mounted, that could be used for injection of a secondary gas, in this case helium or oxygen. It was connected to the second gas line. This setup of magnetron and gas injection ring was used in both the Open (Cluster) Source and the (Closed) Cluster source. In the former it was mounted directly in the chamber, as can be seen in figure 3.2, while in the latter it was mounted inside a separate chamber, constituting the Cluster Source.

HMDSO, the precursor for plasma polymerization, was kept in liquid form in an evacuated glass bottle in an ethanol bath (7). Using a temperature controller, the bath was held at a temperature between $-30°$ and $10°$ C. Directly at the bottle a stop valve was mounted, that connected the bottle to a pipe that led to the chamber. At the end of the pipe, a needle valve (8) was used to control the flow rate of HMDSO. Next, a electronically controlled pulse valve (9), with a minimal opening time of 20 ms, was used to realize pulsed injection of the HMDSO. In the case of the Open Source, the HMDSO was injected using a second injection ring into the plasma of the DC magnetron. In the Closed Source, however, oxygen and argon from two separate flow controllers were merged with the HMDSO flow behind the pulse valve. This enabled full independent control over the atmosphere for plasma polymerization. The gas mix was subsequently led into the deposition chamber in front of a second magnetron (12), which was of the same type as the DC magnetron. It was powered using an RF generator (CESAR 136, 600 W, Dressler) and a matching circuit (14) (VM 1000 A, 1 kW, Dressler).

Before deposition, the HMDSO was cleaned by cooling to $-30°$ C and pumping with fully opened valves to a pressure of $1 \cdot 10^{-2}$ Pa. For deposition the temperature was increased to $10°$ C, to generated sufficient HMDSO vapor pressure in the bottle. After the deposition, the bath was cooled to $-30°$ C again, in order to minimize the loss of HMDS while storage.

Substrates were mounted at two different places in the chamber, depending on the type of experiment. One possibility was a rotatable sample holder in the center of the chamber, it was used for experiments with the Open Source and for pure cluster deposition. Alternatively, samples could be mounted on the RF magnetron, in the opposite of the Cluster Source. This position was mainly used for composite deposition, but also for cluster deposition when the center of the chamber was occupied by the quartz micro balance. A number of different sample holders were built to fit the requirements in each step of the work. Additionally a quartz micro balance (QMB) was used for in-situ deposition rate monitoring. It can be seen in figure 3.1, that it was mounted on a z-axis manipulator perpendicular to the deposition beam of the Cluster Source. In this configuration it could be brought into the cluster beam for rate monitoring, and retracted out of the beam to allow cluster deposition on a substrate.

Further modifications to this setup, for example for in-situ diagnostics, and the setup for the Cluster Source will shown in the corresponding chapters.

Chapter 4

Open Deposition System

The development of the *Open Deposition System* was the first part of this work. The system was used to investigate the process of gas phase cluster aggregation, using silver as cluster material. Subsequently, nanocomposites were created by embedding the silver nanoparticles in a $SiO_XC_YH_Z$ plasma-polymer matrix. This system consisted of a magnetron to sputter metallic silver and an injection system, that uses the magnetron plasma for plasma polymerization of HMDSO. The main motivation for development of this system was the desire to use in-situ plasma diagnostic techniques during the cluster formation process, which is not possible in a closed GAS. Additionally, these experiments served as a test for the stability of silver clusters in such a plasma-polymer matrix, and the compatibility of these processes and materials in a shared vacuum environment. Of course, the shared atmosphere and plasma had some limiting effect on the possible parameters and sample properties, and this was overcome by the second setup, the *Closed Deposition System* (chapter 5).

In the next section, the setup of the Open Source will be shown in detail. After this, different experimental results will be presented, starting with plasma diagnostic that was used with this system. It will be followed by experiments for gas phase cluster aggregation in the Open Source, and the last part will show the deposition of nanocomposite materials.

4.1 The Open Source

The vacuum system described in the previous chapter was used for all experiments with the Open Source. In this case, the sample holder was mounted in the middle of the chamber (cp. figure 3.2 in chapter 3). One of the possible sample holders was rotatable, and the distance between the substrate and the source was variable. This one was used for deposition of pure clusters. For the experiments with nanocomposites, another sample holder with four mountings for substrates at fixed distance of 65 mm was used, that allowed

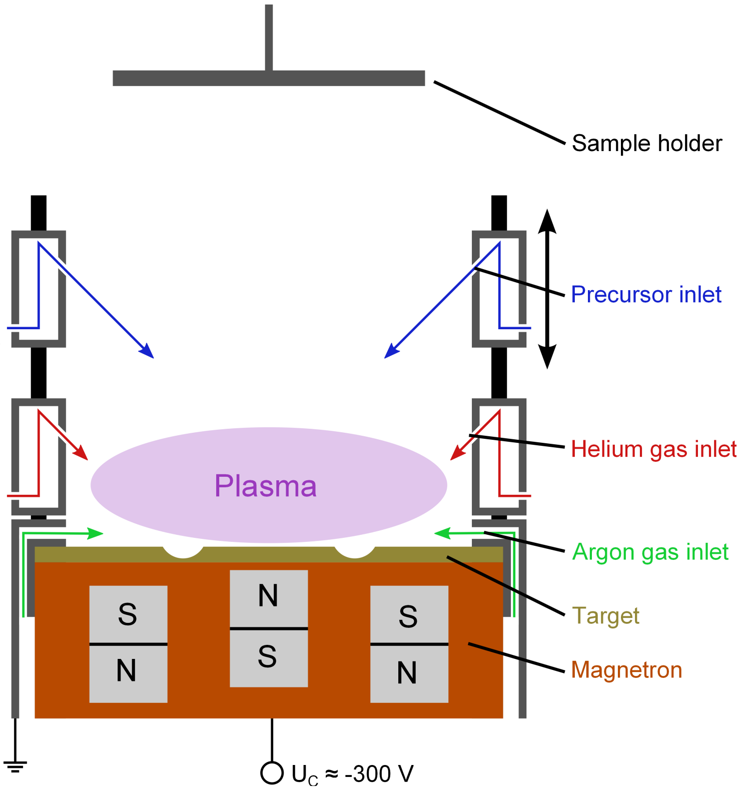

FIG. 4.1: Schematic of the magnetron setup for the Open Source.

the deposition of four samples without evacuating and pumping the chamber for each sample. Additionally, it allowed the deposition of samples using exactly the same deposition parameters, as the discharge and gas flows were running continuously at the whole deposition time.

Figure 4.1 shows a schematic of the Open Source. It consisted of a standard DC magnetron with a silver target, and two concentric rings for gas injection. Argon entered the chamber through the gas channels at the side of the cathode, inside the magnetron. Later, helium was injected into the plasma through the lower ring, at a distance of 11 mm to the target. For experiments with plasma polymerization HMDSO was injected through an additional upper ring, 47 mm above the target. In this setup, the plasma of the magnetron was used for sputtering of silver, as well as plasma polymerization of HMDSO. This simple design came at the price of limited deposition process control. Both, the cluster and the matrix deposition, relied on one plasma discharge, hence, many deposition parameters of these two were bound to each other. One of the dependency was the deposition rate of both constituents, which were both linked to the discharge power. While it was still possible to influence the deposition rate of the matrix by changing the HMDSO partial pressure, there was no other parameter to influence the silver sputtering rate. This especially meant, that it was impossible to deposit pure HMDSO films, since silver sputtering was always part of the plasma process.

Typical conditions for this source were an inert gas pressure of 10 to 300 Pa, using an argon-helium mixture with ratios between 1:3 and 3:1. Usually, a DC power between 3 and 60 W was used on the magnetron. The possible partial pressure of HMDSO for plasma polymerization ranged from 10 to 60 Pa, depending on the inert gas pressure. This parameters were suited to produces nanoclusters in the gas phase. In comparison to the theoretical model, described in section 2.2.4, this source lacked a defined aggregation region that promotes laminar gas flow. Hence, it follows that no aperture was used and therefore it was expected that gas phase cluster coagulation was less likely in this source.

The influence of the pulse valve on the partial pressure could be neglected, however, the pulsing was critical to keep the target from being coated with insulating polymer, resulting in problems similar to reactive sputtering. The ideal setting to avoid target coating was found to be a injection frequency of 5 Hz with an opening time of 20 ms, respectively 10 % duty cycle. The following sections will show the diagnostic techniques that were used to find this parameters.

4.2 Plasma Diagnostic

Calorimetric probe measurements and optical emission spectroscopy (OES) have been used to investigate the cluster-gas interaction during the cluster formation in the Open Source. This experiments were done in cooperation with Sven Bornholdt from the group of Prof. Kersten in the Institute for Experimental and Applied Physics of the Kiel University.

The experimental setup was slightly modified for this investigations: For calorimetric probe measurements the sample holder was taken out, and the probe was mounted on the flange opposite to the source on a rod. In this setup, the distance between source and calorimetric probe could be changed by retracting and extending the rod. All connections to the probe ran through the rod and were shielded against radiation and ions. The test substrate in the probe had a dimension of 0.5 by 10 mm and was made from brass. On its backside, it was connected to a thermocouple for temperature measurement and a copper wire to apply a bias voltage. It was surrounded by a housing made from Marcor® ceramic, to prevent heat loss to the surrounding by radiation or convection. For measuring, it was placed at a distance of about 65 mm to the target, at the same position were typical samples are deposited.

For OES, a similar setup was used: Again the sample holder had to be removed and an optical feedthrough was mounted opposite to the source. The optical feedthrough allowed limited tilting to change the investigated area. A rod was mounted on the vacuum side of the feedthrough to limit the observed area to a small angle, and at the same time reduce deposition on the feedthrough. In this geometry, the measurement was done from a top view on the target and different areas of the target could be analyzed. A optical fiber was connected to the feedthrough and transmited the signal to the grating spectrometer. A HVR 2000+ spectrometer (OceanOptics) was used for this investigation. It had a spectral resolution of about 1 nm and offered time resolved measurements with detection times down to 1 ms.

4.2.1 Cluster Growth

Several experiments with calorimetric probes and OES were conducted to gain insight into the process of cluster growth and the energy distribution of the involved species. These experiments and results were published by Bornholdt et al. [iv], parts of this section are excerpts from this work. The first measurements with a calorimetric probe without a bias voltage showed only a extremely small energy influx, in the order of the minimum detection capability. In a traditional, low pressure, magnetron discharge a substantial influx is expected through high energy ions, sputtered atoms and also heat of condensation as a film grows on the test substrate. In contrast to this, the cluster growth process in the Open Source prevented these three effects. Because of the high pressure and their low mean free path, only very few sputtered atoms and ions could reach the probe with high energy, because they underwent several collisions with the thermalized neutral inert gas. At the same time, most of the atoms were bound in clusters already, and in this process their heat of condensation has already been dissipated.

To be able to detect the ions that leave the magnetron plasma, a negative bias voltage was applied to the probe. As ions that leave the plasma were now accelerated to the probe, first the total number of collected ions rose and secondly also the kinetic energy of the collected ions increased [42]. Similarly, a positive bias voltage was used to get information about the electron density in the chamber.

Figure 4.2a shows the energy influx in dependence of the total chamber pressure at a constant DC power of 50 W and an argon-to-helium ratio of 1:1. It can be seen that with rising pressure the energy influx is decreasing. This can be understood with the same explanation as for the non-biased case before, when the pressure rises, collisions become more probable and thus the number of ions and electrons that escape the plasma decreases. The comparison between the positively and negatively biased case shows that the energy influx is more than one order of magnitude higher for a positively biased probe.

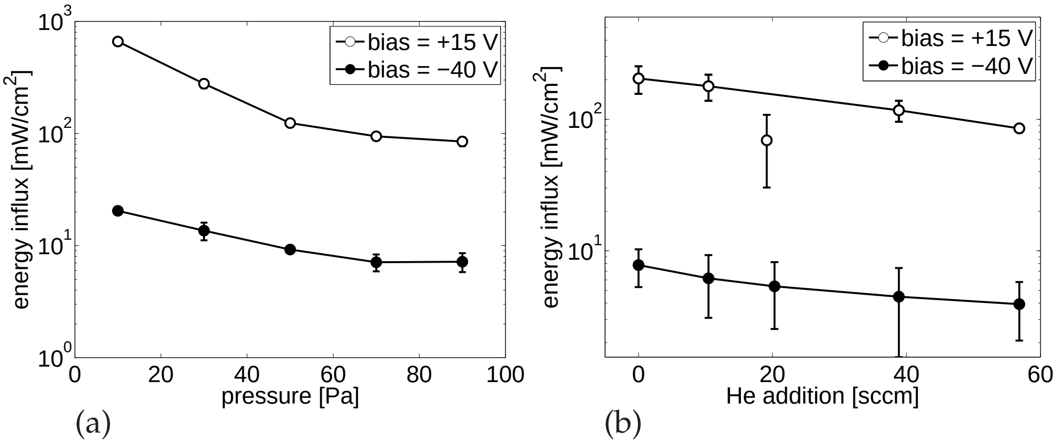

(a) (b)

FIG. 4.2: Energy influx in dependence of (a) the total pressure, with an argon-helium flow ratio of 1:1, and (b) the helium flux, at an argon flow of 54 sccm, and an argon partial pressure of 10 Pa, both at a power of 50 W. From Bornholdt et al. [iv]

This means, that the influence from electrons and negatively charged ions is much greater than the one from positively charged ions.

In the next experiment, the dependence of the energy influx on the amount of helium in the discharge was investigated. The results are shown in figure 4.2b, where the gas flow of helium was varied at a constant argon flow of 54 sccm and a constant power of 50 W. Because of its low mass and high mean free path, helium exhibits a high effective thermal conductivity. For this reason, it is a very effective agent for the dissipation of energy from sputtered atoms [78]. This can also be seen in the graph, since the energy influx is decreasing with increasing helium flow rate.

The influence of helium addition on the sputtered silver can also be seen in figure 4.3. Here, the intensity of emission lines from argon, helium, and silver are shown with different helium-argon mixtures, ranging from pure argon to pure helium. The intensity of the emission of argon decreases, like it would be expected with an increasing amount of helium, the exception being the line at 811 nm. The intensity of this line rises with increasing amount of helium until a mixture with 70 % helium, after this it drops down as the others. This behavior can be explained through an additional excitation of argon that is induced by helium, that does not have a high probability in a pure argon plasma. However, if the amount of argon decreases too much, the number of possible atoms to be excited drops and with this also the total intensity. In conctrast, the intensity of helium naturally increases with a higher amount of helium. The various lines of silver show different dependencies. While some lines a show strictly monotonic increase, others are nearly unaffected or show non-monotonic behavior. It can be concluded that helium interacts with the silver transfering

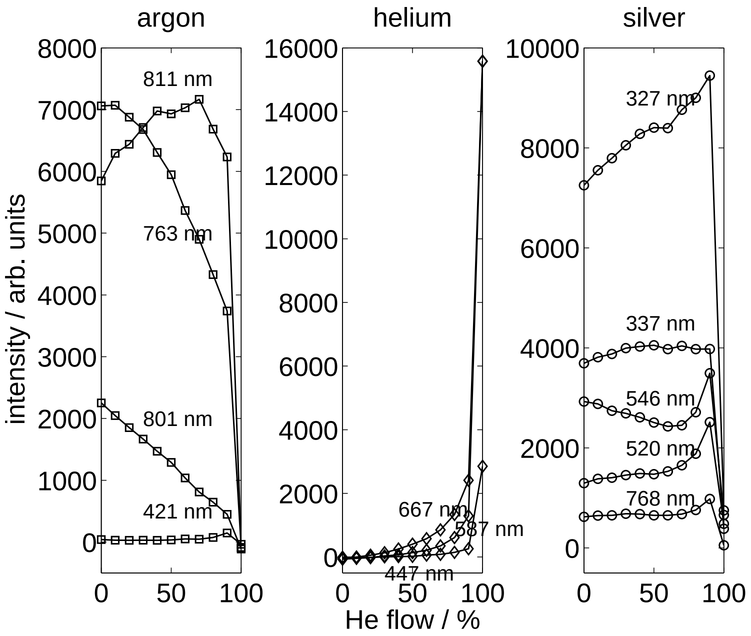

FIG. 4.3: Intensity of emitted optical lines of argon, helium, and silver in dependence of the helium-argon flow-ratio from 0 % helium and 100 % argon to 100 % helium and 0 % argon, at a power of 30 W, and constant pressure of 54 Pa. The assignment of the spectral lines was done using the NIST database [37]. From Bornholdt et al. [iv].

energy between excited states, enabling new routes for de-excitation that were unavailable in a pure argon plasma.

These results confirm that the developed Open Source shows the characteristics of a GAS and can be used as a model system for gas phase cluster aggregation.

4.2.2 OES: Polymer Precursor Injection Optimization

In order to deposit nanocomposite samples, matrix deposition had to be added to the process. This was done by injecting the precursor HMDSO into the magnetron plasma, which led to a simultaneous deposition of silver cluster and the plasma-polymer matrix. As the plasma polymerization was happening in the DC magnetron plasma, a big part of the polymer was deposited on the target. This insulating layer posed a problem, because it could charge up in the plasma and disrupt the sputtering process. A working point had to be found, where the sputtering rate is high enough to prevent a growth of the polymer in the race track and enable continuous deposition.

Time-resolved OES was used to find the optimal pulsing parameters for the injection of the precursor. The DC plasma was running and after some time

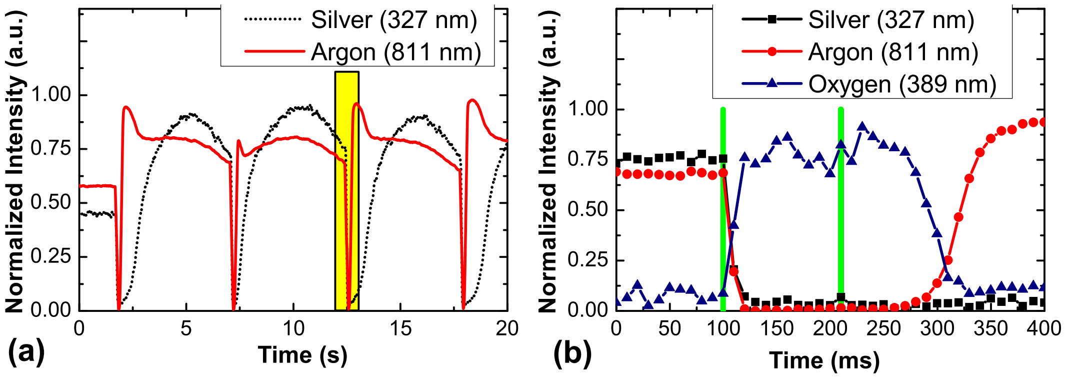

FIG. 4.4: Intensity of emitted optical lines of argon, silver, and oxygen over time. A discharge on a DC magnetron with a silver target using argon is running continuously, while HMDSO is injected every 5.5 s with an valve-open time of 110 ms. (a) Shows an overview over some periods of injection, (b) shows the zoomed-in timeframe that is marked in the overview. The vertical lines mark the beginning and end of the HMDSO injection. The assignment of the spectral lines was done using the NIST database [37].

the HMDSO injection was started with a low repetition rate of one injection every 5.5 s, in order to observe the reaction of the plasma. Figure 4.4 shows the time-evolution of the intensity of optical emission lines from argon, silver and oxygen for this experiment. In this case, oxygen was brought into the chamber from HMDSO, which was dissociated in the plasma. For this reason, the oxygen intensity is a good indicator for plasma polymerization activity.

In part (a) of the figure the intensity of argon and silver over the course of four injections is shown. At the start of the measurement both intensities are stable, but after the first injection they drop to zero. The argon emission goes up again shortly after, reaching an even higher intensity than before the injection. The silver line also rises again, but slower and over a longer period of time. The drop can be explained by the sudden addition of HMDSO, which blocks part of the target by polymerization. In part (b) of figure 4.4 a magnification of the time around the injection can be seen, which is marked with a box in part (a). The green vertical lines mark the time of opening and closing of the injection valve. It can be seen that the drop and rise in argon corresponds to the emerging and vanishing of the oxygen signal. This indicates that it is caused by less excitation of argon, when HMDSO dissociation and subsequent oxygen excitation use up the energy available in the plasma. As soon as the polymerization reaction is finished and the oxygen is bound or pumped, the argon intensity immediately rises again. The fact that the intensity rises to a higher value than before the injection might be caused by argon excitation from recombination reactions of the HMDSO fragments that were not polymerized. Also, the intensity for silver recovers after the injection, however, only much slower, because polymer on the target has to be eroded until silver sputtering starts again.

It can be seen that the intensity of oxygen stays at a high level for about 100 ms after the valve was closed. From separate experiments it is know that the valve can undergo a full open-close cycle in about 20 ms. Accordingly it can be concluded, that the plasma polymerization process still runs for a short time after the precursor injection already stopped, which is a similar behavior as the known effect of plasma polymerization reactions with a pulsed power supply [69]. It is intended to have a continuous deposition process, thats why the frequency should be in the order of 5 to 10 Hz. Since it was found that in our setup the partial pressure of HMDSO is independent of the valve-open time and can be controlled only with the needle valve, a very short opening time of 20 ms is chosen for the valve.

Using this parameters of 5 Hz pulsing frequency and 20 ms opening time, which corresponds to a duty cycle of 10 %, additional long time experiments were conducted to find the range of possible HMDSO partial pressures. While the OES analysis focused on the continuity of the plasma-polymerisation, the partial pressure has to be selected with also the silver target in mind. It should be small enough to never cover the entire target but always leave the race track uncoated to allow continous sputtering. In section 4.4 nanocomposite deposition will be shown, as well as an investigation of different HMDSO partial pressures.

4.3 Silver Nanoclusters

The Open Source was used to study gas phase cluster aggregation in a more simpler design than a typical closed GAS. The usual parameters for cluster production in the Open source were similar to the ones used in comparable closed GAS systems: A pressure of 10 to 300 Pa, using a argon-helium mixture, and a power of 10 to 50 W. For this experiments the Open Source was used in the setup shown in figure 4.1. A sample holder was mounted in the middle of the chamber, which was shown in figure 3.2. On this holder the substrate was mounted parallel to the target at a distance of 7.2 cm. All TEM measurements that are presented in the this part were conducted by Venkata S. K. Chakravadhanula from the group of Prof. Kienle.

The main difference in design of the Open Source in comparison with a closed GAS is the fact that the Open Source lacks an orifice and the conical end piece of the aggregation chamber. This leads to some peculiarities of the deposited clusters. A direct effect from the source geometry is the distribution of the deposition. In a closed design the clusters form a focused beam after they pass the orifice. However, in the Open Source the clusters travel with the inert gas in a all directions, as the geometry of the source does not guide the

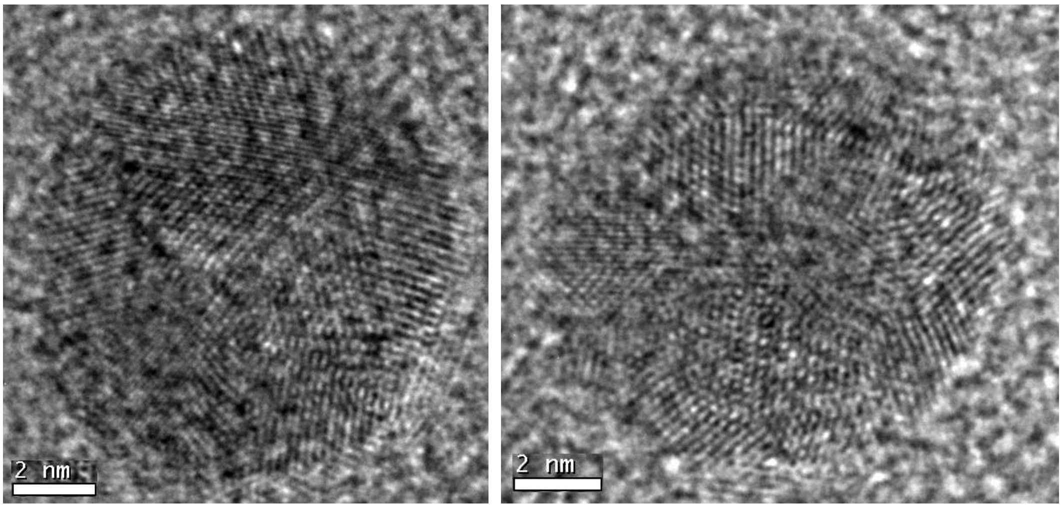

FIG. 4.5: High resolution TEM images of typical nanoclusters deposited with the Open Source, at a pressure of 75 Pa and power of 30 W. Their polycrystalline structure can clearly be seen.

gas stream. This leads to very homogeneous films without the problem of a strong gradient, but at the same time the deposition rate is much smaller, since it is spread over a much larger area.

Figure 4.5 shows two typical clusters that were deposited with the Open Source. It can be seen that the cluster are polycrystalline, which can be explained by the processes during gas phase cluster aggregation. In the first step of cluster growth the cluster seeds only consists of a few ten to hundred atoms. Because of this, the melting point is highly reduced and the particle is in a liquid form. When the cluster growths the melting point rises and at the same time it is cooled by the inert gas. This leads to solidification of the nanoparticle. Since the dimension of the particle is still on the nanoscale, the resulting particle is thought to be monocrystalline. However, in the last step of cluster growth cluster-cluster collisions become more likely and already solid cluster coalescent. In this stage, monocrystallinity cannot be achieved, because the cluster lacks the required thermal energy and time to form a single crystal domain. At a size of about 4 nm diameter, the melting point is already near to the bulk value for silver [87]. This corresponds well to the clusters in this image, where single domains with sizes between 2 and 4 nm can be seen. The overall shape of the cluster also point to this model. The clusters are not perfectly spherical, which can also be explained by insufficient thermal energy and time for diffusion of the atoms in the cluster.

After deposition on the substrate the nanoclusters may diffuse and coalesce. These processes are limited by two factors: First the rate of diffusion and second the average distance between two clusters. For a given material

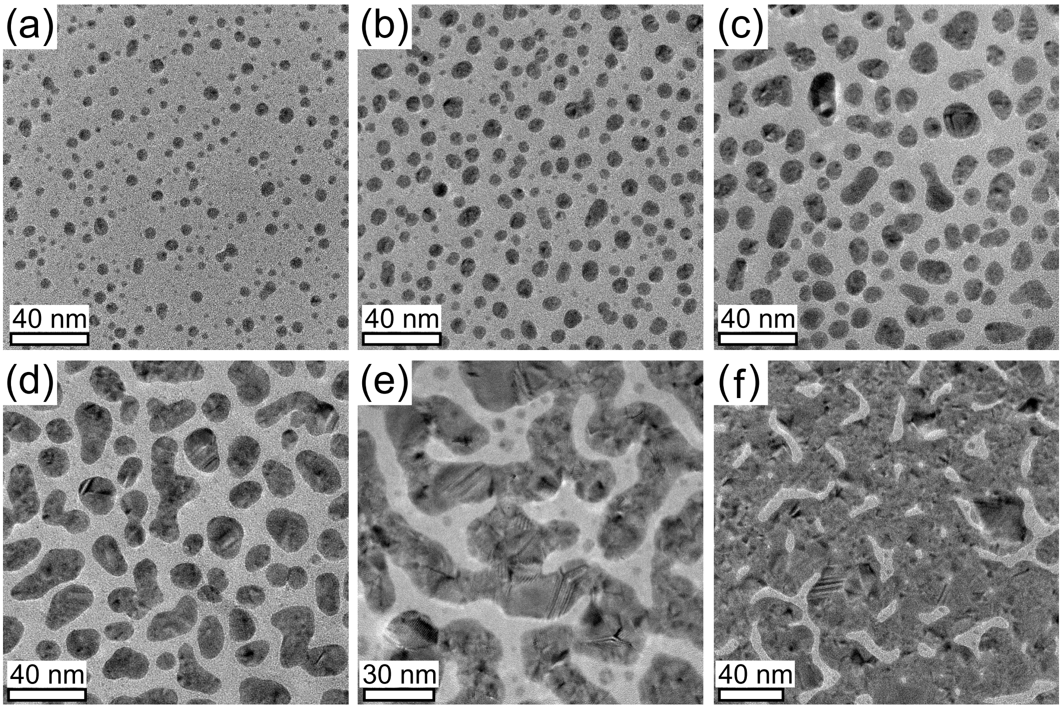

FIG. 4.6: Evolution of surface coalescence of cluster with increasing surface coverage from (a) to (f).

and temperature the rate of diffusion depends primarily on the size of the clusters [53]. Clusters with only 201 atoms already have a diffusion barrier between 0.07 and 0.4 eV [5]. If this is compared to the average thermal energy at room temperature of 0.025 eV, it can be safely concluded that silver clusters of a few nanometers will not diffuse under most conditions. The inter-particle distance is primarily determined by the surface coverage of silver on the substrate, that is the amount of deposited material. With more material, the surface coverage grows and the average inter-particle distances decrease. When the distance decreases, small clusters are able to diffuse to other clusters and merge with them. This process is shown in figure 4.6. In the first frame single, mostly spherical clusters with a broad size distribution, including very small clusters, can be seen. In the following frames the cluster density grows and with it an increasing number of clusters get bigger and non-spherical through coalescence. In the fourth frame, only very few clusters can still be recognized as spherical particles. The fifth frame shows a network of material whose coverage is over the percolation threshold. It constitutes continuous paths through the whole film that connect all points of the layer with each other, allowing for example electrical conductivity. The percolation threshold is especially important for nanocomposite, as many macroscopic properties rapidly

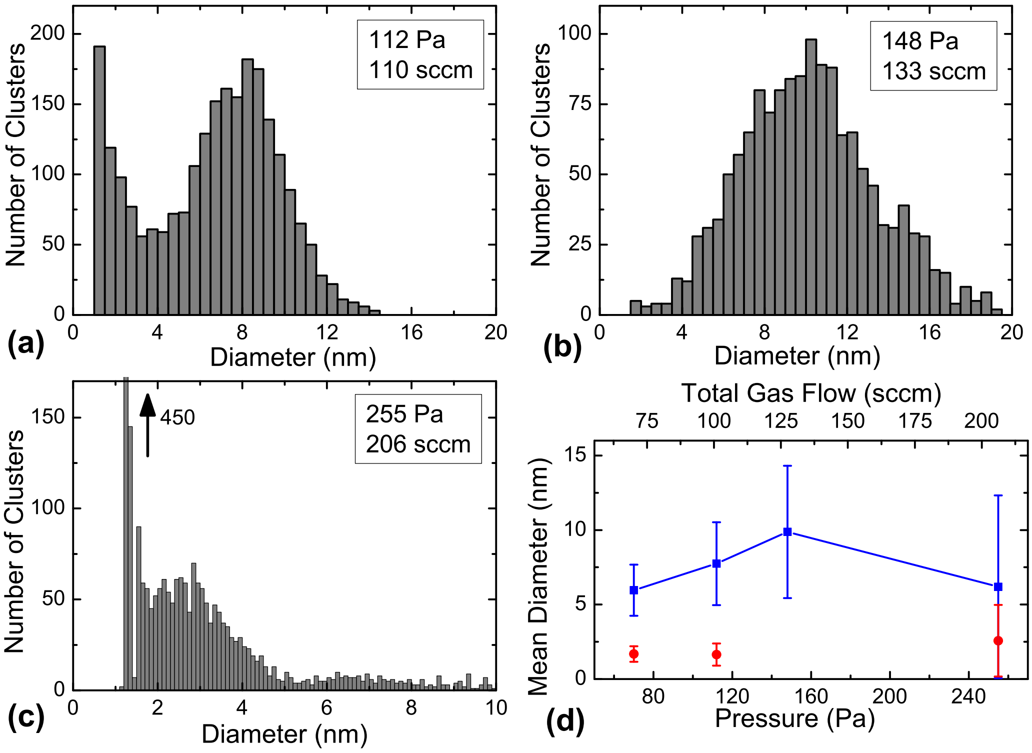

FIG. 4.7: (a) to (c) Comparison of samples with unimodal and bimodal cluster size distributions. (d) Dependence of the cluster size distribution on pressure. The connected points show the maximum of the distribution while the vertical bars show the width of the distribution (FWHM). The single points at smaller diameters show the secondary peaks for bimodal distributions. All samples were deposited with a power of 30 W and a helium-to-argon flow ratio of 1:3.

change at this point [49]. For spherical particles that are homogeneously distributed in a matrix, this critical volume concentration is at 28.5 % [20, 33]. It can be seen in the last frame that if the coverage is increased further after this point, a closed film is formed on the substrate.

Since the aim of this work was the investigation of clusters, the focus was set on the processes that are involved in samples at the stage of the first frame of figure 4.6. One of the differences of clusters deposited with the Open Source in comparison to usual GAS can be found in the size distribution of the clusters. Figure 4.7 shows a comparison of samples with unimodal and bimodal size distributions. These distributions were determined from TEM measurements of samples with low surface coverage. In (a) a bimodal distribution is shown, which is typical for samples deposited with the Open Source. In this case, the sample was deposited at a pressure of 112 Pa, a power of 30 W and a helium-to-argon flow ratio of 1 to 3. Part (b) of the figure shows a distribution of a sample that was deposited with a higher inert gas pressure of 148 Pa, but otherwise unchanged parameters. Here, the distribution broadened and the secondary peak for smaller diameters vanished. For samples with even higher pressures, however, a secondary peak is visible again, as shown in (c). Even a tertiary peak can be found in the shallow background between 5 and 9 nm. Note that in this picture, the scale of the x-axis is altered to a width of 10 nm. In Figure 4.7d the dependence of the mean diameter and distribution width, as full width at half maximum (FWHM), on the inert gas pressure is shown for a constant helium-to-argon flow ratio of 1 to 3 and a constant discharge power of 30 W. The peaks with largest diameter are shown with a connecting line, and the secondary peaks for smaller diameters are shown as single data points.

While the existence of secondary peaks is a unique feature of the Open Source, the non-monotonic behavior of the cluster size is an effect which is also known for closed GAS systems [23]. The maximum in cluster size can be explained by the interaction between several processes: When the inert gas pressure rises, the sputtering rate of metal atoms decreases for pressures beyond ca. 1 Pa [79]. At the same time, the mean free path for metal atoms and clusters decreases, which leads to more efficient cluster seed formation and cluster growth. At even higher pressures this seems to be overpowered by a too short time for growth, as higher gas fluxes move the cluster at a higher speed to the substrate. This is probably also the cause for the variation of the secondary peak. In the case of lower pressures, some smaller clusters or even atoms can reach the substrate without binding to a bigger cluster. If the cluster is much smaller than most other clusters, its thermal velocity is also much higher, because it scales with the square root of the mass. Once the thermal velocity is in the order of the drift velocity of the larger clusters, the integrated interaction probability during the flight time drops significantly. On the substrate the small clusters have again a higher diffusivity than the larger ones, and thus can grow and form the observed secondary peak in the size distribution. In a closed GAS, this is prevented by the conical end, and such small clusters and atoms will either stick to the wall or get caught by bigger clusters when their density rises at this point.

Another difference in behavior can be found in the dependence of the cluster size on the helium gas flux. In common closed GAS designs, a higher helium flow leads to smaller clusters, because it aids the cluster seed formation and thus produces a higher number of smaller clusters [23]. The Open Source, however, shows the opposite effect, as it can be seen in figure 4.8. Here, the size distributions of samples produced in the Open Source, at constant pressure of ca. 70 Pa and a constant power of 30 W, are shown. With a rising helium to argon flow ratio, the mean diameter of clusters decreases, while the width of the distribution remains unchanged. All samples show bimodal distributions, but no significant change in the secondary peak. The reason for this seeming

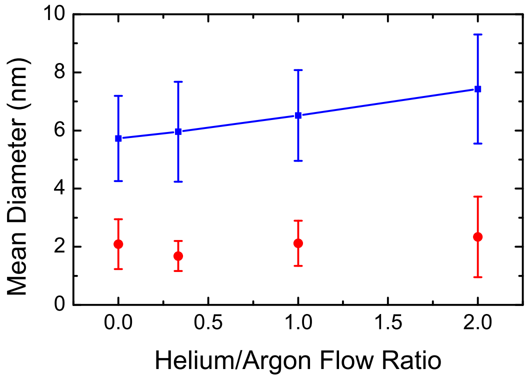

FIG. 4.8: Dependence of the cluster size distribution on the ratio of helium to argon flow rate, at a constant pressure of about 70 Pa. The connected points show the maximum of the distribution while the vertical bars show the width of the distribution (FWHM). The single points at smaller diameters show the secondary peaks for bimodal distributions.

contradiction may lie in the design of the Open Source. Besides the end piece, another major difference to a closed GAS is the missing defined aggregation region. The design of the Open Source allows the gas to escape to the sides into the chamber. This may allow small clusters to leave the inert gas flux more easily, negating the effect of more cluster seeds. When only few cluster seeds are left, the stabilization effect of the helium helps the remaining seeds to grow faster. At the end, some cluster grew very big, while most of the clusters which did not grow fast enough and left the process. This could be the reason for the inverse effect of helium in the Open Source in comparison with closed GAS.

In summary, the Open Source could be used for cluster deposition, while enabling in-situ diagnostics. The effect of smaller cluster that lead to bimodal size distributions, surface diffusion, and cluster growth on the surface is unique for this design. While it poses a problem for single cluster deposition and investigation, it may be used, for example, to support coating of other particles or for filling of cracks.

4.4 Nanocomposites

In the last part of the investigations with the Open Source, plasma polymerization of HMDSO was added to the cluster formation in order to create nanocomposite samples. An important aspect in this investigations were the interactions between sputtering and plasma polymerization, especially on the magnetron target. These experiments were done partly in cooperation with Maike

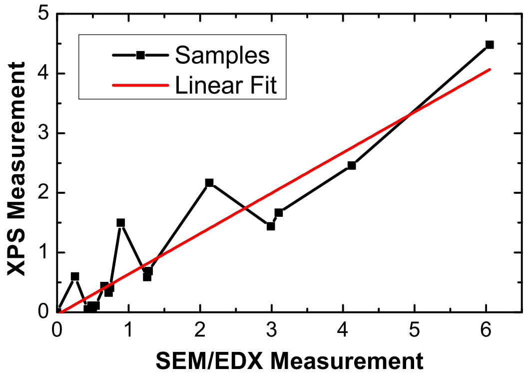

FIG. 4.9: Comparison of the measurement of the atomic ratio of silver to silicon by SEM/EDX and XPS. The fitted line follows the equation $Ag/Si_{XPS} = (-0.04 \pm 0.14) + (0.68 \pm 0.06) \cdot Ag/Si_{EDX}$.

Wegner, and partly by Maike Wegner under my supervision as part of her Bachelor Thesis [81]. Parts of these results were published by Peter et al. [i], excerpts from this publication are used in the following.

The characterization of the nanocomposites was mainly done by profilometry, to determine the thickness, and XPS, to get information about the sample composition. XPS is a surface sensitive technique, therefore its results were compared to SEM/EDX, to estimate the accuracy of these measurements. Several different samples were analyzed using two different SEM devices. First, a Zeiss Ultra plus SEM/EDX at the Fachhochschule Kiel was used by Salah Habouti from the group of Prof. Es-Souni. Second a Philips X L30 was used by Seid Jebril from our group. A comparison of the results from XPS and EDX is shown in figure 4.9. The samples used for this measurements had a thickness of 100 to 200 nm. In this case, EDX is able to measure the whole volume of the sample, because its typical sampling depth is 1 µm. It can be seen in the figure that XPS underestimates the amount of silver in comparison to silicon. This can be explained by the low mean free path of electrons in silver, and the accordingly low sampling depth of XPS. It is typically in the order of nanometers, while a typical silver cluster has a diameter of 2 to 20 nm. For this reason, only electrons from the top part of the cluster can be analyzed by XPS. Since the mean free path of electrons in the polymer is larger than in silver, a larger fraction of the electrons from the polymer reach the analyzer. This leads to an overestimation of the concentration of silicon in comparison to silver [86]. On the other hand, the figure shows that the deviation is linear, so that the data from XPS will give a correct qualitative result and can still be used if no correct total concentration is required. XPS is not the ideal technique for this task, but since it is much faster and more easily available it was used for this investigation.

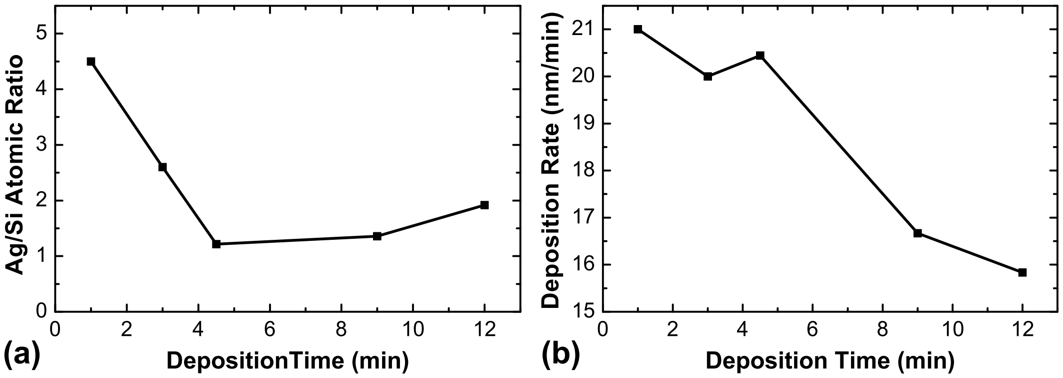

FIG. 4.10: (a) Atomic ratio of silver to silicon and (b) deposition rate for samples with varying deposition times, at a power of 30 W, an inert gas pressure of 10 Pa, and a HMDSO partial pressure of 4 Pa.

Electrons from an area of about 10 mm^2 are analyzed, therefore the XPS measurement is a good average over several billion clusters. The decisive sources for statistical error are the X-ray tube, the analyzer, and its electronics. A variation of about 10 % intensity can be assumed as typical statistical error between two measurements. Sice these always influence the whole measured spectrum, the ratio of two species is mostly uninfluenced by this errors. Instead, small differences in angle and position of the sample holder while measurement, and different water and carbon oxide adsortion on the samples while handing in air, are the main factors for errors in this measurement setup.

4.4.1 Deposition Stability

Like it was mentioned in section 4.2.2, polymer deposition on the target limits the possible range of parameters for precursor injection and sputtering. If the injected amount of precursor is too high, it can cover the whole target with a dielectric polymer film and by this suppress the discharge, similar to the effect of target poisoning in reactive sputtering. Using OES, it was found that the optimal parameters for pulsed injection of the precursor are a frequency of 5 Hz with a duty-cycle of 10 %. This settings were used in all following experiments. For deposition of thin film samples, not only the long term stability and equilibrium are important, but also the short term behavior at the beginning of the discharge and the homogeneity of the deposition. In this and most of the following experiments an inert gas pressure of 10 Pa was used, which consists of a 1:1 mixture of helium and argon. The HMDSO flux was controlled using the needle valve to increase the pressure from 10 to 14 Pa, yielding a HMDSO partial pressure of 4 Pa. This method of determining the partial pressure neglects the effect of change in pumping speed due to inter-

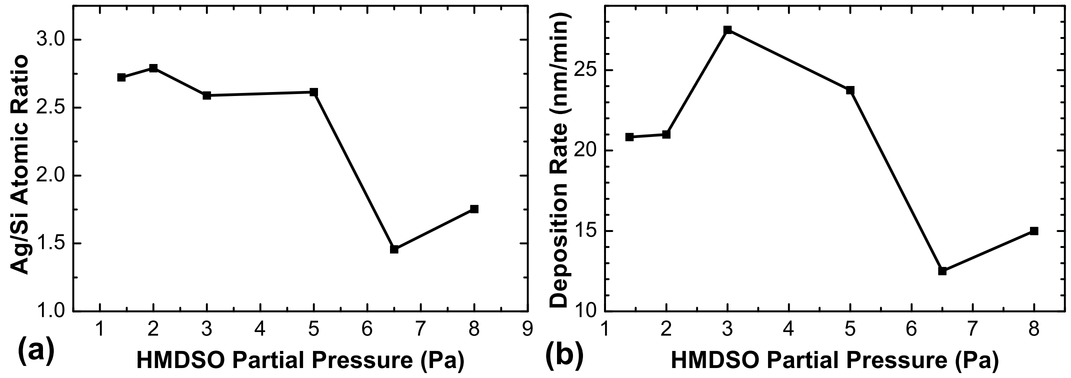

FIG. 4.11: (a) Atomic ratio of silver to silicon and (b) total deposition rate for samples with varying HMDSO partial pressure, at a power of 30 W, and an inert gas pressure of 10 Pa.

actions between the gases. Still it will lead to comparable results, because the pressure was measured in this way in all experiments.

Figure 4.10 shows the evolution of the silver-to-silicon ratio and the deposition rate for samples with deposition times from 1 to 12 minutes. The silver-to-silicon ratio was determined by XPS, so only the topmost layer was analyzed and accordingly the data corresponds to the state of the system at the end of the deposition time. The thickness of the sample, and the rate calculated from this, however correspond to the whole deposition time.

It can be seen, that the silver-to-silicon ratio drops sharply from 4.5 to 1.2 in the first 270 s. This behavior matches the previous results from OES, which showed that the silver target gets coated with polymer and thus less silver is sputtered. Prior to the deposition, the target was cleaned by sputtering in pure inert gas without precursor. Starting with the clean target causes a high amount of silver in the samples of the first few minutes. When the polymer film develops on the target, the amount of silver that is sputtered decreases. At the same time, the polymer film in the sputtering trench is eroded by sputtering and a steady state is reached after about 4 minutes. At this point, also the carbon and oxygen content of the samples remains constant, within the measurement error. However, the measured deposition rate drops further, even after the composition of the samples has reached a constant value. Since deposition rates are not the main interest, this effect is treated by depositing samples with the same deposition time for every investigation. Nevertheless, this uncertainty should be kept in mind when discussing deposition rates of samples created with different parameters.

It was shown before, that the deposition process has a stable state in which polymer growth and erosion on the target are in an equilibrium. The state of the discharge depends on the amount of precursor that is injected into the plasma. Figure 4.11 shows the change in composition and deposition rate for different HMDSO partial pressures at a constant inert gas pressure of 10 Pa. Like it is expected, the silver-to-silicon ratio decreases sharply after a critical amount of precursor is exceeded between 5 and 6 Pa of HMDSO. Prior to this point, the silver content is nearly unchanged. The deposition rate shows an increase for small partial pressures, which can be explained by enhanced growth of polymer without strong negative effects on the sputtering of silver. If the amount of precursor is increased further, the deposition rate drops significantly, because the silver sputtering is now suppressed. This drop is in good agreement with the change in composition at the same HMDSO partial pressure.

As our main goal is a stable discharge, the optimal point for nanocomposite deposition seems to be just below the critical partial pressure. For this reason, a partial pressure of 4 Pa HMDSO was chosen, since this yields reasonable deposition rates. Also at this point, a small variation of the partial pressure will not cause a huge effect on the discharge stability.

4.4.2 Composition

The main parameter that can be used to influence the composition of the nanocomposites is the discharge power. In figure 4.12(a) the change in composition of the samples with varying discharge powers can be seen. For powers under 10 W the silver content rises swiftly from 7 to 29 %, while over 10 W the concentration only rises slowly to 36 % at 60 W. The sputtering rate of silver is approximately proportional to the discharge power. Also the plasma polymerization gets more effective with rising power. It seems that for low powers until 10 W the amount of sputtered silver for cluster aggregation and the direct deposition of atomic silver is not enough to generate a high silver concentration in the sample. Only after a threshold the sputtering gets effective enough to yield a high metal portion in the nanocomposite.

The composition of the matrix also shows a largely different behavior under and above 10 W. While the oxygen and silicon content follow a similar trend in both regions, the amount of carbon drops much faster with rising silver concentration. This is expected from HMDSO, because the only source for oxygen and silicon are the center bridge of the HMDSO molecule. The binding strengths of these center atoms are much greater than the silicon-methyl and the intra-methyl bindings. For this reason, the silicon and oxygen content from the precursor is build into the matrix nearly unchanged [7, 50]. On the other hand, the methyl group is fragmented much more heavily with rising ion energy and current in the plasma. These fragments have a high chance to leave the plasma and stick to walls or be pumped, in contrast to the more heavy and thus slower silicon-oxides. Above 10 W, the composition changes

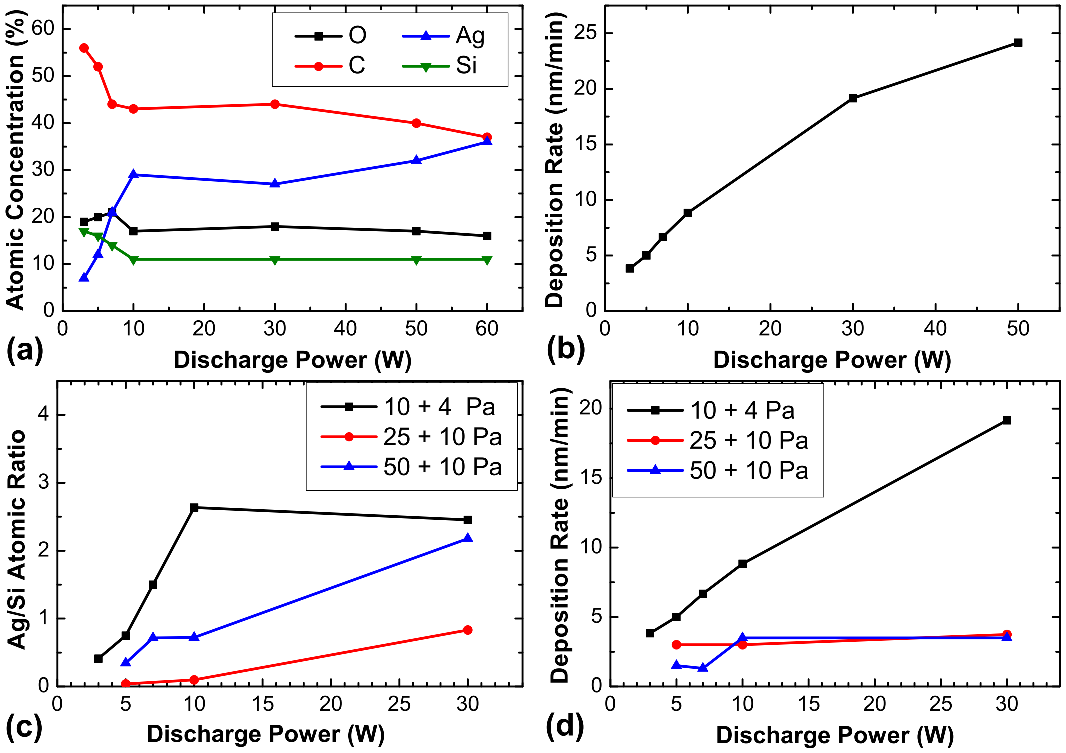

FIG. 4.12: (a) Atomic concentration of silver, silicon, carbon, oxygen and (b) deposition rate for samples with varying discharge power, at an inert gas pressure of 10 Pa and a HMDSO partial pressure of 4 Pa. (c) Atomic ratio of silver to silicon and (d) deposition rate for samples with discharge powers from 3 to 30 W, for total pressures of 14, 35, 60 Pa, which consist of 10, 25, 50 Pa of inert gas and 4, 10, 10 Pa of HMDSO.

much slower with power. Again the change in silicon and oxygen concentration is neglectable, while the carbon content drops even further. As it can be seen in part (b) of figure 4.12, the deposition rate shows a monotone rise over the whole range of discharge power. This means that both processes get more effective with rising discharge power.

Figure 4.12(c) and (d) show the changes in composition and deposition rate with discharge power for 3 different inert gas and HMDSO pressure combinations. The black/square data points are from sample that were deposited with the parameters that were discussed before. In the case of the red/circle line, the inert gas and HMDSO pressure both were increased by a factor of 2.5, and for the blue/triangle line inert gas pressure was doubled again. Both cases with higher pressure lead to a much lower silver content at lower powers. With 50 + 10 Pa the silver content nearly reaches the value of the low pressure samples, but the deposition rate is much lower for all powers. For this pressures, the discharge is in an already damped state, like it is indicated by the

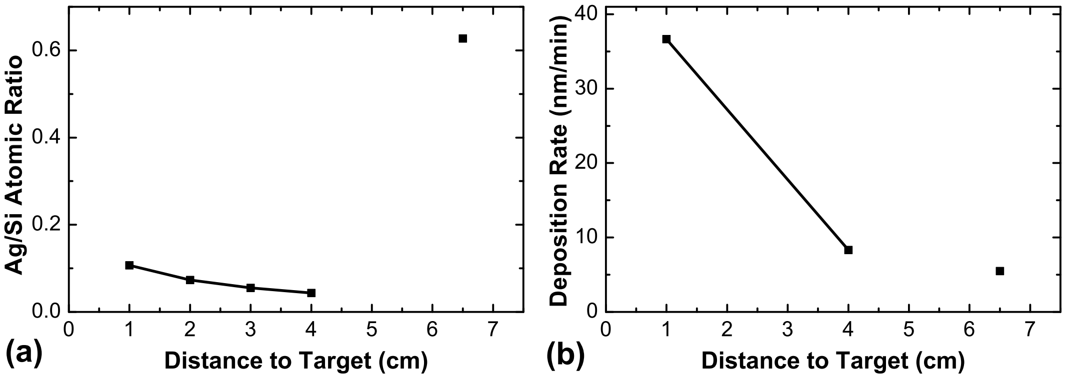

FIG. 4.13: (a) Atomic ratio of silver to silicon and (b) total deposition rate at different position inside the chamber. The samples for distances between 1 and 4 cm from the target were positioned perpendicular to the target, while the sample at 6.5 cm distance is the position on the standard sample holder which is oriented parallel to the target.

low deposition rate and low silver content. It may be possible to find a more stable pressure combination with a lower amount of HMDSO, but this was not pursued in experiments.

Typically, a sample position outside of the active plasma was used. This corresponds to an indirect deposition of plasma polymerization. Figure 4.13 shows the silver-to-silicon ratio and deposition rate for samples at positions closer to the target, inside the plasma, and a corresponding data point from a sample at the standard position. This samples were mounted on the side of the injection rings, perpendicular to the target, while the standard sample holder is parallel to the target. In comparison with the standard sample position at 6.5 cm, the data of the first two samples show a much higher deposition rate of the plasma polymer, yielding a very low silver concentration. For samples at only slightly greater distance the deposition rate drops significantly, because the amount of ionized precursor fragments is much lower outside of the active plasma. Still, the silver concentration is very low, which can be attributed to the tendency of the silver to follow the gas stream away from the target, in the direction to the sample holder. For this reason only a very small portion of the silver clusters stick to substrates at this perpendicular position. Also the deposition of atomic silver on a direct trajectory from the target to these substrates is highly unlikely in such a high pressure atmosphere.

4.4.3 Morphology

Three nanocomposite samples were analyzed using TEM, and the corresponding images can be seen in figure 4.14. Their composition, determined with XPS, is listed in table 4.1. At first glance, the morphology of sample (a) and (b) seem

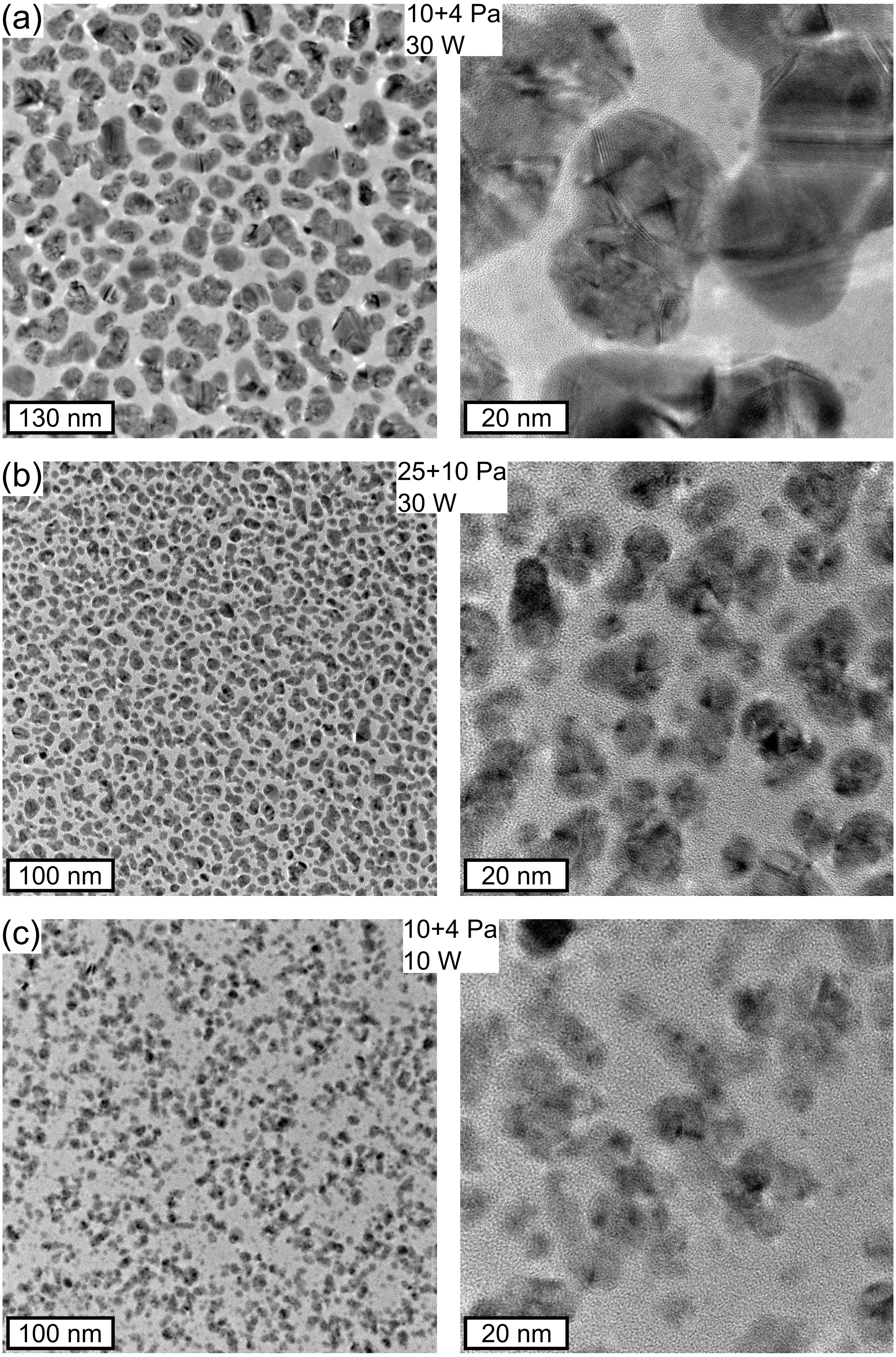

FIG. 4.14: TEM images of 3 samples with varying pressure and discharge power. The right side shows an image with higher magnification of the same sample as shown in the left side.

Sample	Oxygen	Carbon	Silver	Silicon	Ag/Si
(a) 10+4 Pa, 30 W	25 %	46 %	22 %	7.5 %	2.93
(b) 25+10 Pa, 30 W	17 %	45 %	22 %	16 %	1.31
(c) 10+4 Pa, 10 W	19 %	58 %	5.2 %	19 %	0.28

Table 4.1: Composition of the nanocomposite samples shown in figure 4.14.

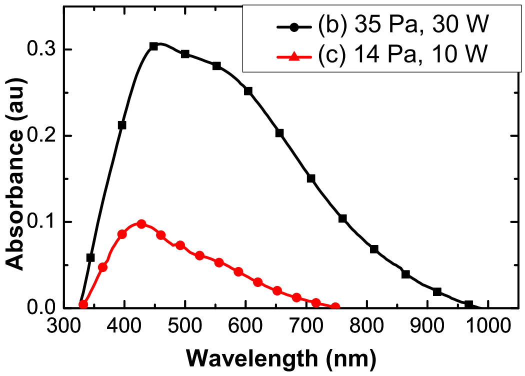

FIG. 4.15: UV-Vis absorption spectra of a sample deposited with (a) 25 Pa of inert gas, 10 Pa of HMDSO, at 30 W power, with a thickness of 25 nm and a sample deposited with (c) 10 Pa of inert gas, 4 Pa of HMDSO, at 10 W power, with a thickness of 35 nm. TEM images of this samples are shown in part (b) and (c) of figure 4.14.

to contradict the earlier results that showed an increase in cluster size with pressure. However, the silver concentration of these samples is quite high and cluster coalescence and growth on the substrate has clearly set in. This way also small cluster, like they can be seen in sample (a) in between the larger ones, will diffuse and agglomerate after deposition. Two reasons for the different growth in this samples can be given here: First at high concentrations smaller cluster are more prone to surface agglomeration, because of their much higher diffusion rate. Second, it was stated before, that the matrix composition is changed and especially the higher silicon content in sample (b) might hinder diffusion and by this further agglomeration.

Sample (c) in the same figure shows a composite with much lower silver concentration, in which the deposited silver clusters are clearly separated. However, this low silver concentration is not expected from the previous results, and was probably caused by an error during deposition. This concentration and morphology would only be expected for even lower powers near 3 W, according to prior measurements.

The difference in morphology of these samples is also visible in the plasmonic resonance in the UV-Vis absorption spectrum, shown in figure 4.15.

While the sample (b), with much bigger and coagulated clusters, shows a very wide absorption, the peak in the spectrum of sample (c) is smaller both in its maximum and width [17]. Simulations by Amendola et al. [3] show that for a sample with perfectly monodisperse and separate cluster only a very sharp single peak is expected as only plasmons of one frequency can be excited, while a broader size distribution allows plasmons with a wider frequency range and thus show a broader absorption. Coagulated nonspherical clusters also allow plasmon excitations with different frequencies depending on the excited axis, giving rise to shoulders and double-peaks in the absorption spectrum, as it can be seen in this case.

From this results we can conclude, that the Open Source is an interesting method to realize and study nanocomposite deposition. The interaction between clusters, inert gas plasma, and plasma polymerization determines most of the behavior of the deposition. This can be used to gain inside into these interactions, because the setup allows easy access with in-situ diagnostic techniques. Also the deposited composite materials can be studied, however most applied research is limited by the restricted control over the matrix. The admixing of an oxygen flow to further change the matrix composition is impossible, because the additional oxidation of the target would aggravate the problems of system stability. The control over the matrix can be improved by separating the cluster growth from the matrix deposition, at the cost of a more complex setup and less possibilities for plasma diagnostics. This approach will be followed using the Closed Cluster Source, which is presented in the next chapter.

Chapter 5

Closed Deposition System

In the second part of this work, the Closed Cluster Source was designed, built, and used for the investigations. The Cluster Source was a self-designed[a] GAS that was used for the investigations of gas phase cluster aggregation of silver. As a next step, these silver nanoclusters were embedded into a plasma-polymer matrix in order to create nanocomposite samples. In the last part of the work, a method for reactive gas phase aggregation of titanium was developed and investigated. In other works of the group also cobalt [22] and aluminum clusters were deposited using this source.

The main advantage of this new setup in comparison to the Open Source was the independent control over the two deposition processes. Since all cluster growth processes happened inside a separate volume, all relevant parameters such as pressure, discharge power, inert gas low rate, and gas composition can be tuned in a bigger operational range. This was especially interesting for composite deposition, because the deposition rates and properties of clusters and matrix could be controlled with less interaction. Additionally, this setup allowed the in-situ analysis of deposition rates using a quartz microbalance (QMB). This design and the investigation of silver nanoclusters and nanocomposites were published by Peter et al. [iii], and excerpts of this publication are used throughout this chapter.

5.1 The Cluster Source

The experimental setup for the Closed Source was based on the vacuum chamber that was used before, and was described in chapter 3. A few changes were made in comparison to the previous setup for the Open Source: The new Cluster Source was mounted instead of the DC magnetron and its gas injection system. An RF magnetron was mounted opposite to the Cluster Source,

---

[a] In cooperation with S. Rehders

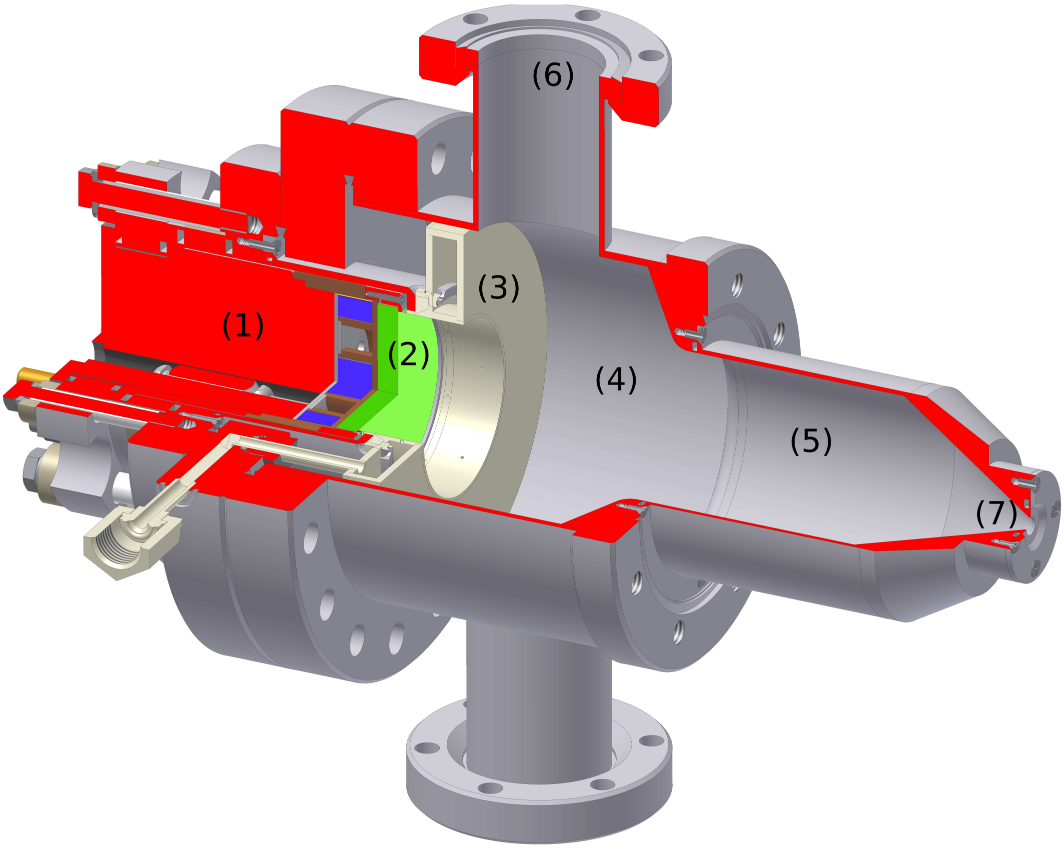

FIG. 5.1: Cross-sectional view of the Cluster Source: (1) Magnetron, (2) target, (3) gas injection ring, (4) central aggregation region, (5) changeable secondary aggregation region ,(6) connection to baratron and by-pass, (7) conical end of aggregation region and orifice. From Peter et al. [iii]

for plasma polymerization. With it a separated gas injection system for argon, oxygen, and HMDSO was mounted as well. The sample holder was dismounted from the center of the chamber, and instead a QMB was mounted on a linear feedthrough, perpendicular to the axis of the Cluster Source. This allowed to move the QMB into and out of the nanocluster beam without breaking vacuum. It could be used to check the deposition rate and its evolution before and in intervals during a deposition of a sample, or do long-time investigations of the Cluster Source. In between the Cluster Source and the QMB a movable shutter is mounted to block the nanocluster deposition if desired. An additional shutter behind the QMB is not necessary, because the cluster beam is blocked completely by the QMB when it is extended.

The most important part of this setup is the Cluster Source itself. It was specifically developed and designed to fit to most aspects of the previously used Open Source. The DC magnetron and the argon-helium injection system in the Cluster Source are identical to the one used in the Open Source. Furthermore, it included the possibility for OES measurements in the closed volume. To achieve flexibility for investigations some parts of it were changeable, namely the elongated aggregation region with the conical end and the orifice that leads to the deposition chamber. This parts could easily be swapped for pieces with other geometries and sizes.

Figure 5.1 shows the design of the Cluster Source. The generation of metal vapor was realized using a 2 inch planar magnetron (1) with a 6 mm thick target (2). Argon was injected through the magnetron directly above the target. An additional gas could be injected using a ring (3), which is placed next to the magnetron. Helium and oxygen were injected through this ring in this work. Cluster aggregation and coalescence happened during the transport through the aggregation chamber, which consisted of two parts. The central part of the chamber (4) had a diameter of 104 mm and a length of 85 mm, measured from the target till the end of this part. In this part, there were two possible connections for extra mounts (6). Usually on one of these side flanges a window for process monitoring and optical spectroscopy (OES) was mounted. The other side flanges was connected to a three-way cross, which leaded to a baratron for pressure control of the Cluster Source, and a valve. This valve was connected to a by-pass to the main chamber and could be opened for faster pumping of the Cluster Source. While deposition this valve was closed, forcing the gas stream and the metal clusters in the second part of the aggregation region (5). This second part was mounted onto the Cluster Source and could easily be replaced, changing its diameter, length, and the general geometry. The commonly used part in this work is shown in the figure, and had an aggregation length of 98 mm with a diameter of 60 mm. At the end of the aggregation region, an orifice (7) constituted the exit to the main chamber. This orifice was also interchangeable with other pieces of different diameter. For this work, a diameter of 3 mm was used in most cases, because this offers the highest deposition rates. This allows the broadest parameters for composite deposition, as the rate of cluster deposition has to compete with the high deposition rate of the polymer matrix. In contrast to most other GAS designs, the Cluster Source did not use liquid nitrogen or water cooling of the aggregation region walls. Typical operational parameters were powers from 10 to 80 W, but also powers up to 200 W are possible. The gas flow rates ranged from 5 to 150 SCCM, yielding an aggregation pressure of 10 to 200 Pa.

The setup that was used for plasma polymerization is depicted in figure 5.2. A magnetron of the same type as the one used in the Cluster Source was used for the secondary plasma discharge. It was operated using RF power, which is less susceptible for problems arising from coating with the dielectric polymer. A mock target made from stainless steel was used to minimize sputtering, as this was not intended for this source. Since mostly a low power between 2 and 10 W was used, the sputter rate was low enough to not interfere with

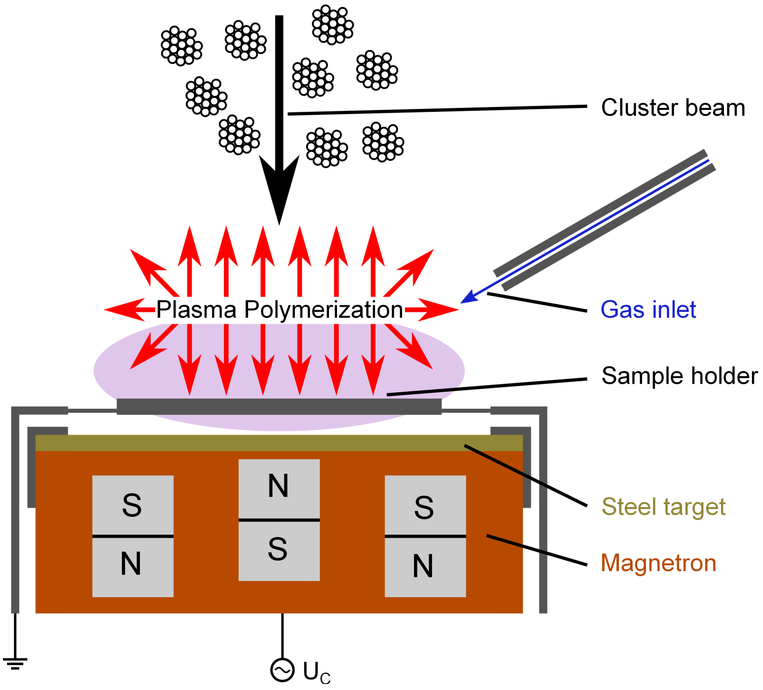

FIG. 5.2: Schematic of the setup for plasma polymerization. An arbitrary mixture of argon, oxygen, and HMDSO can be injected through the gas inlet into the plasma.

the operation. Any material that was sputtered, hit the backside of the sample holder and thus did not interfere with the experiments. The sample holder was mounted in front of the target in a distance of about 10 mm. It was grounded by its connection to the outer hull of the magnetron. An mixture of argon, oxygen, and HMDSO was injected through an inlet at the side of the sample holder. The three gas fluxes could be controlled independently by separated gas flow controllers. This injection led to plasma polymerization of HMDSO, and by this to polymer coating of all surfaces near the plasma. Of course, this included the samples on the sample holder, where the polymer coating was intended. But also the sampler holder itself and parts of the magnetron were coated and had to be cleaned after some time. The cluster beam from the Cluster Source reached the magnetron from the opposite of the chamber perpendicular in the middle of the sample holder. For this source usually argon flow rates between 10 and 80 SCCM, with oxygen flow rates up to 20 SCCM were used. The total gas pressure was typically between 1.5 and 2 Pa, with an HMDSO partial pressure from 0.01 to 0.075 Pa.

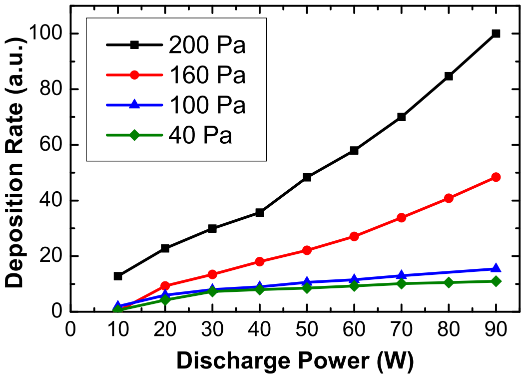

FIG. 5.3: Deposition rate of the Cluster Source measured by QMB for different pressures and discharge powers. In all cases, pure argon was used as inert gas.

5.2 Silver Nanoclusters

The Cluster Source produced an intense, focused beam of nanoparticles, that was directed into the main deposition chamber. Here, the clusters could either be deposited onto a substrate, or they could be analyzed using the QMB. In this and the following sections, the investigation of this Cluster Source using silver will be presented. At first, the general properties of the cluster beam and the deposited film is discussed, and in the second part the properties and possibilities for nanoclusters are shown. A Zeiss Ultra plus SEM device at the Fachhochschule Kiel was used by Salah Habouti, from the group of Prof. Es-Souni, for the presented measurement in this section.

The main parameters that influence the cluster beam are the discharge power, that is used for sputtering, and the inert gas pressure in the source. In an exact view, the effects of inert gas flow rate and pressure should be separated. They are, however, tied to each other by the size of the orifice, and changing the orifice might also change other characteristics of the gas flow and the resulting cluster beam. For this reason, only the inert gas pressure with an orifice size of 3 mm diameter is discussed in the following.

The QMB was used to investigate the deposition rate of the Cluster Source. Figure 5.3 shows the dependence of the deposition rate on the discharge power for different gas aggregation pressures. It should be noted, that the QMB only measures the change in mass and does not distinguish between size of clusters or the type of film they form. Like it is expected the deposition rate rises with increasing power for all pressures. For lower pressure the detected deposition rates decreases, which is mostly an effect from the change in the cluster beam focus. The cluster beam is broader when a lower pressure in the Cluster Source is used. Because the sputtering rate does not significantly change with pressure, the amount of free metal for cluster formation is approximately con-

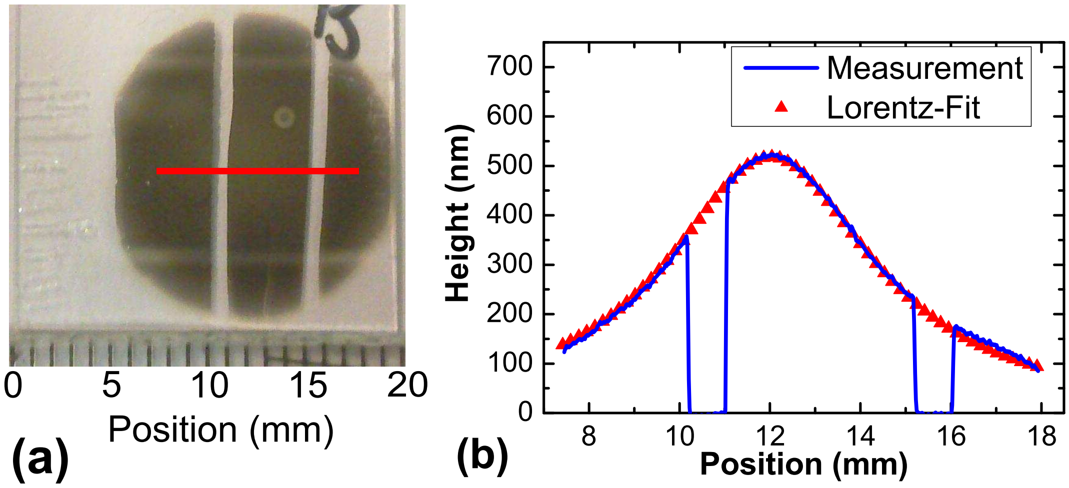

FIG. 5.4: (a) Photograph of a typical nanocluster sample deposited at 30 W power and 200 Pa pressure for 300 s at a distance of 8 cm to the Cluster Source. (b) Contact profilometer measurement at the red line shown in (a).

stant. Changes in the cluster formation process will mostly influence the size distribution of cluster, but not the total mass of the produced clusters. Thus, the same amount of material is spread over a larger area, leading to a lower deposition rate that is measured on the area of the QMB.

5.2.1 Nanocluster Thin Films

Samples that were created by depositing the cluster beam over a time of several minutes have the form a gray to black circular spot. The height profile of this deposition spot naturally corresponds to the profile of the cluster beam and can be approximated using a Lorentz profile. A photograph and height profile of such a sample is shown in figure 5.4. It can be seen, that even at a low power of 30 W a deposition rate of 100 nm/min is achieved. Using a still moderate power of 80 W rates up to 300 nm/min were possible at the distance of 8 cm. Because of the beam nature of the deposition, all rates have to be compared keeping distance and pressure in mind. A variation of these parameters can cause a change in maximum height by broadening or narrowing of the deposition spot.

On the microscopic level, these dark deposition spots are made up of a porous network of metallic silver nanoparticles. An SEM image of this structure can be seen in figure 5.5. It can be seen, that the film consists of agglomerates with sizes up to 50 nm. The typical size of nanoclusters that were formed inside the Cluster Source was 5 to 15 nm, indicating that these structures were

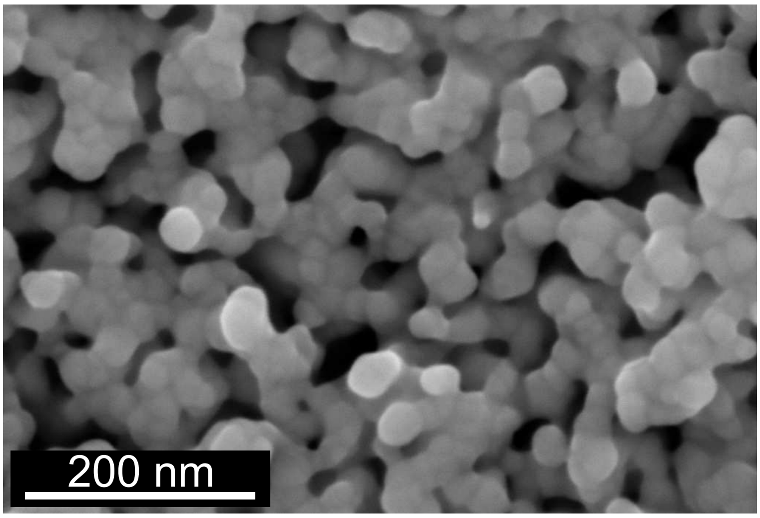

FIG. 5.5: SEM image of a porous cluster film with a deposition time of 120 s at 30 W power and 160 Pa aggregation pressure of argon.

formed by coalescences of the nanoclusters. Such films show good electrical conductivity, like it would be expected from metallic bound silver.

At the same time, the films showed a very low mechanical stability, which posed a problem for handling, because even a slight touch would remove the film. It was observed, that very thin films until about ≈ 20 nm thickness were even destroyed when using a contact profilometer with a force of 0.5 mg. Thicker films, starting at ≈ 100 nm, were more stable and could easily be measured using a contact profilometer, but they were still susceptible to touching. If the film was deposited at a very small distance of only 1 cm for a longer time, extremely thick samples up to few millimeters could be deposited. These samples showed much higher mechanical stability, and could only be destroyed by hand with some effort.

Theoretical works report, that the porosity of such a system can reach values up to 85 % [77] for a system of hard spheres. EDX was used to determine the porousity of the silver nanocluster samples deposited with the Cluster Source. The amount of material bound in a dense and a porous film with a height of 100 nm each was compared, yielding a porosity of about 50 %. This is in good agreement with the fact that the silver cluster coalesce and agglomerate, yielding a denser film with a lower porousity than in the case of hard spheres.

The dark color of the films is caused by their porosity. Figure 5.6 shows the UV-Vis absorption spectra and photographs of two such films with different thickness. For a very thin film, the color is still determined by the plasmon resonance of the constituting silver cluster. While a thicker film shows high

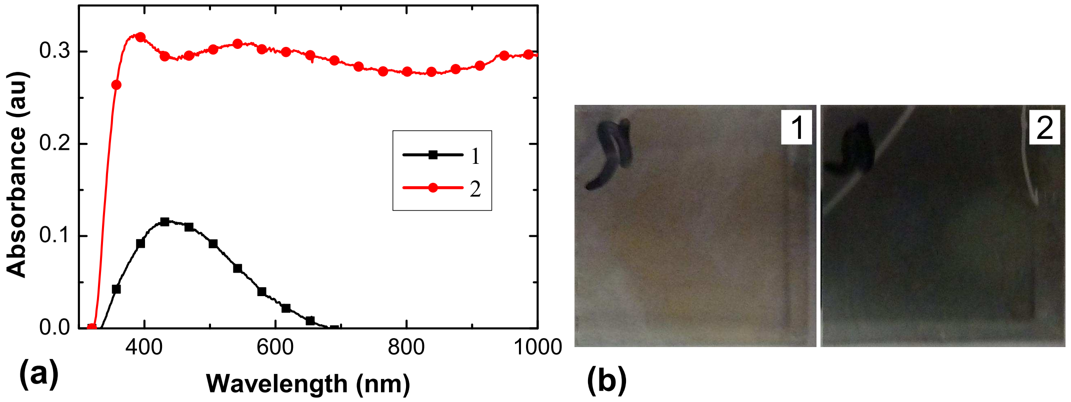

FIG. 5.6: (a) UV-Vis absorption spectra and (b) photographs of 2 porous nanocluster film samples with varying thickness. Sample 1: < 20 nm, Sample 2: 35 nm

absorbance over the whole measured spectrum. This is an indicator, that the color is caused by multiple scattering of light in the porous structure, leading to broad absorption with very little reflection and transmission.

These highly porous films have some potential applications for cases where a high surface area is desired, such as catalysis. Also the moderately weak bounding may be interesting for other materials, as it may help to suppress unwanted volume properties. Still, the low mechanical strength will pose a challenge for most applications of these films.

5.2.2 Nanoclusters

One of the main goals was the deposition of nanocomposites using the Cluster Source, because of this the study of the nanocluster properties was an important prerequisite. For this purpose, some key aspects of the nanoclusters that are produced in the Cluster Source will be discussed in the following. Figure 5.7 shows a TEM image and the size distribution of a typical nanocluster sample with short deposition time of about 1 s. Here, separated spherical clusters with a mean diameter of 13 nm and quite narrow width of ≈ 3 nm (FWHM) can be seen. A more detailed analysis of the cluster size distribution was done using a mass spectrometer and will be presented in the next section.

To determine the charge of the clusters, a special setup using electrostatic deflection was used. This setup is shown in figure 5.8b. Behind the orifice of the Cluster Source, the beam was directed through a pinhole to cut away the outer parts of the beam. Subsequently, the clusters were directed in between two plates with opposite bias voltages, up to ± 70 V. At a small distance behind the plates, the QMB was mounted. It could be moved in a range of 5 cm,

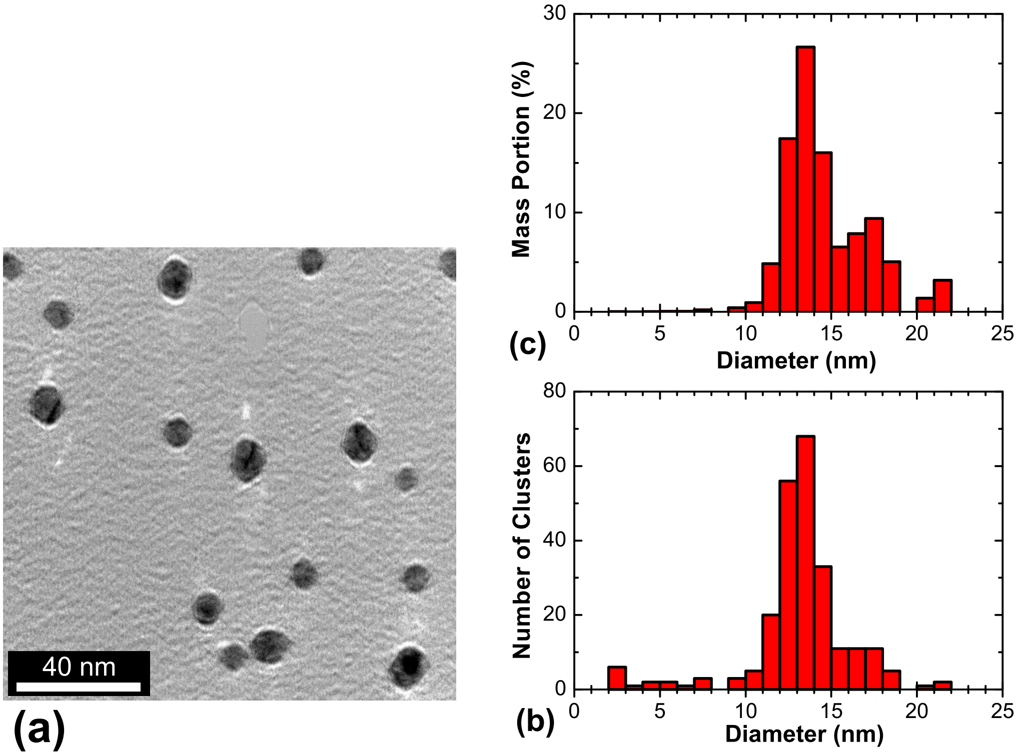

FIG. 5.7: TEM image of single clusters from a very short deposition time (≈ 1 s) at 50 W power and 200 Pa aggregation pressure of argon. (b) Size distribution by numbers of clusters and (c) by mass of the cluster of the same sample.

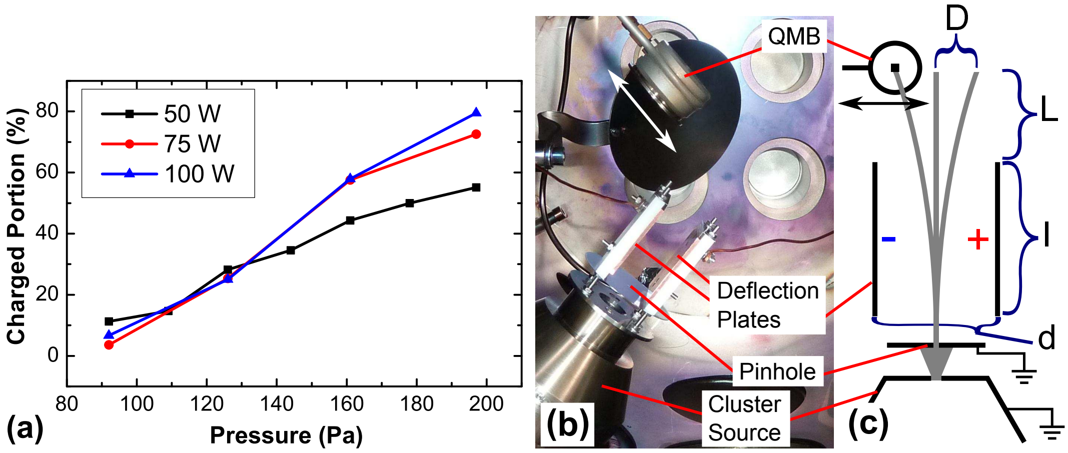

FIG. 5.8: (a) Portion of the cluster that is charged in dependence of power and pressure. (b) Photograph and (c) schematic of the experimental setup for charge separation experiments.

from approximately the lower plate until far above the upper plate. The latter position is the position in which it is shown in the image.

In order to improve the resolution, the measuring area of the QMB was limited to 5x5 mm by a partial cover. Otherwise, the resolution of the setup was mainly defined by the size of the used pinhole. With a large pinhole the deposition spots of clusters with different charge-to-mass ratio overlapped over a wide area, making a distinction impossible. On the over hand, a small pinhole led to low deposition rate on the QMB. Especially with low pressures and powers, the deposition rate was too low to get meaningful signal-to-noise ratios. Also, a small pinhole led to problems with high deposition rates, because the pinhole got covered over time with material. As this causes a decreasing transmission over time, it prevented comparable results for successive measurements. In the case of a power of 30 W, a pressure of 200 Pa, and a pinhole with 0.5 m diameter, the first change in deposition rate due to this effect could be seen after merely 30 s. Another 90 s later, the pinhole was closed completely and no deposition could be measured anymore. For this reason, a pinhole with 1.5 mm diameter was used for the following experiments.

Using electrostatic theory, the total deflection D of a cluster with the mass m and charge q from its path entering the deflection plates at the center with a speed v_0, can be calculated to

$$D = \frac{Uql}{v_0^2 dm}\left(\frac{1}{2}l + L\right) , \tag{5.2.1}$$

where $d = 1.5$ cm is the distance between the two plates, $l = 3$ cm is the length of the plates, U is the voltage between the plates and $L = 1.75$ cm is the distance between the plates and the detector. For clusters of a diameter of 10 nm, a velocity of $v_0 = 100$ m/s [56] and a single elementary charge the total deflection is $D \approx 1.4$ cm at a voltage of $U = 140$ V. So even the heaviest and fastest clusters that were expected would be deflected far away from the detector area, which was only 5x5 mm in size.

Experimental results using this setup are shown in figure 5.8a. In this experiment the deposition rate of the full cluster beam without deflection voltage was compared to the rate with a deflection voltage of ± 70 V. From the ratio of these two rates the percentage of charged clusters could be calculated, assuming identical size distributions for charged and neutral clusters. It can be seen, that the charged portion only varies lightly with the discharge power, which is surprising in comparison with results for other GAS in the literature [56]. The pressure seems to be the main influence on the charged portion for the Cluster Source used in this work. A more detailed measurement for the typical parameters using a power of 50 W and pressure of 200 Pa yielded a positive-to-negative charge ratio of 0.86 for the clusters. From this the total charge distribution could be calculated to 45 % neutral, 25 % positvely and 30 % negatively charged clusters.

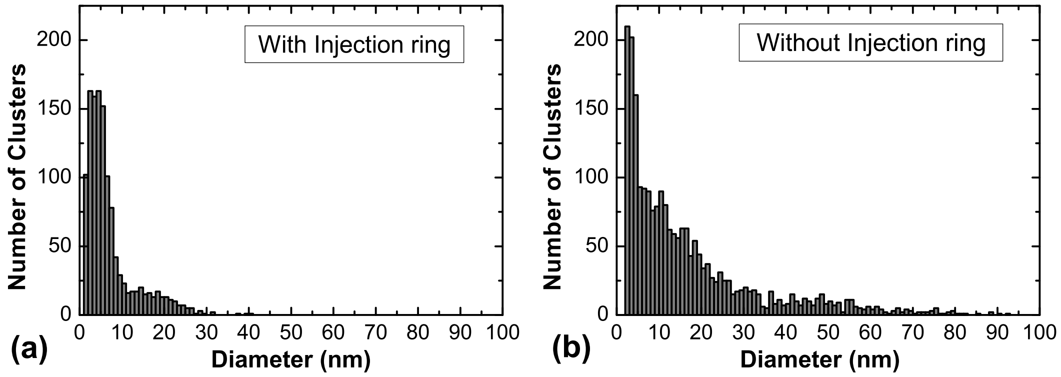

FIG. 5.9: Comparison between the cluster size distribution of two samples deposited with a discharge power of 50 W and an argon aggregation pressure of 40 Pa. One sample (a) was deposited in the normal geometry of the Cluster Source, while for the other (b) the gas injection ring inside the Cluster Source was removed.

The most important part of GAS design is the gas flow, as it determines the aggregation time and cluster acceleration. Of course, by this it influences all parts of the resulting beam and cluster properties. Figure 5.9 shows an example how a small variation in geometry can cause a big change in cluster properties. Two samples were deposited with identical parameters: A power of 50 W, a pressure of 40 Pa using pure argon as inert gas, an aperture of 3 mm diameter, and a deposition time of 180 s. For sample (a) the setup that was shown before was used, while for sample (b) the ring for helium injection was removed. Obviously this leads to a much wider size distribution, that includes clusters with sizes up to 95 nm. A possible explanation for this would be a more turbulent gas flow at an early stage of cluster growth, that leads to longer aggregation times for some clusters, allowing them to become much larger. For the aim of this work, the first case is of course the favorable one, as a narrow size distribution is essential to control the properties of the resulting samples.

5.2.3 Quadrupole Mass Spectrometry

Experiments using TEM measurements, to determine the size distribution of clusters, are suffering from two main disadvantages. First, in our case they are quite time-consuming, because the samples have to be deposited and subsequently measured in cooperation with another group. And second, they are prone to over or under-deposition, where either too much material leads surface aggregation that makes it impossible to determine the size distribution of the gas phase aggregation. Or on the other hand, too little material leads to too few clusters and causes large statistical errors. Yet, it is still an invaluable

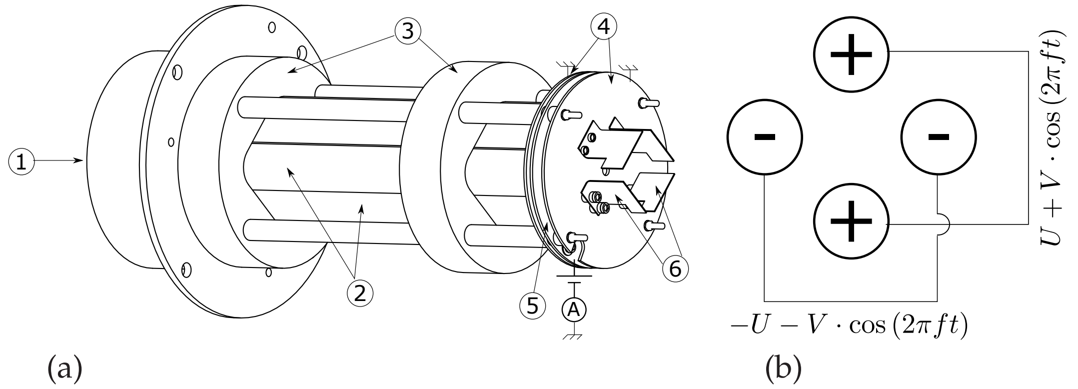

FIG. 5.10: (a) Schematics of the QMF-200, (b) front view of the quadrupole rods and their voltages. From Ganeva et al. [v]

1	Cluster injection	3	Dielectric isolation	5	Ion detector plate
2	Quadrupole rods	4	Grounded plates	6	Deflection plates

tool, as it offers not only size information, but can also be used to determine the shape and crystal structure of the investigated clusters.

In this section, measurements using an alternative method are presented. A quadrupole mass filter (QMF) was used to determine the cluster size-distributions for the charged part of the cluster beam. The main advantage of this method is the possibility to measure a full mass spectrum in a few minutes, without the need to break vacuum or change any substrates. However, it was limited to the charged part of the clusters, since this setup did not use any system for active ionization. Also, it was limited to analyze particles with a maximum mass of $3 \cdot 10^6$ amu, which corresponds to silver clusters with a diameter of about 10 nm. For silver clusters from a GAS, and by this also for the Cluster Source in this work, the liquid drop model [9] is assumed. It can be used to calculate the cluster diameter

$$D = 2r_w \sqrt[3]{N}\,, \tag{5.2.2}$$

where r_w is the Wigner-Seitz radius (for silver $r_w = 0.166$ nm) and N is the number of atoms in the cluster. In brief, this assumes that the cluster is build up from atoms with uniform distances equal to the volume lattice constant. This introduces a small error, because a change in lattice constant for nanoclusters is known in the literature [61, 67]. The experiments where done at the University of Greifswald in cooperation with Marina Ganeva from the group of Prof. Hippler from the University of Greifswald and Sven Bornholdt from the group of Prof. Kersten from Kiel University. All of the results shown in

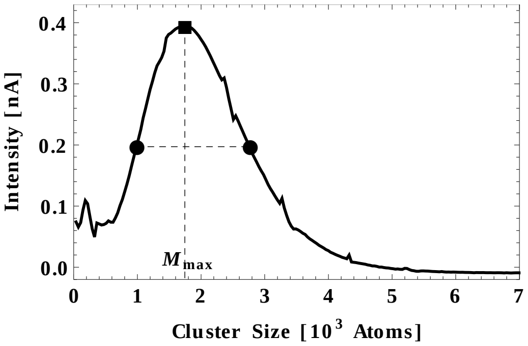

FIG. 5.11: Typical cluster size distribution (solid line) measured using the QMF-200. The black square indicates the point of maximum intensity. Black circles are the half-maximum points. From Ganeva et al. [v]

this section were published by Ganeva et al. [v] and parts of this section are excerpted from the paper.

Figure 5.10a shows a schematic of the QMF. It was connected to the Cluster Source via an additional chamber for differential pumping, since the QMF could only work in a pressure lower than 0.1 Pa. Between this additional chamber and the QMF a pinhole with a diameter of 5 mm was mounted. The main functional part of the QMF were the four rods, that were used to generated an electrical field to filter the ions. They were connected in pairs, as shown in figure 5.10b, and an AC voltage of $\pm(U + V{\cdot}\cos 2\pi f t)$ was applied to them. U and V are the amplitudes of the DC and AC components of the voltage, respectively, and f is the frequency of the AC modulation. Assuming single charged ions, the mass of the ions that pass the filter can be calculated to

$$M = 7 \cdot 10^7 \, \frac{kV}{f^2 d^2} \, , \tag{5.2.3}$$

where d is the diameter of the rods and $k = 1.30$ a correction factor for this instrument. In all experiments the ratio of U to V was held constant, because it determines the width of the mass range that can pass the filter:

$$\frac{\Delta M}{M} = 7.936 \left(0.16784 - \frac{U}{V} \right) \tag{5.2.4}$$

With the used value of $U/V = 0.1$, the resolution of the filter was $\Delta M/M = 0.54$.

A typical mass spectrum that was recorded in this way can be seen in figure 5.11. In the following, only the relevant data points that are marked in the figure will be discussed: First the maximum of the distribution, corresponding to the most probable cluster size. Second the points at the half-maximum, which are used to describe the width of the distribution.

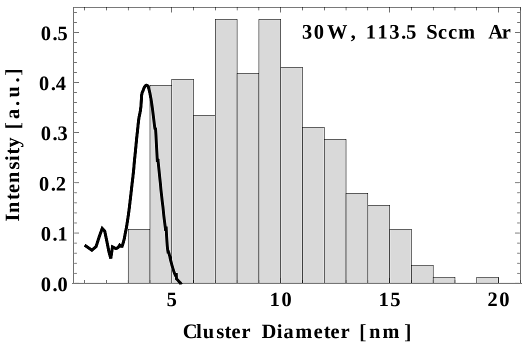

FIG. 5.12: Comparison of size distribution of clusters in the beam measured using the QMF (black solid curve) with deposited film analyzed using TEM (gray histogram). From Ganeva et al. [v]

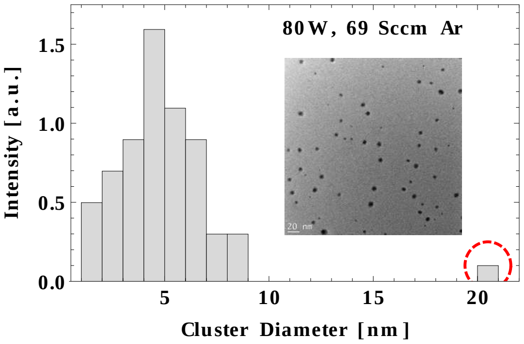

FIG. 5.13: Deposition of mass selected clusters. The selected cluster size is approximately 5 nm. The red dashed circle indicates large clusters formed by aggregation on the surface. From Ganeva et al. [v]

At first the question of comparability of the two measurement techniques TEM and QMF was investigated. In figure 5.12 the cluster size distribution measured by both methods at the same parameters of the source is shown. Here, the main problem of the QMF is visible: Because a big fraction of the produced clusters were larger than the detection range of the QMF, only a small part of the size distribution can be seen in the QMF measurement. This should be kept in mind for all results that are shown in this section. Another problem is the fact that the QMF can only detect charged clusters. Especially for the interpretation of the cluster beam intensity this can cause huge errors, because the percentage of charged clusters varies between 10 and 80 %, depending on the employed parameters. To check the general validity of the QMF results, a sample was deposited behind the mass filter unit. During the whole deposition, the filter was running at constant parameters, only allowing clusters with a mass in the range around 5 nm to pass. Of course, also all neutral clusters could still reach this substrate during deposition, but their deposition rate is very low, because of the large distance of about 1 m from the Cluster Source to the substrate. On the other hand, the charged clusters that pass the mass filter are focused again and thus have a much larger deposition rate on the substrate. Subsequently, this sample was analysed using TEM and the result can be seen in figure 5.13. Like it was expected, clusters with a distribution around 5 nm in size are found on the sample. Additionally, very few clusters with a much larger size can be seen, which could be caused by aggregation on the surface. The low amount of these surface aggregated clusters support the conclusion drawn earlier, that surface diffusion and aggregation can be neglected for samples with a low surface coverage.

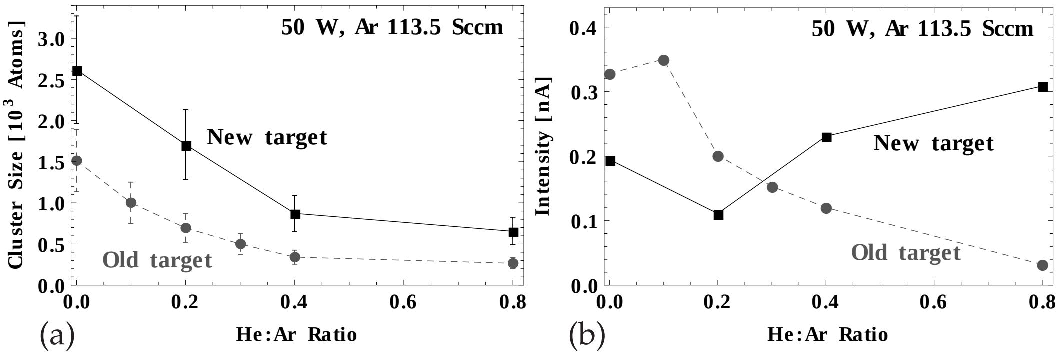

FIG. 5.14: Influence of the target age on (a) the most probable cluster size and (b) maximum cluster ion intensity. The black square symbols (solid line) represent the measurements carried out with a new target and the gray filled circles (dashed line) the used target with a deep sputtering trench. The error bars indicate the QMF resolution. From Ganeva et al. [v]

Another general obstacle for the comparison of results obtained by QMF measurements of clusters is the influence of the target age on the resulting clusters. With time the sputtering trench in the target gets deeper and after a maximum the effective sputtering rate decreases slowly. And because the cluster growth process depends strongly on the density of free metal, the size of clusters lessens until at some point the cluster growth stops completely. This effect is depicted in figure 5.14, where the size distribution and cluster beam intensity for an old target with a deep sputtering trench and for a new target without a sputtering trench are compared. It can be seen, that the general behavior, a decrease in cluster size with helium addition, is the same in both cases. Still the clusters produced using the older target are smaller for all parameters. The change in number of clusters is a more complicated case. To understand this dependence, it should be considered that not only the size shrinks with all other parameters constant. Quite the opposite is the fact: The change in sputtering trench not only influences the amount of free metal atoms, but also their angular emission distribution from the target and by that also their spatial distribution inside the Cluster Source. It has to be expected, that this can introduce a quite complicated change in the whole cluster growth process. Also, it should be noted that even in the case of small helium additions, where the number clusters emitted using the older target is higher by a factor of 1.6, the size of the clusters is smaller by factor of 1.8, leading to a net decrease in emitted cluster mass by a factor of about 0.88.

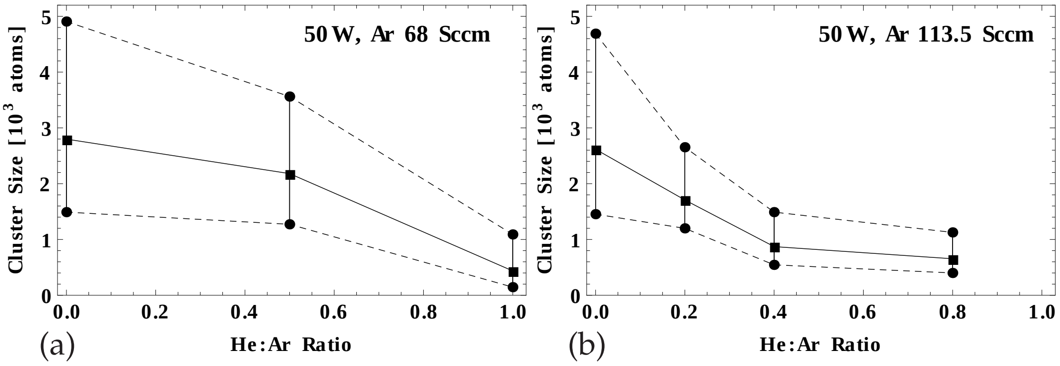

FIG. 5.15: Influence of the helium-to-argon flux ratio on the cluster size distribution measured by the QMF-200, with a varying helium flow rate, a discharge power of 50 W, and a constant argon flow rate of (a) 68 sccm) and (b) 113.5 sccm, respectively. The squares indicate the cluster size with maximum intensity (most probable cluster size). The circles represent the cluster sizes at the half-maximum points of the mass spectra. From Ganeva et al. [v]

Overall, the effect of changes in sputtering trench pose a hindrance when results from measurements at different conditions are compared. For measurements that are done in a row, however, this effect is neglectable, and because of this all results shown in the following are derived from such experiments. Of course, this applies not only to the investigations done with QMF, but to also to all sample depositions using the Cluster Source. While the change in deposition rate can be measured and corrected using a quartz microbalance, the change in size distribution can not be checked easily for every deposition. To estimate the magnitude of this effect it should be noted that a target typically lasts for $\approx$ 1 kWh, while a normal deposition takes only $\approx$ 1.5 Wh, including target cleaning. A noticeable difference in sample properties is earliest expected after about 0.1 kWh [19] or 60 samples, which is far more than the amount of produced samples for most investigations.

The influence of helium on the cluster size was investigated in more detail. In figure 5.15 the evolution of the cluster size with changes in the helium addition can be seen for several different argon flow rates. Like it is expected from the literature [23, 58], the cluster size shrinks with increasing helium flux, and at the same time the distribution also gets narrower. This behavior is the same for all used argon flow rates. Figure 5.16 shows the intensity of the cluster beam at these parameters. Here, a change in behavior can be observed between different argon flow rates. While the intensity decreases with helium addition at low argon flow rates, it seems to have a different and more com-

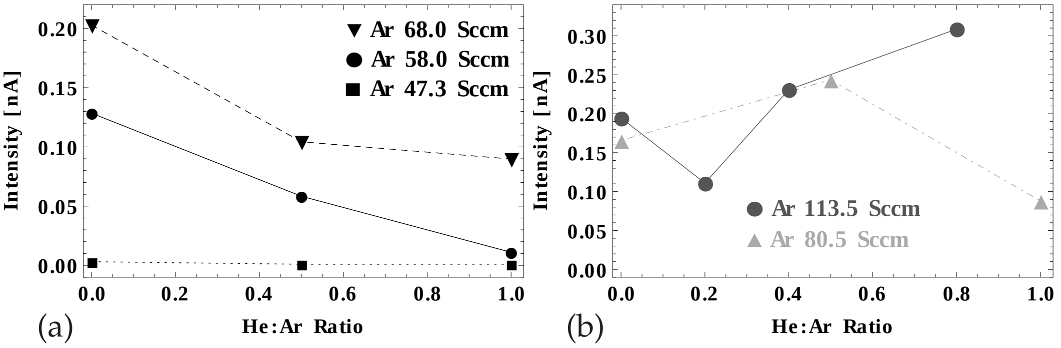

FIG. 5.16: Influence of the helium-to-argon flux ratio on the maximal intensity measured by the QMF-200 with a varying helium flow rate, a discharge power of 50 W, and an argon flow rate of (a) 47.3 to 68 sccm and (b) 80.5 to 113.5 sccm. From Ganeva et al. [v]

plicated behavior at high argon flow rates. A possible explanation for this was suggested by Pratontep et al. [58]: Helium helps to stabilize nucleation seeds, which results in more smaller clusters. But at the same time helium also allows for faster cluster growth and cluster coalescence, which creates larger clusters. These two processes are competing for number and size of clusters, and depending on the other parameters the balance of power between them can be shifted.

As a last step, the change of size and numbers of clusters with varying argon flow rate was measured. Figure 5.17 shows the results of this measurements. In the left side the dependence of the size distribution on the argon flow rate can be seen. The drop in the cluster size at an argon flow rate of 60 sccm is not expected in line with the currently available theories. It can only be explained by a mistake or error during the measurement. A maximum around 80 sccm and the subsequent drop for higher flow rates however fits to previous experiments with the open source and also, at least qualitatively, to known literature [23, 58].

Turning to the right part of the figure, the evolution of the cluster beam intensity with a variation in the argon flow rate can be seen. For low flow rates until 50 sccm, which corresponds to about 100 Pa pressure in the Cluster Source, the measurable intensity is very low, but constant. Beyond this point, the intensity rises dramatically and stays at a high level with only small variations. Again, this result is in accordance with previous results using the quartz microbalance at the setup in Kiel. The behavior is mostly governed by the different focus of the cluster beam. With higher flow rate the cluster beam

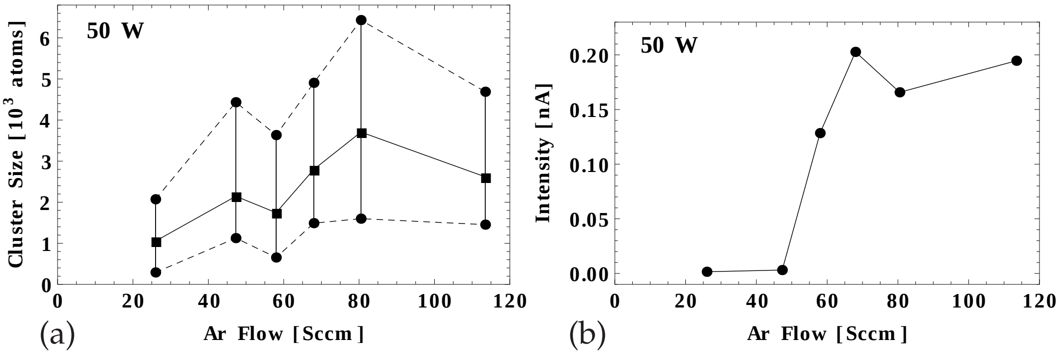

FIG. 5.17: Influence of the argon flow rate on (a) the cluster size distribution and (b) the maximal intensity. The black filled squares in (a) represent the most probable cluster size and the black circles represent the cluster size at half-maximum points. From Ganeva et al. [v]

is concentrated in a smaller angle and thus the amount of material that enters the QMF in an area that allows transmission increases.

In conclusion the Cluster Source that was designed and used during this work produces reproducible results. The obtained results are in most cases in line with the current theory and predictions. And again it was verified that the determination of the cluster size distribution is possible using TEM measurements, at least for samples with a low silver concentration. With this experiment the investigation of the silver cluster generation for the Cluster Source is concluded.

5.3 Nanocomposites

Combining the Cluster Source with a growing matrix allowed the deposition of nanocomposite thin films with variable cluster size distribution and density. To realize this, the cluster were directed onto a sample holder that was mounted opposite of the Cluster Source. A secondary plasma was ignited around this sample holder using an RF-magnetron. By injecting HMDSO into this secondary plasma, a $SiO_XC_YH_Z$ film could be deposited simultaneously with the cluster deposition. Characterization of such nanocomposite samples is challenging, as they are mostly insulating and consist of different materials in unknown concentrations. For this reason, TEM, SEM, and EDX measurements are the most important tools, because the desired information about morphology and composition can be obtained by them. The SEM/EDX mea-

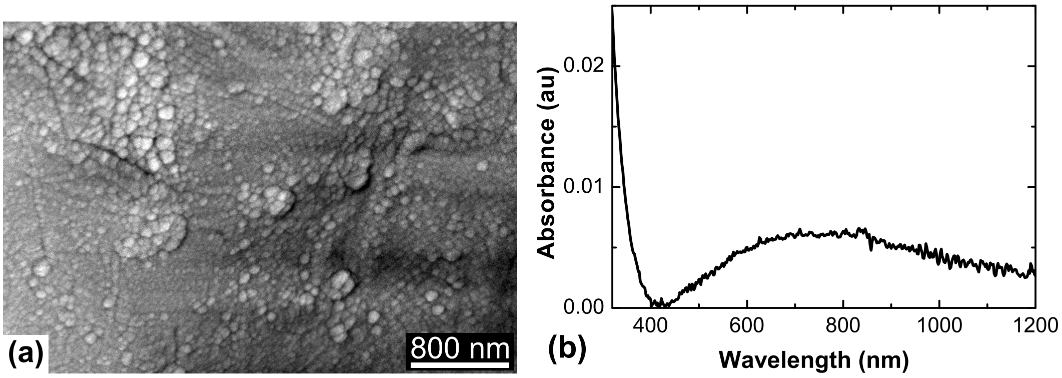

FIG. 5.18: (a) SEM image and (b) UV-Vis absorption spectrum of two $SiO_XC_YH_Z$ samples without silver. The sample in (a) has a thickness of 290 nm, while the one in (b) has a thickness of 115 nm.

surements presented in this section were done by Viktor Schneider and David Haffner using a Zeiss Ultra plus SEM/EDX device.

Figure 5.18 shows an SEM image and an absorption spectrum of two pure $SiO_XC_YH_Z$ films without silver clusters as reference. The film in (a) was deposited with a power of 5 W, an argon flow rate of 100 SCCM, resulting in an argon partial pressure of 0.77 Pa, a 0.2 Pa of HMDSO partial pressure, and a deposition time of 200 s. For the second sample in (b), the HMDSO partial pressure was decreased to 0.2 Pa, the deposition time was shortened to 140 s, and the argon flow rate was changed to 105 SCCM, resulting in a partial pressure of 0.87 Pa. While the power did not show any significant influence on the film properties in any experiments, the HMDSO partial pressure could be used to control the deposition rate, which was proportional to the partial pressure. The chemical composition of the sample in (a) was determined by EDX to be 16 % oxygen, 71 % carbon and 13 % silicon. Of course, also hydrogen is present in this samples, but cannot be detected by many spectroscopic techniques, including EDX and XPS. The surface of the polymer is quite rough and some particles with sizes ranging from 50 to 180 nm are formed on it. This structure is expected from the literature and could be smoothened by treatment in a pure argon plasma [21]. By varying the pulse frequency and length of the HMDSO injection, it should be possible to obtain a smoother structure with less particles. However, this was not done in this work, because the focus was set on the composition of the produced nanocomposite samples. It can be seen in (b), that the absorbance of the film is quite low over the whole measured range, also no peaks or other features are present that could overlay the absorption peaks of the silver clusters.

Two basic types of samples can be deposited using this setup: First, 3D composites that consist of a homogeneous distribution of clusters in the matrix. By means of the independent control over the two deposition processes for silver clusters and plasma-polymer matrix, also gradients of cluster concentration or size are possible in this case. Second, layered composites that consist of alternating films of $SiO_XC_YH_Z$ matrix and silver clusters can be deposited. Of course, deposition of any combination such as layers of 3D composites alternating with pure matrix layers are possible and can be used depending on the desired application.

For 3D composite samples, the deposition rates of both processes are an important factor, because they limit the possible range of the cluster concentration and the total deposition rate. In order to achieve a maximum composite deposition rate, the Cluster Source should be operated a high pressure, yielding a small but intense cluster beam. Because composites with cluster concentrations down to a few percent may be desired, the matrix deposition technique has to be able to grow the matrix at least ten times faster than the pure cluster film is deposited. Since the Cluster Source can produce a beam of clusters with a deposition rate up to 0.5 nm/s, the matrix deposition should reach speeds of 5 nm/s and possibly more. For this reason, a direct plasma polymerization deposition of the matrix was chosen, where the film deposition takes places inside the plasma zone. In this configuration, the polymer forming radicals that are created in the plasma have an extremely short way to the film, and thus reach very high deposition rates over 10 nm/s easily. With this setup a nanocomposite sample with 10 % silver can be produced at rates up to 2.8 nm/s. In indirect deposition the sample deposition takes place outside of the plasma region. Here, the deposition relies on radicals that leave the plasma region to build up the polymer film. Naturally, this mode achieves lower deposition rates, but on the other hand suffers less from interaction between the cluster beam and the secondary plasma.

In direct deposition, the interactions between the cluster beam, which is partly charged, and the secondary plasma can lead to a number of problems for composite deposition. The kinetic energy of a cluster with a diameter of 10 nm is in the range of 200 to 300 eV. Hence, for total deflection of the cluster, a voltage in this range would be required, assuming single charge of the cluster. This will not be the case in a typical RF discharge with a power of 5 W and a bias voltage of about 30 V, like it was used in this experiment. Still, a part of the cluster beam will be deflected far enough, when passing the secondary plasma, to miss the sample. Also clusters that were neutral before can get charged in the secondary plasma, depending on the pressure and power of it, and the ion and electron densities following from this. Experiments have shown that such effects exists, but do not play a major role in practice, as they only reduce the silver amount slightly and are mostly reproducible.

Additionally, the secondary plasma can influence the growing and already grown film. To determine the magnitude of this effect, test samples with a 20 nm thick cluster-film were produced. These samples were treated in the

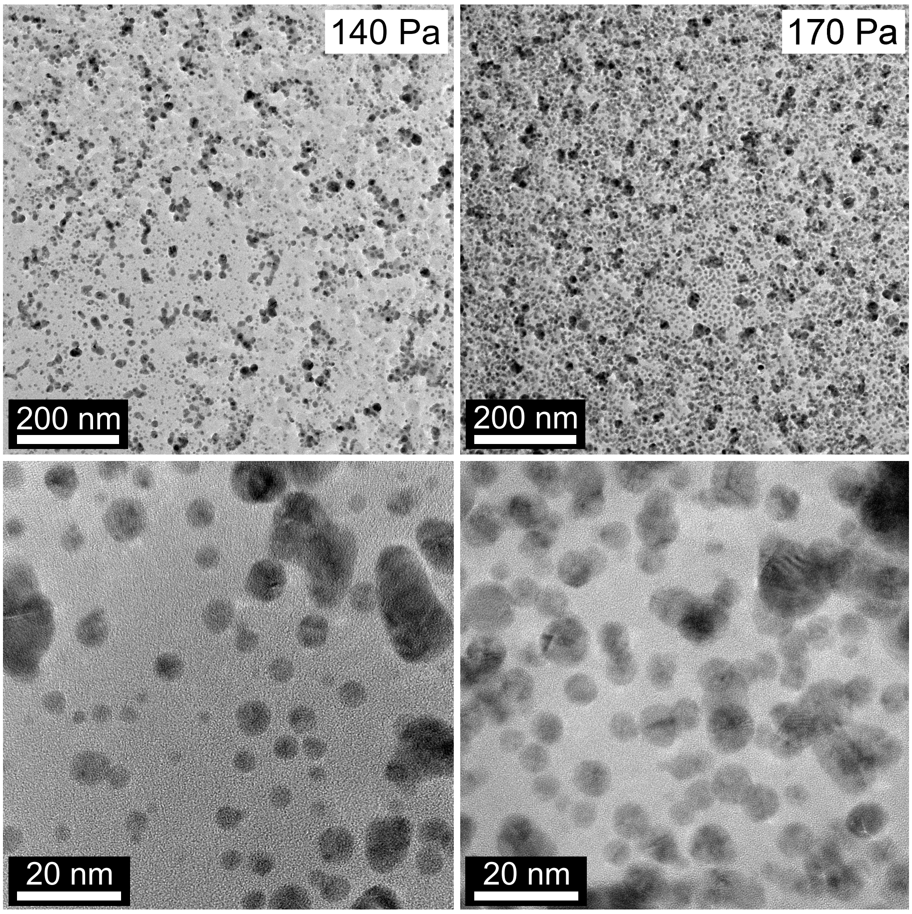

FIG. 5.19: TEM images of two silver/$SiO_XC_YH_Z$ 3D nanocomposite samples deposited with similar parameters, only differing in the gas flux and aggregation pressure: (left) 77.2 SCCM, 140 Pa and (right) 94 SCCM, 170 Pa.

secondary plasma using different parameters, and subsequently the amount of silver on all samples was compared to a reference sample using EDX. The deposition of a $SiO_XC_YH_Z$ layer without additional oxygen flux yielded no change in the measurable amount of silver. However, the treatment in a plasma with gas flows of 111 SCCM argon and 20 SCCM oxygen for 120 s, and the deposition of an $SiO_XC_YH_Z$ film using the same gas mix, decreased the amount of detectable silver by 10 and 20 %, respectively. This decrease is probably caused by charging and heating, which leads to erosion of the weakly bound silver clusters. Also this effect is small enough that it does not pose a serious problem in practice.

TEM images of two 3D composite samples are shown in figure 5.19. The samples were produced with identical matrix deposition parameters and a thickness of about 90 nm. Only the pressure inside the Cluster Source was

Pressure	Silver	Silicon	Oxygen	Carbon
140 Pa	3.0 %	21 %	50 %	26 %
170 Pa	5.3 %	24 %	42 %	20 %

Table 5.1: Composition of the 3D nanocomposite samples shown in figure 5.19.

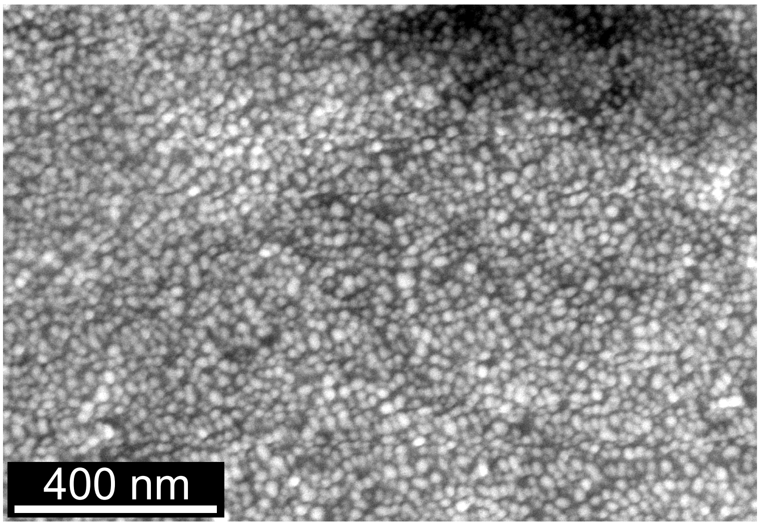

FIG. 5.20: SEM image of silver/$SiO_XC_YH_Z$ layered nanocomposite with a deposition time of silver of 67 s, corresponding to 7 nm cluster thickness.

varied from 140 Pa to 170 Pa. This led to a changed cluster beam focus width and thus to different concentrations of silver. The concentration of silver in the sample rises from 3.0 % to 5.3 %, according to TEM/EDX. Table 5.1 shows the composition of both samples. As expected, the matrix composition is very similar. It should be noted that the carbon concentration is only approximated, because the substrate used for the measurement is copper net coated with carbon (S160-3, Plano). Size and spatial distribution of the silver clusters is similar in both samples, since the sputtering power was not altered. Even if the cluster density in the images appears to be quite high, it should not be minded that the image is a projection of the 90 nm thick film. Therefore, the clusters in these samples are well seperated, which is also in line with the measured concentrations.

For the creation of layered nanocomposites the deposition rates of the single processes do not play such an important role. Here, the desired concentration can easily be obtained by varying the corresponding deposition times. Also, this method avoids interactions of the cluster beam and the growing film with the secondary plasma. On the other hand, the deposition time is longer,

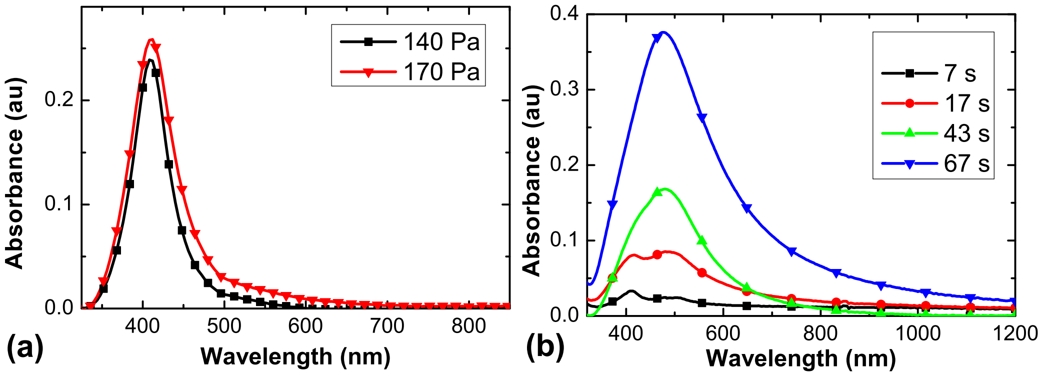

FIG. 5.21: UV-Vis absorption spectra of silver/$SiO_XC_YH_Z$ nanocomposite samples: (a) 3D composite samples, that are shown in figure 5.19. (b) Layered composites with varying silver-cluster deposition time from 7 to 67 s. The sample with 67 s of deposition time is shown in figure 5.20.

because the process, and with it possibly the gas flows, has to be switched between the alternating layers. In figure 5.20 an SEM image of a multilayer sample can be seen. It consist of one layer of silver clusters in between two $SiO_XC_YH_Z$-polymer layers. The silver clusters film has thickness of 7 nm, the $SiO_XC_YH_Z$ layers a thickness of about 45 nm each. Four samples of this layered type were deposited with similar deposition parameters, only the silver cluster deposition time was varied, to obtain different amount of clusters. The samples were created with 7, 17, 43 and 67 s of deposition time, which yields 1, 2, 4 and 7 nm of cluster film thickness.

Simulation done by Amendola et al. for plasmon resonance in silver nanoparticles with spherical and cylindrical shapes showed that non-spherical particles exhibit a double-peak resonance, because they have two non identical axes that can be excited [3]. Figure 5.21 shows the UV-Vis absorption spectra for the deposited 3D and layered samples. In part (b) of the figure, in the curve of the sample with 7 s deposition time a peak at 416 nm can be seen, as well as a broader second peak around 486 nm. The former corresponds to single non agglomerated clusters, while the latter broad peak can be explained by some agglomeration. In comparison with the spectrum of the 3D sample in (a), this first peak at 416 nm confirms that the clusters presented in figure 5.19 are well separated, as they do not exhibit broadening or secondary peaks. By means of agglomeration non-spherical clusters are created, that allow a second plasmonic excitation along the new longer axis at higher wavelength. With longer deposition time, the second peak rises in intensity and broadens, until at 67 s deposition time, only one broad peak can be seen. This is caused by increasing interaction between the individual clusters and further agglomeration of clusters. This gives rise to more possible plasmon excitations with different wavelengths, that overlap and thus lead to one broad continuous peak [17].

To conclude, the cluster beam deposition from the Cluster Source was combined with plasma polymerization to create nanocomposite samples. In comparison with the Open Source, the degree of control over the processes is much higher, and this setup especially allows independent control of cluster and matrix deposition. It was shown, that different types of nanocomposites can be deposited, which display the expected optical properties based on surface plasmon resonances of the silver clusters. Still, in this setup some parameters of both processes, such as the gas flows, are linked to each other. To overcome this, a third chamber for differential pumping would be needed, similar to the setup that was used for the QMF measurements, shown in the previous section. However, this would only be required if, for example, lower pressures for plasma polymerization are desired, or if another method for matrix deposition would be employed.

5.4 Titanium/Titanium Oxide Nanoclusters

The last part of this work deals with a special case of nanocluster formation: The chemical enhanced gas phase cluster aggregation process. In the previous chapter, silver was used for all experiments. Noble metals like copper, silver, and gold are well suited materials for use in a GAS [4], because of their high sputtering yield and moderate dimer binding energies. For applications other materials, such as titanium or cobalt, are also interesting. In the case of titanium, cluster formation is not possible under the same conditions as for silver, because of the low sputtering yield and also low dimer binding energy of titanium. Even at high discharge powers, the free metal density inside the Cluster Source is too low to achieve cluster growth. At the same time, the low dimer binding energy leads to a high probability that an already firmed nucleation seed will dissociate again. To overcome this problem, reactive gases can be used to allow cluster growth by creating more stable cluster nucleation seeds.

The basics of reactive cluster aggregation in a GAS will be presented in detail in the following. Afterwards, the use of pulsed DC power for this process will be discussed. It can lead to a drastically increased cluster deposition rate. Then, the properties of the titanium nanoclusters samples that were created using this process are shown. And this sections will be concluded with an outlook for possible application of these nanoclusters in photocatalysis.

For these experiments the same principal setup of the Cluster Source as before was used. Naturally, the silver target in the Cluster Source was substituted with a titanium target. To control the gas flow of oxygen for the reactive cluster formation, two different methods were used: First a sensitive needle valve and second an additional automatic gas flow controller for low gas fluxes from 0.05

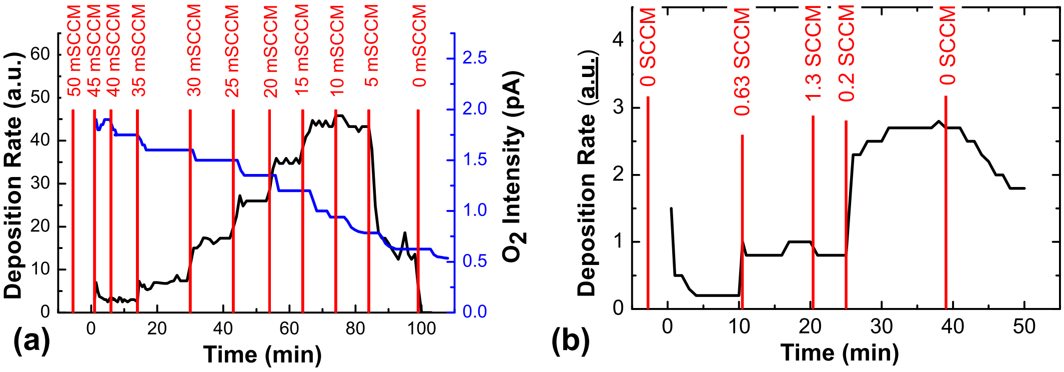

FIG. 5.22: Time evolution of the cluster deposition rate with a varying reactive gas flow for (a) titanium with oxygen (argon flux 80 SCCM, 150 Pa) and (b) for cobalt with nitrogen (argon flux 100 SCCM, 178 Pa). For titanium/oxygen, on the right axis the intensity of oxygen (O_2, 32 amu) is shown, measured with a mass spectrometer. A gas flux of 10 mSCCM oxygen corresponds to a partial pressure of 0.027 Pa and a gas flux of 0.2 SCCM nitrogen corresponds to a partial pressure of 0.54 Pa.

to 1 SCCM (purchased from Apex). Both methods could be used to control the oxygen gas flows in the interesting range between 0.05 and 0.2 SCCM. For in-situ monitoring of the gas composition, a mass spectrometer was mounted in a separated chamber, which was connected through a valve with the deposition chamber. The chamber of the mass spectrometer was pumped separately using a turbo molecular pump (Pfeiffer HiPace 80), because a pressure of lower than $5 \cdot 10^{-3}$ Pa was needed for the operation of the mass spectrometer. Most of this experiments were conducted in cooperation with Oleksandr Polonskyi. Additionally, some measurements were done in cooperation with Amir Mohammed Ahadi. The experiments with cobalt were done by Björn Gojdka in a different chamber, there the same Cluster Source design was used, and thus the obtained results can be compared. Many results that are presented here were published by Peter et al. [ii] and Polonskyi et al. [vi], excerpts from this publications are used in the following. The SEM measurements presented in this section were done by Vladimir Zaporojtchenko using a Zeiss Ultra plus SEM device.

5.4.1 Reactive Cluster Formation

It was first reported by Marek et al. [43] that the admixing of oxygen can increase the deposition rate of titanium cluster in a GAS. This effect of oxygen admixing on the titanium cluster deposition rate is shown in figure 5.22a. If a high flux of oxygen is let into the chamber, the titanium target is in ceramic mode, and no cluster deposition can be monitored. Upon decreasing the oxy-

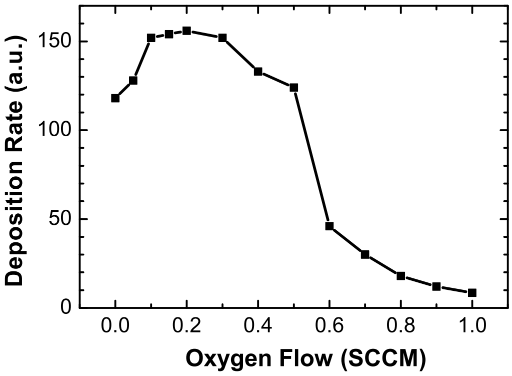

FIG. 5.23: Dependence of cluster deposition rate on oxygen gas flow for silver.

gen flow, the target will switch to metallic mode, and below 50 mSCCM a deposition rate can be measured. The deposition rate increases with decreasing oxygen flow, until an optimal flow of about 10 mSCCM is reached, that yields the maximum titanium cluster deposition rate. Decreasing the flow rate further leads to a drop in deposition rate, and without oxygen no deposition can be measured at all.

Figure 5.22b shows a similar behavior of nitrogen admixing on cobalt. Without additional nitrogen, in high vacuum conditions after bake-out, a low deposition rate of cobalt clusters is observed that decreases over time. After bake-out of the vacuum system and cleaning of the target, no deposition rate would be measured at all at this point. The low deposition rate after bake-out, but without cleaning the target, is an effect of reactive gas that is adsorbed on the target and is released during sputtering. This effect will be discussed in more detail later. When nitrogen is let into the aggregation source, the deposition rate rises and is stable over time. Again, going to lower flow rates yield a higher deposition rate, and a maximum at approximately 0.2 SCCM. Without reactive gas the deposition rate decreases gradually over time.

Also materials that exhibit high cluster deposition rates without reactive gas, still can show an increase in rate with oxygen admixing. With silver an increase in the deposition rate of about 32 % can be achieved, as it is shown in figure 5.23. However, in the case of silver, the system reacts much faster to a change in oxygen flow. Typically a stable deposition rate is reached in 10 to 30 s, while this process can take up to 15 minutes for titanium.

From this data it can be concluded that the presented systems show the same behavior in regard to reactive gas influence on cluster deposition rates, however on different scales of time and gas flux. The very low deposition rate at high reactive gas flow can be understood in terms of well-known reactive sputtering phenomena. A high reactive gas flow causes oxidation or nitridation of the target surface, which leads to the formation of a dielectric layer on

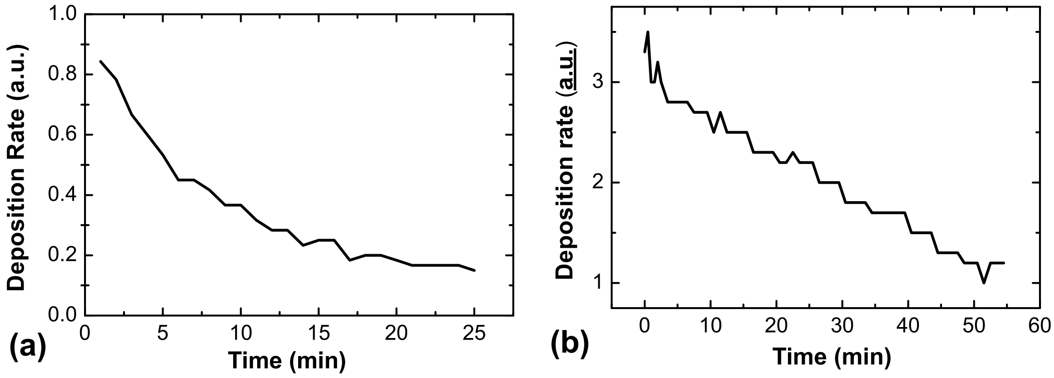

FIG. 5.24: Decrease of deposition rate with sputtering time at constant discharge and gas parameters, for (a) titanium and (b) cobalt. The experiments started directly after venting and pumping the chamber, without baking it out. Water and carbon oxide contaminations are sources for oxygen and are used up over time.

top of the target, and consequently reduces the sputtering yield. In this state, not enough metal is sputtered to create a sufficient free metal density in the gas phase to achieve stable cluster formation and growth in the gas phase. The reason for the significant increase of the deposition rate at lower reactive gas fluxes is, however, not obvious and will be discussed in the following.

Like it was pointed out above, the residual gas concentration is frequently already sufficient for cluster formation. Therefore, it is of interest to see the typical behavior of a gas aggregation source if no reactive gas is added. Figure 5.24a depicts the time evolution of the deposition rate without additional oxygen for titanium clusters. Prior to this experiment, the chamber was vented and then pumped down to 10^{-5} Pa. Subsequently, the discharge was started at 200 Pa argon and a declining deposition rate is observed. The steady decrease suggests, that a residue of oxygen in the chamber is being used up in the process of cluster formation. The most probable sources for oxygen are water and carbon oxides, on the walls of the GAS, that start to gas out because of electron and ion bombardment when the discharge is started. A similar trend is observed for cobalt clusters, shown in figure 5.24b. In this case, cobalt cluster formation is probably also be driven by oxygen rather then nitrogen.

If the system is baked out to $8 \cdot 10^{-6}$ Pa prior to the experiment and no reactive gas is added to the discharge, a cluster production rate is observed only for a short time of about 2 minutes. In this case, no oxygen is provided from the chamber walls due to the bake-out. Thus, the short non-zero deposition rate can be attributed to oxygen or nitrogen chemisorbed on the target itself. The reactive gas gets released during the sputtering process, and is then available for gas phase cluster formation. Once the target surface is sputtered clean,

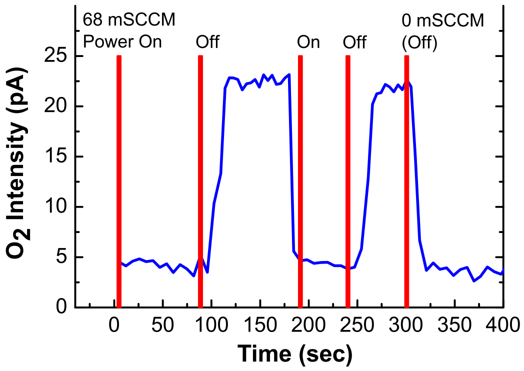

FIG. 5.25: Intensity of oxygen (O_2, 32 amu) measured by a mass spectrometer over time with and without running discharge. The discharge was run with a constant argon and oxygen flow of 36 SCCM and 68 mSCCM, respectively, at a power of 100 W. The power was switched on and off as indicated by the red bars (the intensity scale differs from the scale of figure 5.22a).

no reactive gas is left to sustain the cluster formation, and accordingly the rate drops to zero until reactive gas is added to the process.

Another hint that oxygen is steadily consumed in cluster growth is given in figure 5.25. In this experiment, the partial pressure of oxygen in the process atmosphere was measured using a mass spectrometer. The discharge was operated at a constant power and flow of argon, the flow of oxygen was chosen to yield stable cluster production. After 80 s the discharge was stopped, and a rise in the oxygen signal was observed. Once the discharge was started again, the oxygen signal dropped to the initial value. This behavior was highly reproducible. After 300 s the oxygen flow was finally stopped and the discharge was turned off. In this case the signal drops to the same value as before in the presence of the discharge. Thus it can be concluded, that during the sputtering operation oxygen is steadily consumed by processes in the GAS.

The results of the experiments suggest that oxygen binds with titanium atoms forming stable titanium oxide molecules. Subsequently, the latter serve as nucleation centers for the growth of titanium clusters. Accordingly, the oxygen is consumed as long as there are free titanium atoms, i. e. as long as the discharge is running. In the case of the optimal, very low, oxygen concentration, which yields the maximum deposition rate, the added oxygen is mostly consumed in the gas phase and is not sufficient to oxidize the target, and switch the sputter process to ceramic mode. A lower flow of oxygen will result in a lower cluster deposition rate, because less titanium can be bound into clusters due to the lack of nucleation sites. In contrast, a higher oxygen flow than the optimal one will lead to an excess of oxygen which cannot be bound into cluster sees and therefore will oxidize the titanium target. The lat-

Material	Silver	Copper	Titanium	Cobalt
Dimer binding energy (eV) [26]	1.688	2.083	1.219	<1.316
Oxide binding energy (eV) [26]	2.29	2.979	6.908	2.168
Nitride binding energy (eV) [84]	-	-	-	4.119
Sputtering yield [44]	1.3	0.9	0.2	0.5

Table 5.2: Binding energies and sputtering yields for silver, copper, titanium, and cobalt. The sputtering yields are taken for an ion energy of 200 eV, which corresponds to a discharge voltage of about 285 V, a typical value for the Cluster Source.

ter is a well known process, that leads to lower a sputtering yield and can also be observed as a rise in bias voltage of the discharge.

There is a difference between the behavior of materials like titanium and cobalt on the one hand, and copper and silver on the other hand. While the former show a strong dependence on the reactive gas flow, and no cluster deposition at all without it, the later show only a small change in cluster deposition rate with varying reactive gas flux. The difference can be explained by the diatomic binding energies and sputtering yields of the different materials. Table 5.2 shows the sputtering yields, dimer and oxide binding energies for the discussed materials, and for cobalt also the nitride binding energy. This data can be used to explain the observed effects: Without reactive gases, copper is more likely to build stable clusters than titanium, because it will produce more free metal atoms due to the much larger sputtering yield. Also, the formation of stable cluster seeds will be much more likely, as they have a lower probability to dissociate again. However, with the addition of oxygen the situation is reversed. Now the binding strength for titanium-oxygen is much higher than that for copper-oxygen, which results in very efficient generation of stable cluster seeds for titanium. For cobalt, the values fit the same behavior as titanium with oxygen, but in a less dramatic form. The cobalt oxide dimer has a bit lower binding strength than cobalt nitride, but still almost a doubled binding energy compared with the pure cobalt dimer. This explains the effect of cluster growth without nitrogen in a not baked-out chamber. In this case, there are still water residues that release oxygen when the plasma is ignited, supporting the cluster formation. Another effect that plays a role in this is the increase of sputtering yield with slight oxidation the target [40, 41]. According to this, low concentrations of oxygen can lead to an increase of up to 40 % in sputtering rate. While this ca not explain the influence of reactive gas on its on, it is probably a contributing factor.

The difference in the optimal reactive gas flux for titanium and cobalt can be explained with these values as well: The sputtering yield of cobalt is more than twice than the sputtering yield of titanium, and also the bonding strength

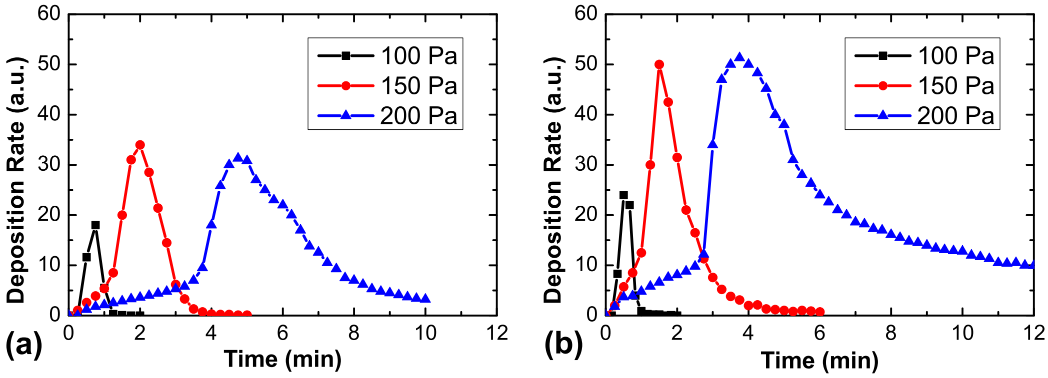

FIG. 5.26: Time evolution of the titanium nanocluster deposition rate at (a) 75 W and (b) 100 W power for different sputtering pressures, after 2 minutes of oxygen treatment with 2 SCCM oxygen at 50 W power and 100 Pa argon.

of cobalt-nitrogen is much smaller than for titanium-oxygen. This means that a cobalt target is less likely to be poisoned by nitrogen than a titanium target with oxygen, because of a lower sticking coefficient of nitrogen atoms arriving at the target. Additionally, with the higher sputtering yield a larger amount of physisorbed reactive gas can be sputtered away from the target. This allows a higher reactive gas flux without poisoning of the target.

To gain more insight into the relationship between reactive gas flow and cluster formation, further experiments with titanium and oxygen were conducted. 2 SCCM of oxygen were led into the Cluster Source for 2 to 8 minutes, while a discharge was running at 50 W power with 100 Pa of argon as working gas. After this oxygen rich process, the oxygen flow was stopped completely and the cluster deposition rate was measured. Figure 5.26 shows the time evolution of the deposition rate after the oxygen injection. Directly after the oxygen injection, the discharge is running at a high voltage up to 350 V, at constant power of 100 W, and no cluster deposition rate is detected. After a delay of 30 s to 6 minutes, depending on discharge parameters, the deposition rate rises. The delay until the deposition starts is longer for higher pressures, this is probably caused by a lower sputtering rate at higher pressures [79]. With a lowered sputtering rate it takes longer to sputter through the oxide layer on top of target and reach the metallic part. When the deposition rate reaches its maximum, the voltage drops down to 200 V and then stays constant. After the maximum, the deposition rate goes down to zero. The behavior is slightly different for a argon pressure of 200 Pa. Here, a deposition rate is measured already after a very short delay, but the maximum follows later, compared to a lower pressure of 150 or 100 Pa. Also, the shape of the peak is different. While the curves for the two lower pressures can be approximated with a Gaussian, the curve at 200 Pa represents the sum of two superimposed Gaussians. The

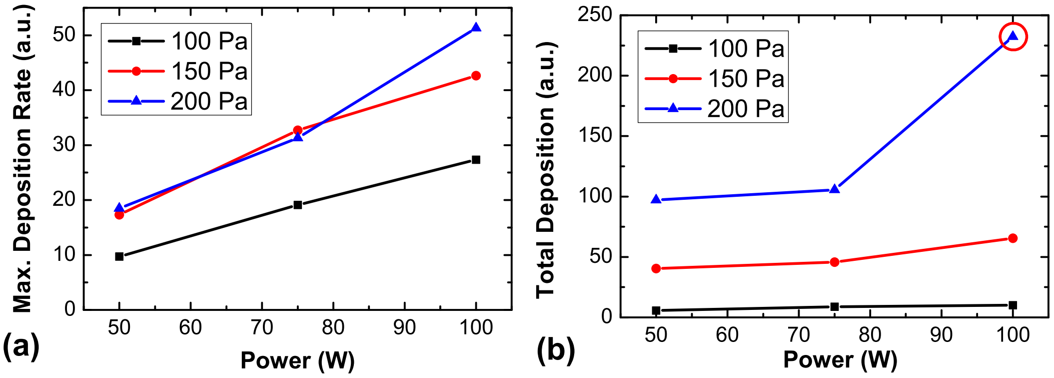

FIG. 5.27: The change in (a) maximum deposition rate and (b) total deposition amount in dependence of the discharge power and argon pressure. After 2 minutes of oxidation with 2 SCCM oxygen at 50 W power and 100 Pa argon. For 200 Pa is system is behaving partly different, for yet unknown reasons (red circle).

origin of the latter effect needs further investigation and can not be explained with the current data.

Figure 5.27a shows the maximum deposition rate obtained for different argon working gas pressures in dependence of the discharge power. For all pressures the maximum in deposition rate rises approximately linearly with the discharge power. This appears coherent, since a higher discharge power leads to higher sputtering rate and thus will lead to a higher amount of material deposited as clusters. As most of the oxygen, that is available for cluster formation, is coming from the target, both oxygen and titanium are released faster when operating at a higher power, and thus yield a higher cluster production rate. However, here we can not differentiate between a rise in number of clusters or an increase in cluster size, because the quartz microbalance only measures the total deposited mass.

In figure 5.27b, the integrated deposition from the same experiments is shown. The data was obtained by integrating curves like the ones shown in figure 5.26. It appears that the total amount deposited is constant with respect to power for both low-pressure cases. This indicates that the same number of atoms is bound into clusters and only the time evolution of the cluster formation is influenced by the power.

A possible explanation of this behavior is based on a cluster growth rate that is limited, and in the time while clusters travel through the GAS they can only gain a certain amount of material. Thus, the total amount of mass can only be influenced by a change in number of cluster seeds, which are controlled by the amount of oxygen.

Accordingly, most of the sputtered titanium atoms will either return to the target or condensate on the walls of the Cluster Source and will not be detected

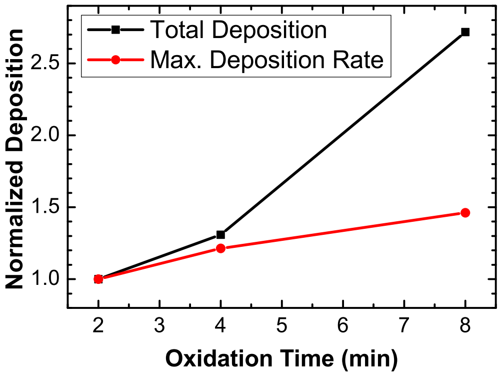

FIG. 5.28: Normalized change in maximum deposition rate and normalized total deposition amount at 50 W power and 150 Pa argon pressure, after varying times of oxidation with 2 SCCM oxygen at 50 W power and 100 Pa argon.

on the quartz microbalance. Again, for the case of 200 Pa we see a somewhat different behavior. The area under the curve for 200 Pa is taken from the whole curve, including also the broad peak that is not present for lower pressures. Like it was stated before, no explanation of this behavior can be given at the current time.

To vary the total amount of deposited mass, the amount of initially provided oxygen has to be changed. This can be done by changing the time of oxygen treatment, as shown in figure 5.28. Again, this supports the hypothesis that reactive gas is needed for cluster seed formation and stabilization. Thus, the amount of oxygen directly controls the amount of material grown in clusters. In agreement with the results presented above, the deposition rate maximum only rises slightly when the oxidation time is increased at constant power.

The data clearly demonstrate that the operation of a GAS for reactive metals like titanium and cobalt depends critically on the reactive gas supply, and that the results obtained will vary if the history of reactive gas supply is different. Therefore, it does not seem to be possible to get reproducible results for a GAS used without a precisely controlled supply of reactive gas. It is shown in figure 5.22, that it is possible to achieve stable cluster production at high rates with a critical amount of reactive gas flux.

5.4.2 Pulsed DC Reactive Cluster Production

It is common in normal reactive sputtering to use pulsed DC power in order to achieve a more stable process. In this setup, the voltage which is used to run the discharge is modulated by a square wave, and the voltage is only applied for a short time τ_{on}. Alternating to this, the target is left on floating potential for

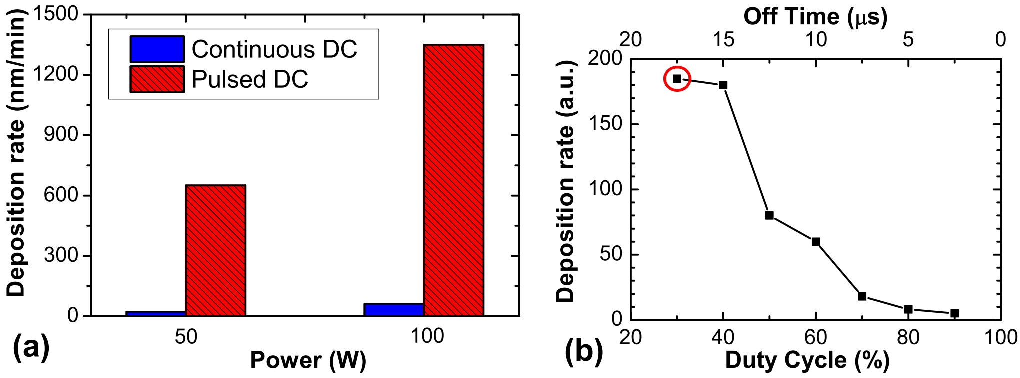

FIG. 5.29: (a) Comparison of maximum possible deposition rates of continuous and pulsed DC for 50 and 100 W at 200 Pa of argon and an optimal oxygen partial pressure in each case. The deposition rate applies to the position of the QMB, in the center of the chamber. (b) Dependence of the deposition rate on the duty cycle using pulsed DC power with a discharge power of 50 W, a oxygen partial pressure of 0.04 Pa and an argon pressure of 200 Pa.

the rest of time (τ_{off}). During τ_{on}, the sputtering takes place, while during τ_{off}, electrons are accelerated towards the target by the potentially accumulated surface charges, and negate them. Since no external voltage is used for the electron acceleration, the process stabilizes itself with a varying thickness of the insulating layer on the target and varying charge that accumulated during the sputtering interval.

A setup for pulsing of the DC power was constructed by Rainer Kloth from our group. It consisted of a power MOSFET (HTS 31 with cooling fins, Behlke electronics), that was used to switch the magnetron DC power supply (MDX 500, Advanced Energy). Frequencies up to 100 kHz were possible, with 20 to 50 kHz being used typically. The possible range for the ratio of τ_{on} to τ_{off}, the duty cycle, is in principle only limited by thermal constraints of the MOSFET. However, as the used power supply is not intended for pulsed power, it includes feedback control, for example to suppress arcing and to achieve a stable continuous power. For this reason some, frequency-duty cycle combinations are not possible using this setup. This includes especially frequencies above 40 kHz with duty cycles lower than 50 %.

Using pulsed DC power for reactive sputtering in the Cluster Source not only yields a more stable deposition. Also, it leads to a huge increase in deposition rate, as it is depicted in figure 5.29a. Here, the maximum deposition rates that could be achieved with continuous and pulsed power are compared. The values for continuous DC were reached by using the pre-oxidation technique that was shown in the previous section (cp. figure 5.26), while the results for pulsed power were achieved using a continuous flow of oxygen. This results were confirmed numerous times using the quartz micro balance and also by depositing films, which were analyzed using profilometry. An increase of more than a factor of twenty was quite unexpected from previous literature. Until now it is not completely understood what the origin of this effect is, yet a possible explanation will be presented in the following.

A fundamental difference to the previous shown continuous DC power is induced by the use of pulsed DC power. The sputtering power is concentrated in a shorter time, while the average power is held constant. This leads to a high power during τ_{on}, which will lead to a high sputtering rate in this time. Such a behavior is know in the literature for pulsed DC sputtering in a standard low pressure magnetron [48]. The cluster aggregation process relies heavily on the formation on stable seeds, which are created by metal-metal collisions in the gas phase. As this process has a quadratic dependency on the free metal density, a higher cluster deposition rate is expected when comparing continuous and pulsed DC with the same average powers. However, Stranak et al. investigated pulsed DC sputtering for copper cluster deposition and did not find any significant increase in deposition rate [71]. Similarly, experiments with silver showed no significant increase in deposition rate using pulsed DC in comparison with continuous DC. From these results it can be concluded, that the reason for the huge increase in deposition rate must be peculiar to the reactive cluster formation process.

Comparing this results with the data shown in figure 5.29b, leads to a possible explanation. Here, a rise in deposition rate with decreasing duty cycle, which implies a decreasing τ_{on}, is shown. The curve was measured starting at 90 % decreasing the duty cycle in steps of 10 %. The mesurement is not equal when reversed, because of the hystersis in the surface oxidation of the target. The circled data point at 30 % is most likely cause by limits in the electronics, that prevent the use of short duty cycles. Considering the fact that a change in sputtering rate cannot be the primary effect, reactive processes on the target that are influenced by sputtering are a likely candidate. In this mode, the target is partially poisoned, that is a very thin layer of titanium oxide exists on top of the pure titanium. Because of the vast difference in binding energy between titanium-titanium and titanium-oxygen, sputtering of a titanium-oxygen dimer will have a high probability in this case. If exactly one monolayer of titanium oxide exists on the top of the target, the energy needed to sputter either pure titanium, that is bound to oxygen, or pure oxygen, that is bound to titanium, is much higher than the the energy needed to sputter a titanium-oxygen dimer, that is bound to titanium. For this reason, using pulsed DC reactive sputtering in the GAS leads to unusual high amounts of titanium-oxygen dimers that are sputtered. Since they already constitute the needed nucleation seed for cluster formation, they enhance the cluster growth by a huge factor. If enough of this dimers are sputtered, they take away the necessity for the very unlikely and thus slow three-body collision, that is the

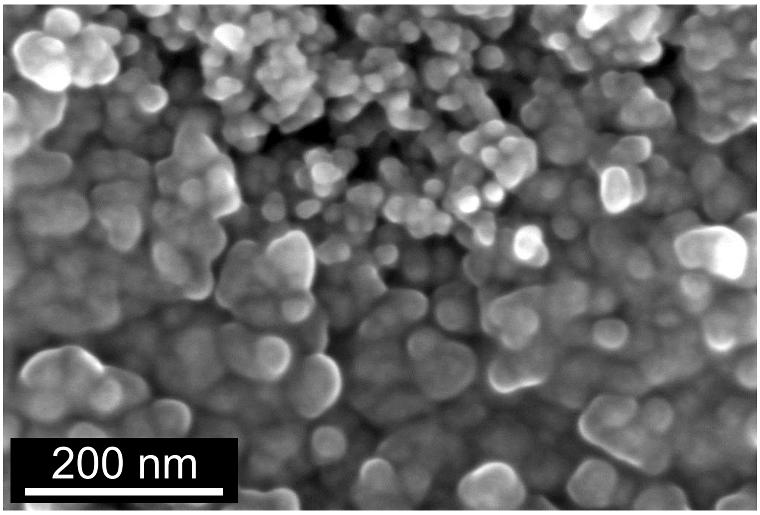

FIG. 5.30: SEM image of a titanium oxide nanocluster film deposited with pulsed DC using an average power of 50 W, an argon gas flux of 100 SCCM, a pulsing frequency of 40 kHz, a pulsing duty cycle of 50 %, a deposition time of 60 s, and a resulting film thinckness of about 250 nm.

first step of cluster formation. Of course, this scheme will only work in a small range of oxidation, because on the one hand enough titanium oxide has to be bound on the target to make a noticeable effect. And on the other hand the oxidation has to be sparse enough to not build up a closed titanium oxide film, as this would not allow the easy sputtering of singe titanium-oxygen dimers.

Although only this proposed model exists for the effect without a definite proof, this process is highly stable and reproducible. It was used in several experiments for the deposition of titanium oxide cluster samples, whose properties will be presented in the following section.

5.4.3 Nanocluster and Film Properties

Using the methods that were presented in the previous sections, thin film sample of titanium oxide nanoclusters were deposited. Due to the low amount of oxygen that is used during the deposition, the clusters that were generated in the Cluster Source were assumed to be made up mostly from metallic titanium. This assumption can be backed by a simple observation: A thin film of deposited clusters appears gray to black directly after the deposition, while it is still kept in vacuum. When the chamber is vented, to remove the sample, however, the film changes its appearance to completely transparent in a matter of seconds. Also, later analysis of the samples show that they consist of completely stoichiometric titanium dioxide.

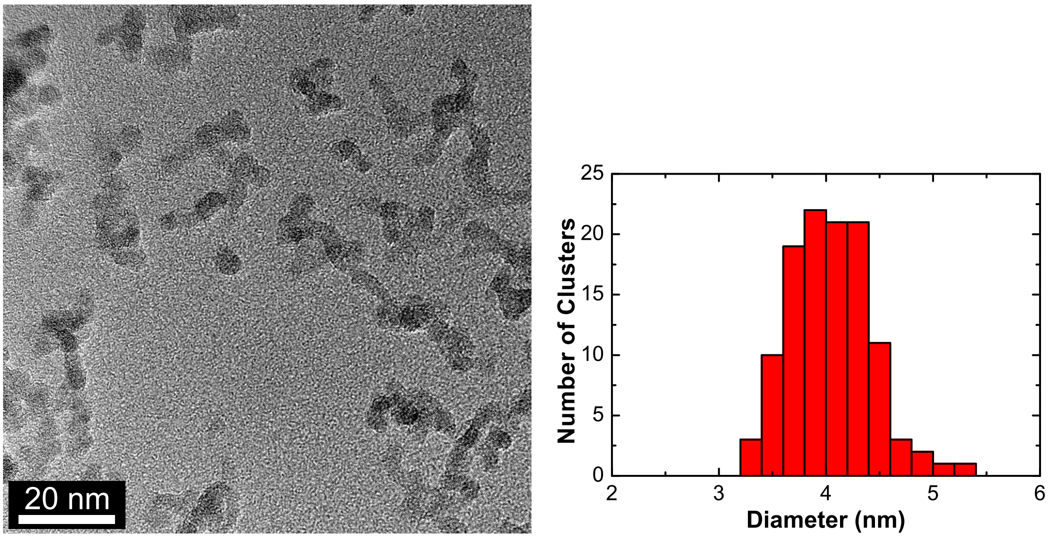

FIG. 5.31: (a) TEM image and (b) size distribution of titanium oxide nanoclusters deposited with pulsed DC, using an average power of 50 W, an argon gas flux of 108 SCCM, a pulsing frequency of 22 kHz, a pulsing duty cycle of 50 %,and a deposition time of 7 s.

An SEM image of a typical titanium oxide sample is shown in figure 5.30. Overall the structure is similar to the silver nanocluster films that were shown before, but in the case of titanium some much smaller structures are visible. All other properties like the low mechanical stability and the deposition profile are the same as for silver. Of course, the titanium oxide nanocluster films are insulating, in contrast to the metallic silver.

On a smaller scale more differences to the silver clusters are visible. Figure 5.31a shows a TEM image of titanium oxide clusters. In contrast to silver, the clusters are obviously not evenly distributed, but agglomerated by surface diffusion and built into chains of clusters. Also, the clusters itself are not spherical but clearly show facets and are monocrystalline, which both are in contrast to the results for silver nanoclusters. A big problem for the interpretation of this data is the fact that the clusters oxidize after the deposition on the surface. This reaction yields a high energy output, which might excite the surface diffusion. Additionally, the recrystallization during the oxidation is probably the reason for the facets in the cluster shape.

The cluster size distribution shown in figure 5.31b was determined by manually measuring the size of the clusters in the TEM image. Separated clusters were counted as they are, and agglomerated clusters in chains were counted if it was possible to estimate the size of a single cluster. The resulting distribution is quite narrow with its maximum at 4 nm. Surprisingly, this value is independent of the Cluster Source parameters. Samples were prepared at

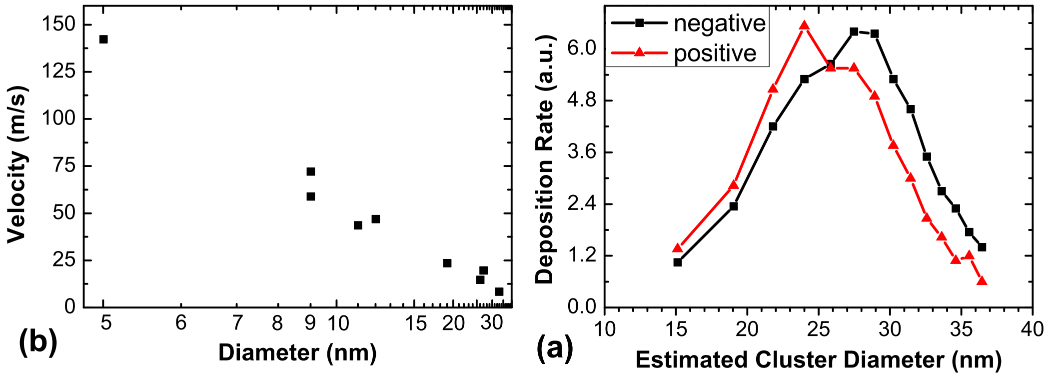

FIG. 5.32: (a) Velocity of titanium nanoclusters in dependence of their size, plotted on a reciprocal axis. (b) Size distribution of positive and negative titanium nanoclusters. The size was calculated by assuming a fixed speed of 50 m/s for the clusters.

different power, pressure, and also using continuous DC, but no variation in spatial and size distribution was observed. This behavior is a very unusual for GAS generated clusters, which in all other cases can be controlled easily with changes in pressure and power. The discrepancy can also be explained by the oxidation and subsequent diffusion and agglomeration on the substrate. It may lead to redistribution of the material into uniform-sized clusters, obfuscating the original cluster properties.

In order to investigate the titanium clusters before their oxidation, experiments using electrostatic deflection were used to estimate the size distribution, velocity, and charged portion of these clusters. All experiments were done using pulsed DC power, since the deposition rate of the deflected parts is only a fraction of the total beam, and thus would be too low to be measured for a continuous DC discharge. For this measurements the setup that was already used for silver cluster deflection experiments was used again (cp. figure 5.8). Three experiments were done: In the first experiment the cluster beam was deflected using a low voltage of ± 8 V, and then deposited on silicon substrates with a very low surface coverage. These samples were analyzed using SEM to determine the minimum and maximum cluster size found on them, depending on their distance from the neutral beam during deposition. From this, the cluster velocity could be calculated, the results are plotted in figure 5.32a. For this calculation it was assumed, that all cluster were generated as pure titanium and that during oxidation the amount of titanium atoms stayed constant. Additionally it is assumed that no agglomeration took place, which is grounded on the very low surface coverage and the low mobility of clusters on silicon. Using this assumptions, the cluster mass before oxidation was calculated and used to determine the velocity, which should correspond to the properties of the cluster when they leave the Cluster Source. The results concur with litera-

	Duty Cycle:		
Frequency:	50 %	65 %	80 %
20 kHz	60.2 % ± 1.2 %	62.4 % ± 2.2 %	63.5 % ± 8.5 %
40 kHz	53.7 % ± 0.2 %	58.3 % ± 1.2 %	67.5 % ± 3.1 %
60 kHz	56.6 % ± 1.2 %	64.6 % ± 5.4 %	72.3 % ± 0.9 %

Table 5.3: Charged portion of the titanium clusters in dependence of the pulse frequency and duty cycle.

ture about silver clusters [56], showing that the velocity of the cluster increases with smaller size.

This data was used in the second experiment, where the deflected cluster beam was directly analyzed using a QMB. The QMB was mounted at a fixed position, in that no clusters from the undeflected beam could reach it. Then the deflection voltage was varied between 0 and ± 70 V in steps of 5 V and the corresponding deposition rate on the QMB was measured. From this, a distribution of cluster depending on their charge, positive or negative, over the deflection voltage was obtained. Taking the results from before, the distribution over the cluster diameter could be determined, if a fixed speed was assumed. With an assumed velocity of 50 m/s, the distributions depicted in figure 5.32b was obtained. It should be kept in mind that the uncertainty in the diameter from this calculation is rather high, especially because the variation of velocity with cluster size is neglected. Still, the distribution itself and particularly the difference between the positive and negative charged clusters is quite certain. The different charged clusters were investigated with exactly the same setup and quartz position, only switching the voltages of the deflection plates. Also, taking the size of the area of the QMB into account, at the maximum point in the distribution cluster with a size of 25.4 to 30.6 nm are collected with negative charge, while at the maximum point for positively charged clusters the collected diameters are between 22.2 and 26.7 nm. For this reason, the difference in size of positive and negative clusters must be considered a true effect.

To investigate the influence of the pulsing parameters on the cluster charge, a third experiment was conducted, similar to one that was presented with silver already. First, without any deflection voltage, the whole beam intensity was measured. Subsequently, the maximum deflection voltage of ± 70 V was applied and only the neutral part of the beam was collected. From the comparison of this values the charged portion of the whole cluster beam could be determined. Table 5.3 shows this data for different pulsing frequencies and duty cycles. The experiment was repeated several times, because the values

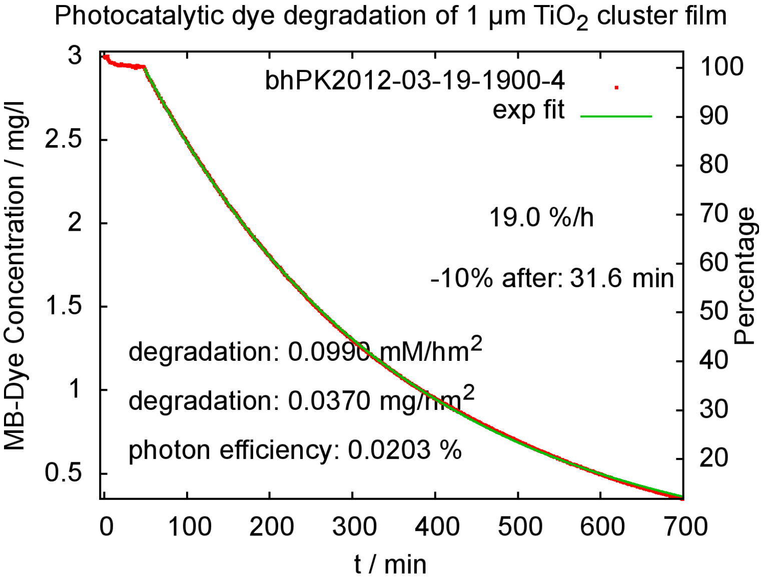

FIG. 5.33: Photocatalytic degradation of methylene blue dye by a titanium oxide cluster film. From Bodo Henkel.

are quite similar and do not show any strong trends. They are, however, quite stable and reproducible. Obviously the charged portion rises with increasing duty cycle in the investigated range. This result is not surprising, since a higher duty cycle means that ions are produced for a longer time and have shorter time for recombination. If so, a higher amount of argon ions is found in the Cluster Source, and thus also more ionizing collisions with cluster take place.

Titanium oxide samples can easily be deposited using the Cluster Source with very high rate and reproducibility. Yet, the exact characterization of the clusters that are generated is a complicated task, because of the high reactivity that hinders ex-situ analysis. Hence, a further investigation was not possible in the line of this work. It would require a new setup to allow cluster analysis without braking vacuum. And even then, the samples properties do not reflect the cluster properties in all aspects anyhow. At this point, two separate problems have to be explored: On the one hand the titanium clusters and their generation in the Cluster Source, since the knowledge about the basic processes might help to optimize the deposition process. On the other hand the titanium oxide samples already show huge potential for applications and should be inspected separately, even if the growth process is not yet completely understood.

5.4.4 Application in Photocatalysis

One possible application of nanocluster lies in the form of porous thin films for chemical catalysis. Here, the huge surface area of such samples offers new possibilities in comparison to bulk films. In case of titanium oxide layers, photocatalysis is the most promising field. Closed thin films, and also suspensions of particles, of titanium oxide have already proven useful for the photocatalytic degradation of industrial dyes [10]. This process disintegrates dye molecules that are soluted in water, in order to clean industrial sewage. UV-light is needed to excite electrons to the conduction band in the titanium oxide layer, and subsequently the electrons and electron holes can break bonds in molecules. It is also possible that they create hydroxyl radicals from the surrounding water, which in turn can degrade organic molecules. Depending on the targeted molecule, some or all of these processes may help in the degradation. A standard benchmark system to for photocatalytic experiments is the industrial dye methylene blue.

Several titanium oxide nanocluster samples were produced and their photocatalytic activity was investigated. These experiments were done in cooperation with Bodo Henkel from our group, who also did the photocatalytic measurements. The setup for this analysis consisted of a cuvette, a holder for the photocatalytic sample inside this cuvette, a UV-light source for excitation, and an optical transmission spectrometer to monitor the residue methylene blue concentration. At the beginning of the measurement, the cuvette was filled with a defined methylene blue solution. It is known, that the concentration of methylene blue can be easily determined using a transmission spectrometer, as the absorbance is directly proportional to the dye concentration [1]. This was done through the whole experiment to observe the degradation. At the beginning of the measurement, the sample was mounted inside the cuvette and left for some time without UV-light, to wait for the methylene blue concentration to settle. Such an experiment is shown in figure 5.33, where the methylene blue concentration is plotted against time. In the first minutes, the methylene blue is adsorbed on the sample, which also decreases the concentration in the solution, but is not the desired photocatalytic effect. Once the concentration reaches a stable value, the UV-light is turned on and the actual photocatalysis begins.

From the time evolution of the methylene blue concentration that is obtained by this, the degradation rate can be calculated, which is an important value for comparing different materials. Also the photon efficiency, that is the portion of the UV-light that started a degradation reaction, is often used to evaluate the performance of a sample. Titanium oxide nanocluster layers exhibit degradation rates and photon efficiencies in line with bulk titanium oxide films. Future optimization might even increase their performance and surpass the classical closed films. Another promising sample structure is a composite, where a nanocluster layer is deposited on top of bulk titanium oxide. Yet, for future applications still the low mechanical stability of the cluster layers is a major problem. This is especially true for catalytic samples, because here it is impossible to use a matrix or coating for stabilization, since the cluster surface is the functional feature. In a real world example the catalyst would reside inside a pipe for extensive time, and would be destroyed by the water stream alone. However, they would be fit to be used for cleaning of air, since no such mechanical work is expected in this case. Additionally, cluster layers help to understand the basic processes during the photocatalysis. In particular, the small and variable size of the the clusters allows to probe diffusion lengths of the charge carriers inside the titanium oxide. At the same time, the influence of the surface area can also be investigated with this system. For further reading, a publication about the measurement technique by Henkel et al. [viii] is recommended. Also, more detailed discussions of the photocatalytic performance of titanium oxide clusters and of bulk-cluster composite films are published by Henkel et al. [ix].

Summary and Outlook

In this work several different aspects of gas phase cluster aggregation have been investigated. To this end, two new experimental setups were developed, designed and constructed. The gas phase aggregation technique is an interesting technique, which is promising for future applications in many fields. However, not all processes during the cluster formation are fully understood yet. This makes it a very important topic for applied research. A particularly interesting process is the embedding of such clusters into a matrix material. Here, we have chosen a plasma-polymer, because its deposition is a suitable model system for the combination of gas phase cluster aggregation and other plasma based deposition methods. Also the used precursor, hexamethyldisiloxane (HMDSO), is widely used and its properties are known already. For similar reasons, silver was used for the metallic nanoparticles. It was already known that nanocluster generation is possible, and also as noble metal it does not react strongly with oxygen and nitrogen, enabling easy analysis out of vacuum. Accordingly, the investigation could focus on the new properties that were introduced by the embedded nanoclusters.

The first approach to deposit this composite material was the direct combination of both processes in one plasma. Therefore, a system to create a controlled precursor flow and inject it into a magnetron plasma was built. This Open (Cluster) Source was an uncommon design, which nevertheless proved to be a valuable tool to approximate the behavior of a closed gas aggregation cluster source (GAS). In contrast to most other designs, the Open Source was not an enclosed vessel, but consisted just of the injection system that was mounted in an usual vacuum chamber. The main advantage at this point was the ability to use various plasma diagnostic techniques, to gain insight into the cluster formation process.

It was used to create nanoclusters with tailorable size distribution, which mainly depend on the gas pressure and composition. Cluster with sizes between 5 and 10 nm were deposited, by changing the gas flow of argon and helium into the magnetron plasma. At this point, the influence of helium was surprising, as a higher helium flux led to bigger clusters, which was the opposite of what would be expected for a closed GAS. The reason for this behavior is thought to be the open design in combination with the position of helium injection. In the next step, the precursor for plasma polymerization was injected into the magnetron plasma, leading to the formation of silver-$Si_XO_YC_ZH$ nanocomposite thin films. Using this method, samples were created and analyzed to understand the interaction between the two deposition processes. It was found that the silver content of the samples can be easily tuned in a wide range. However, the silicon and oxygen content of the matrix was constant, and mainly independent of the deposition parameters. With an additional injection of oxygen, the matrix composition would have been also tailorable. Since the sputtering process already competed with polymer growth on the target, which threatens to stop the discharge, an added oxygen gas flux would have surely prevented the discharge for most parameters.

To cope with this problem, a new closed GAS was developed, designed, and constructed. Here, the magnetron with the gas injection for metal cluster formation was fit into a separate volume, which was only connected to the main deposition chamber by a small orifice. In this volume, the metal nanoclusters were grown and directed only into the chamber, after their aggregation process was already complete. In contrast to most other designs of GAS, it did not use water or liquid nitrogen cooling, but relied on the inert gas flux for cooling, which led to a very simple, yet effective, source. This Cluster Source was then characterized by analyzing different aspects of the produced silver nanoclusters. Subsequently, the desired nanocomposites were deposited by growing the plasma-polymer during the cluster deposition. In this setup, it was possible to separately control the discharge power and argon pressure for the plasma-polymerization, without disturbing the cluster growth. Furthermore, oxygen could be led into the secondary plasma, which enabled the tuning of the silicon and oxygen content of the polymer matrix. Several nanocomposite samples were deposited with this system, and were analyzed with a focus on their optical properties.

Both deposition techniques, the gas phase cluster aggregation and the plasma polymerization, were not used in this working group before. Now these two new techniques are established, and a deposition chamber to produce samples with these is built up. Other projects already used a second Cluster Source, that was built from this design. Also, the plasma polymerization was used in a different project as a barrier layer. In this case, the deposition was done in the system that was built for this work.

In the final part of the work, a derivative of gas phase cluster aggregation was investigated: The reactive cluster formation. Only few materials can be used in a classical gas phase cluster aggregation process, because a certain minimum sputtering yield and nucleation seed stability is required. For materials like cobalt and titanium this values are too low to allow cluster production in the Cluster Source. However, if a reactive gas, for example oxygen or nitrogen, is admixed to the argon flow, cluster production is easily possible. The needed reactive gas fluxes for this effect to work are in the range of 0.03 % to 0.2 % of the inert gas flux. Many experiments using titanium and oxygen were dedicated to understand and explain this effect, and to make it viable for sample deposition. In conclusion the main influence of reactive gas is the stabilization of the nucleation seeds, preventing them from dissociating, and thus allowing stable cluster production.

When the discharge power was switched from continuous DC to pulsed DC, a huge increase in cluster production rate was discovered for titanium. Its high rate was completely unforeseen, and surpassed even the rates known from metals with high sputtering yields, such as silver and copper. Further investigation of this effect led to the model, that the partial oxidation of the target can lead to sputtering of titanium-oxygen dimers, which already constitute a nucleation seed. Consequently, the rate-limiting three-body-collision is not needed for nucleation seed formation anymore, allowing much more efficient cluster growth.

Also this technique was used to deposit samples for a cooperation with a different project. The high surface area of the titanium oxide cluster films, and the possibility to easily create samples with a thickness in the order of microns, made them interesting for photocatalysis.

Overall, two new techniques for cluster and nanocomposite deposition were developed and investigated in this work. Their usefulness was proven not only by the creation of new materials, but also by other projects that utilize this new techniques. Lastly, a previous unknown effect that can be exploited for rapid cluster deposition has been found and explored. Also this technique was immediately employed in cooperation with another project for sample deposition, even though some open questions remain about the basics of this effect and require a continued study.

Appendix

Acknowledgements

I would like to thank Prof. Dr. Franz Faupel for the opportunity to work in his group. His guidance and advice, but also the thrust in my work, helped me greatly during my research.

Dr. Vladimir Zaporojtchenko deserves praise and thanks for his supervision of my work, but unfortunately he is not there to receive it anymore. He left us suddenly and unexpected, and thus will forever be remembered as the friendly and lively man he was. Apart from his job as our supervisor, he also fulfilled the role of a good friend. At every possible possibility he discussed, not only the recent topics of our research, but anything from history, politics, or personal matters. By this, he grow much too close to let go of him easily.

I would also like to express my thanks to Dr. Thomas Strunskus, for his supervision and cooperation in all parts of this work. Many thoughts and arguments from him helped me a lot, especially for the preparation of our publications.

For our continuous cooperation I am grateful to Prof. Dr. Kersten and his group, particularly Sven Bornholdt and Dr. Maik Fröhlich. The plasma physics view on the joined projects was always a valuable addition.

Also Oleksandr Polonskyi and Prof. Dr. Biedermann from Prague earned my thankfulness. The cooperation with them was a very pleasent experience, because of their active and friendly nature.

I thank Prof. Dr. Lorenz Kienle and his group for their help in all investigations with TEM analysis. Especially Dr. Venkata Sai Kiran Chakravadhanula has offered his help in many different occasions and thus contributed a great deal in my research. Also Dr. Ulrich Schürmann, Victor Hrkac, Burak Erkartal and the rest of the group deserve my thanks for their cooperation.

Prof. Dr. Es-Souni and Salah Habouti from the Fachhochschule Kiel have my thanks for their help and cooperation with SEM measurements and discussions.

I would like to also thank Prof. Dr. Rainer Hippler, Marina Ganeva, and the rest of their group from Greifswald for their cooperation in the joined project.

Dr. Jebril Seid and David Haffner deserve my thanks for their help with SEM measurements, which data was a significant part of this work.

Also Viktor Schneider contributed greatly by doing SEM analysis, for this I would like to thank him, as well as for the friendly and calm atmosphere in our joined office.

I would like to deeply thank my long term student assistant Maike Wegner, who was not only always a diligent and thrustworthy worker, but also a good friend and perfect confectioner. The bachelor's thesis that she completed under my supervision was another proof of her hard and independent work.

Alexander Hinz is the second student assistant, who I owe greatly. His excellent knowledge, ambition, and precision made him invaluable in the time he was working with me.

I would not only like to thank Bodo Henkel for the fruitful cooperation, but also for his continuous help in all sideline activity of the group.

Also Nisreen Alissawi has my thanks for our joined project and her driving nature, that lead to a very efficient teamwork.

I thank Stefan Rehders for his help by technical drawings, coordination with the workshop and help with every problem I have encountered during my work. Without him, probably nothing would be constructed or brought to function. Furthermore, his direct nature made him a pleasant discussant.

Also to Christoph Ochmann I am thankful for his help with all kinds of mechanical problems. Additionally, he was a very good table-neighbor to have, as his friendly way and help also outside of the work were invaluable at times.

Rainer Kloth has my thanks for his work in keeping our computers alive, as well as bringing new life to all kinds of electronics, that were needed during my research. I always liked to discuss questions of electronics and technology with him, which did not only cover purely research related topics. I deeply wish him to get well soon, and hope the best for his complete recovery.

Prof. Dr. Klaus Rätzke deserves praise for his omnipresent cheeriness and just as ubiquitous council in all questions of science and beyond.

I thank Tomislav Hrkac, Muhammad Qasim Shaikh and Christina Pakula for the wonderful time in our joined offices. All your help, opinions, ideas, and general discussions will stay as good memories.

Of course I would also like to thanks the people from our and the neighboring groups, that made the stay at the Institute a nice experience. My special thanks to Björn Gojdka, Christian Ohrt, Ingo Paulowicz, Xin Jin, Arnim Schuchardt, Tönjes Koschine, Sebastian Zabel, Sören Kaps, Dr. Yogendra Kumar Mishra, Kerstin Meurisch, Prof. Dr. Rainer Adelung, Stephan Harms, Christian Pochstein, Alexander Bartsch, Sebastian Wille, Jian Xiong, Amit Kulkarni, and Amir Mohammad Ahadi.

The most important person in creation of this thesis is of course my fiance Sri Wahyuni Basuki. She patiently endured the months of writing with less time for her, and at the same helped me with it in every way possible.

At last, also my brother, sister, and mother helped, again, greatly with their support during a thesis in the line of my research, and for this I am truly grateful.

Bibliography

1. *DIN 52980: Photocatalytic activity of surfaces – Determination of photocatalytic activity by degradation of methylene blue*. Beuth Verlag GmbH, Berlin, 2008.

2. M. Aktik, Y. Segui, and B. Ai. A new polymer insulated gate field-effect transistor. *Journal of Applied Physics*, 51(9):5055, 1980.

3. V. Amendola, O. M. Bakr, and F. Stellacci. A Study of the Surface Plasmon Resonance of Silver Nanoparticles by the Discrete Dipole Approximation Method: Effect of Shape, Size, Structure, and Assembly. *Plasmonics*, 5(1):85–97, Jan. 2010.

4. a.N. Banerjee, R. Krishna, and B. Das. Size controlled deposition of Cu and Si nanoclusters by an ultra-high vacuum sputtering gas aggregation technique. *Applied Physics A*, 90(2):299–303, Sept. 2007.

5. F. Baletto, C. Mottet, and R. Ferrando. Molecular dynamics simulations of surface diffusion and growth on silver and gold clusters. *Surface Science*, 446(1-2):31–45, Feb. 2000.

6. C. Bohren and D. R. Huffman. *Absorption and Scattering by Small Particles*. Wiley, New York, 1983.

7. C. Bourreau, Y. Catherine, and P. Garcia. Glow discharge deposition of silicon dioxide and aluminum oxide films: A kinetic model of the surface processes. *Plasma Chemistry and Plasma Processing*, 10(2):247–260, June 1990.

8. J. W. Bradley and T. Welzel. Physics and phenomena in pulsed magnetrons: an overview. *Journal of Physics D: Applied Physics*, 42(9):093001, May 2009.

9. J. E. Campana. Elementary theory of the quadrupole mass filter. *International Journal of Mass Spectrometry and Ion Physics*, 33(2):101–117, 1980.

10. O. Carp. Photoinduced reactivity of titanium dioxide. *Progress in Solid State Chemistry*, 32(1-2):33–177, 2004.

11. A. Chen and P. Holt-Hindle. Platinum-based nanostructured materials: synthesis, properties, and applications. *Chemical reviews*, 110(6):3767–804, June 2010.

12. S. Chernov, Y. Fedorov, and V. Zakharov. Surface tension of silver in different media. *Journal of Physics and Chemistry of Solids*, 54(8):963–966, Aug. 1993.

13. A. Choukourov, I. Gordeev, D. Arzhakov, A. Artemenko, J. Kousal, O. Kylián, D. Slavínská, and H. Biederman. Does Cross-Link Density of PEO-Like Plasma Polymers Influence their Resistance to Adsorption of Fibrinogen? *Plasma Processes and Polymers*, 9(1):48–58, Jan. 2012.

14. D. Depla, S. Heirwegh, S. Mahieu, J. Haemers, and R. De Gryse. Understanding the discharge voltage behavior during reactive sputtering of oxides. *Journal of Applied Physics*, 101(1):013301, 2007.

15. K. Ebihara and T. Fujishima. Silicon oxide film preparation by RF plasma-enhanced MOCVD using hexamethyldisiloxane. *Plasma Sources Science . . .* , 2(1):14, 1993.

16. J. Fang, H. Chen, and X. Yu. Studies on plasma polymerization of hexamethyldisiloxane in the presence of different carrier gases. *Journal of Applied Polymer Science*, 80(9):1434–1438, May 2001.

17. F. Faupel, V. Zaporojtchenko, T. Strunskus, and M. Elbahri. Metal-Polymer Nanocomposites for Functional Applications. *Advanced Engineering Materials*, 12(12):1177–1190, 2010.

18. B. Finke, F. Hempel, H. Testrich, a. Artemenko, H. Rebl, O. Kylián, J. Meichsner, H. Biederman, B. Nebe, K.-D. Weltmann, and K. Schröder. Plasma processes for cell-adhesive titanium surfaces based on nitrogen-containing coatings. *Surface and Coatings Technology*, 205:S520–S524, July 2011.

19. M. Ganeva, a.V. Pipa, and R. Hippler. The influence of target erosion on the mass spectra of clusters formed in the planar DC magnetron sputtering source. *Surface and Coatings Technology*, Oct. 2012.

20. E. J. Garboczi, K. A. Snyder, J. F. Douglas, and F. Thorpe. Geometrical percolation threshold of overlapping ellipsoids. *Physical Review E*, 52(1):819–828, 1995.

21. T. Garcia-Perez, E. Rodriguez, E. Bittencourt, and Z. Jova. ACTIVATION OF HMDSO THIN FILMS WITH LOW PRESSURE ARGON PLASMA AND VACUUM ULTRAVIOLET RADIATION. *Latin American Applied Research*, 25(42):19–25, 2012.

22. B. Gojdka, V. Hrkac, T. Strunskus, V. Zaporojtchenko, L. Kienle, and F. Faupel. Study of cobalt clusters with very narrow size distribution deposited by high-rate cluster source. *Nanotechnology*, 22(46):465704, Nov. 2011.

23. M. Gracia-Pinilla, E. Martínez, G. Vidaurri, and E. Pérez-Tijerina. Deposition of Size-Selected Cu Nanoparticles by Inert Gas Condensation. *Nanoscale Research Letters*, 5(1):180–188, 2010.

24. H. Haberland, M. Karrais, M. Mall, and Y. Thurner. Thin films from energetic cluster impact: A feasibility study. *J. Vac. Sci. Technol. A*, 10(5):3266–3271, 1992.

25. H. Haberland, M. Mall, M. Moseler, Y. Qiang, T. Reiners, and Y. Thurner. Filling of micron-sized contact holes with copper by energetic cluster impact. *Journal of Vacuum Science & Technology A: Vacuum, Surfaces, and Films*, 12(5):2925, Sept. 1994.

26. W. M. Haynes and D. R. Lide. *CRC Handbook of Chemistry and Physics*. CRC Press, Boca Raton, 91 edition, 2010.

27. A. Heilmann. *Polymer Films with Embedded Metal Nanoparticles*. Springer Verlag, Berlin, 2003.

28. H. Hirai, H. Sekiguchi, S. Miyata, and S. Kobayashi. Tellurium thin-film transistor deposited on polyester film having plasma polymerized films on double-layered gate insulators. *Applied Physics Letters*, 50(13):818, 1987.

29. A. A. Howling, L. Sasonnens, J.-L. Dorier, and C. Hollenstein. Time-Resolved Measurements of Highly Polymerized Negative Ions in Radio Frequency Silane Plasma Deposition Experiments. *Journal of Applied Physics*, 75:1340–1353, 1994.

30. D. Ildebrandt, R. Manns, and H. Düsterhöft. The mean kinetic energy of sputtered atoms as a function of the angle of emission. *physica status solidi (a)*, 64:K27, 2006.

31. S. W. Ing and W. Davern. Glow Discharge Formation of Silicon Oxide and The Deposition of Silicon Oxide Thin Film Capacitors by Glow Discharge Techniques. *Journal of The Electrochemical Society*, 112(3):284, 1965.

32. Y. Inoue and O. Takai. Spectroscopic studies on preparation of silicon oxide films by PECVD using organosilicon compounds. *Plasma Sources Science and Technology*, 5:339, 1999.

33. M. Isichenko. Percolation, statistical topography, and transport in random media. *Reviews of Modern Physics*, 64(4), 1992.

34. A. Jiang, N. Awasthi, A. Kolmogorov, W. Setyawan, A. Börjesson, K. Bolton, A. Harutyunyan, and S. Curtarolo. Theoretical study of the thermal behavior of free and alumina-supported Fe-C nanoparticles. *Physical Review B*, 75(20):205426, May 2007.

35. P. V. Kashtanov, B. M. Smirnov, and R. Hippler. Magnetron plasma and nanotechnology. *Physics-Uspekhi*, 50(5), 2007.

36. H. Kersten, G. M. W. Kroesen, and R. Hippler. On the energy influx to the substrate during sputter deposition of thin aluminum films. *Thin Solid Films*, 332:282, 1998.

37. A. Kramida, Y. Ralchenko, and J. Reader. *NIST Atomic Spectra Database (ver. 5.0)*. National Institute of Standards and Technology, Gaithersburg, MD, 2012.

38. U. Kreibig. Electronic properties of small silver particles: the optical constants and their temperature dependence. *Journal of Physics F: Metal Physics*, 4(7):999–1014, July 1974.

39. U. Kreibig and M. Vollmer. *Optical Properties of Metal Clusters*. Springer Verlag, Berlin, 1995.

40. T. Kubart, D. Depla, D. M. Martin, T. Nyberg, and S. Berg. High rate reactive magnetron sputter deposition of titanium oxide. *Applied Physics Letters*, 92(22):221501, 2008.

41. T. Kubart, R. Schmidt, M. Austgen, T. Nyberg, a. Pflug, M. Siemers, M. Wuttig, and S. Berg. Modelling of sputtering yield amplification in serial reactive magnetron co-sputtering. *Surface and Coatings Technology*, 206(24):5055–5059, Aug. 2012.

42. D. Lundin, M. Stahl, H. Kersten, and U. Helmersson. Energy flux measurements in high power impulse magnetron sputtering. *Journal of Physics D: Applied Physics*, 42(18):185202, Sept. 2009.

43. A. Marek, J. Valter, S. Kadlec, and J. Vyskočil. Gas aggregation nanocluster source — Reactive sputter deposition of copper and titanium nanoclusters. *Surface and Coatings Technology*, 205:S573–S576, July 2011.

44. N. Matsunami, Y. Yamamura, and Y. Itikawa. Energy dependence of the ion-induced sputtering yields of monatomic solids. *Atomic Data and . . .* , 31(1), 1984.

45. G. Mie. Beiträge zur Optik trüber Medien, speziell kolloidaler Metallösungen. *Annalen der Physik*, 25(3):377, 1908.

46. R. P. Mota, D. Galvão, S. F. Durrant, M. A. De Moraes, S. de Oliveira Dantas, and M. Cantão. HMDSO plasma polymerization and thin film optical properties. *Thin Solid Films*, 270(1-2):109–113, Dec. 1995.

47. J. F. Moulder, W. F. Stickle, P. E. Sobol, and K. D. Bomben. *Handbook of X-ray Photoelectron Spectroscopy*. Perkin-Elmer, Eden Prairie, Minnesota, 1992.

48. J. Musil, J. Lestina, J. Vlcek, and T. Tölg. Pulsed dc magnetron discharge for high-rate sputtering of thin films. *Journal of Vacuum Science & Technology A: Vacuum, Surfaces, and Films*, 19(2):420, 2001.

49. C.-W. Nan, Y. Shen, and J. Ma. Physical Properties of Composites Near Percolation. *Annual Review of Materials Research*, 40(1):131–151, June 2010.

50. V. S. Nguyen, J. Underhill, S. Fridmann, and P. Pan. Plasma Organosilicon Polymers: deposition, characterization, and Application in Multilayer Resist. *Journal of The Electrochemical Society*, 132(8):1925, 1985.

51. M. Ohring. *Materials Science of Thin Films*. Academic Press, London, 2 edition, 2002.

52. Y. Osada and A. Mizumoto. Preparation and electrical properties of polymeric copper phthalocyanine thin films by plasma polymerization. *Journal of Applied Physics*, 59(5):1776, 1986.

53. K. Oura, V. Lifshits, A. Saranin, A. Zotov, and M. Katayama. *Surface Science: An Introduction*. Springer Verlag Berlin Heidelberg, Heidelberg, 2003.

54. P. Piseri, A. Podesta, E. Barborini, and P. Milani. Production and characterization of highly intense and collimated cluster beams by inertial focusing in supersonic expansions. *Review of Scientific Instruments*, 72(5):2261, 2001.

55. H.-U. Poll, J. Meichsner, M. Arzt, M. Friedrich, R. Rochotzki, and E. Kreyβig. Optical properties of plasma polymer films. *Surface and Coatings Technology*, 59(1-3):365–370, Oct. 1993.

56. O. Polonskyi, P. Solař, O. Kylián, M. Drábik, A. Artemenko, J. Kousal, J. Hanuš, J. Pešička, I. Matolínová, E. Kolíbalová, D. Slavínská, and H. Biederman. Nanocomposite metal/plasma polymer films prepared by means of gas aggregation cluster source. *Thin Solid Films*, 520(12):4155–4162, Apr. 2012.

57. V. N. Popok, I. Barke, E. E. Campbell, and K.-H. Meiwes-Broer. Cluster–surface interaction: From soft landing to implantation. *Surface Science Reports*, 66(10):347–377, Oct. 2011.

58. S. Pratontep, S. J. Carroll, C. Xirouchaki, M. Streun, and R. E. Palmer. Size-selected cluster beam source based on radio frequency magnetron plasma sputtering and gas condensation. *Review of Scientific Instruments*, 76(4):045103, 2005.

59. M. Rai, A. Yadav, and A. Gade. Silver nanoparticles as a new generation of antimicrobials. *Biotechnology advances*, 27(1):76–83, 2009.

60. L. Reimer. *Scanning electron microscopy: physics of image formation and microanalysis*. Berlin, 1998.

61. D. Salz, R. Lamber, M. Wark, A. Baalmannb, and N. Jaegera. Metal clusters in plasma polymer matrices Part II. Silver clusters. *Physical Chemistry Chemical Physics*, 1(1):4447–4451, 1999.

62. S. Sapieha, C. a. Ferguson, R. P. Beatson, and M. R. Wertheimer. Deposition of organosilicone plasma polymer onto cellulose networks. *Plasma Chemistry and Plasma Processing*, 9(2):225–234, June 1989.

63. K. Sattler, J. Mühlbach, and E. Recknagel. Generation of metal clusters containing from 2 to 500 atoms. *Physical Review Letters*, 45(10):821–824, 1980.

64. H. Schreiber, M. Wertheimer, and A. Wrobel. Corrosion protection by plasma-polymerized coatings. *Thin Solid Films*, 72:487–493, 1980.

65. M. Seah and W. Dench. Quantitative electron spectroscopy of surfaces: A standard data base for electron inelastic mean free paths in solids. *Surface and Interface analysis*, 1(1):1, 2004.

66. Y. Segui and B. Ai. Microelectronic applications of plasma-polymerized films. *Thin Solid Films*, 50:321–324, May 1978.

67. I. Shyjumon, M. Gopinadhan, O. Ivanova, M. Quaas, H. Wulff, C. a. Helm, and R. Hippler. Structural deformation, melting point and lattice parameter studies of size selected silver clusters. *The European Physical Journal D*, 37(3):409–415, Nov. 2006.

68. D. L. Smith. *Thin-Film Deposition Principles & Practice*. McGraw-Hill, New York, 1995.

69. C. Soll. *Plasmapolymerisation von Hexamethyldisiloxan zur Abscheidung von quarzähnlichen Schichten bei gepulster Leistungszufuhr*. Doktorarbeit, Bergische Universität Wupertal, 2000.

70. M. Stahl. Energiestrommessungen in Prozessplasmen. 2009.

71. V. Stranak, S. Block, S. Drache, Z. Hubicka, C. A. Helm, L. Jastrabik, M. Tichy, and R. Hippler. Size-controlled formation of Cu nanoclusters in pulsed magnetron sputtering system. *Surface and Coatings Technology*, 205(8–9):2755–2762, 2011.

72. J. Sun and S. Simon. The melting behavior of aluminum nanoparticles. *Thermochimica Acta*, 463(1-2):32–40, Oct. 2007.

73. S. Tahara, M. Yoshii, and S. Oka. Electrochemical reference electrode for the ion-selective field effect transistor. *Chemistry Letters*, 11:307–310, 1982.

74. J. a. Theil, J. G. Brace, and R. W. Knoll. Carbon content of silicon oxide films deposited by room temperature plasma enhanced chemical vapor deposition of hexamethyldisiloxane and oxygen. *Journal of Vacuum Science & Technology A: Vacuum, Surfaces, and Films*, 12(4):1365, July 1994.

75. J. A. Thornton. Substrate heating cylindrical magnetron sputtering sources. *Thin Solid Films*, 54:23–31, 1978.

76. P. K. Tien, S. RivaSanseverino, R. J. Martin, and G. Smolinsky. Two-layered construction of integrated optical circuits and formation of thin-film prisms, lenses, and reflectors. *Applied Physics Letters*, 24(11):547, 1974.

77. F. Voigt, R. Brüggemann, T. Unold, F. Huisken, and G. Bauer. Porous thin films grown from size-selected silicon nanocrystals. *Materials Science and Engineering: C*, 25(5-8):584–589, Dec. 2005.

78. K. Wagatsuma and K. Hirokawa. Effects of helium addition to an argon glow discharge plasma on emission lines of sputtered particles. *Analytical Chemistry*, 60(7):702–705, Apr. 1988.

79. R. K. Waits. Planar Magnetron Sputtering. *J. Vac. Sci. Technol.*, 15(2):179–187, 1978.

80. K. Wegner, P. Piseri, H. V. Tafreshi, and P. Milani. Cluster beam deposition: a tool for nanoscale science and technology. *Journal of Physics D: Applied Physics*, 39(22):R439–R459, Nov. 2006.

81. M. Wegner. *Untersuchung der Herstellung von Nanokompositen durch Plasmapolymerisation und Hochdruckmagnetronentladung*. Bachelorarbeit, Christian-Albrechts-Universität zu Kiel, 2010.

82. D. B. Williams and C. B. Carter. *Transmission Electron Microscopy - A Textbook for Materials Science*. Springer, New York, 2009.

83. Y. Xia, N. J. Halas, and G. Editors. Shape-Controlled Surface Plasmonic Nanostructures. 30(May), 2005.

84. T. Yamaki, M. Sekiya, and K. Tanaka. A theoretical study on lower electronic states of CoN. *Chemical Physics Letters*, 376(3-4):487–492, July 2003.

85. H. Yasuda. *Plasma Polymerization*. Academic Press, New York, 1985.

86. V. Zaporojtchenko, K. Behnke, T. Strunskus, and F. Faupel. Condensation coefficients of noble metals on polymers: a novel method of determination by x-ray photoelectron spectroscopy. *Surface and Interface Analysis*, 30(1):439–443, Aug. 2000.

87. S. Zhao, S. Wang, and H. Ye. Size-dependent melting properties of free silver nanoclusters. *Journal of the Physical Society of Japan*, 70(10):2953–2957, 2001.

88. J. F. Ziegler, J. P. Biersack, and M. D. Ziegler. *SRIM - The Stopping and Range of Ions in Matter*. SRIM Co., Chester, Maryland, 2008.

List of publications

i. T. Peter, M. Wegner, V. Zaporojtchenko, T. Strunskus, S. Bornholdt, H. Kersten and F. Faupel.
"*Metal/polymer nanocomposite thin films prepared by plasma polymerization and high pressure magnetron sputtering*".
Surf. Coat. Technol. 205, 38 (2011).

ii. T. Peter, O. Polonskyi, B. Gojdka, A. M. Ahadi, T. Strunskus, V. Zaporojtchenko, H. Biederman and F. Faupel.
"*Influence of reactive gas admixture on transition metal cluster nucleation in a gas aggregation cluster source*".
J. Appl. Phys. 112, 114321 (2012).

iii. T. Peter, S. Rehders, U. Schürmann, T. Strunskus, V. Zaporojtchenko and F. Faupel.
"*High Rate Deposition System for Metal-Cluster / SiOxCyHz -Polymer Nanocomposite Thin Films*".
J. Nanopart. Res. 15, 1710 (2013).

iv. S. Bornholdt, T. Peter, T. Strunskus, V. Zaporojtchenko, F. Faupel and H. Kersten.
"*The method of conventional calorimetric probes - A short review and application for the characterization of nanocluster sources*".
Surf. Coat. Technol. 205, 388 (2010).

v. M. Ganeva, T. Peter, S. Bornholdt, H. Kersten, T. Strunskus, V. Zaporojtchenko, F. Faupel and R. Hippler.
"*Mass Spectrometric Investigations of Nano-Size Cluster Ions Produced by High Pressure Magnetron Sputtering*".
Contrib. Plasma Phys. 52, 881 (2012).

vi. O. Polonskyi, T. Peter, A. M. Ahadi, A. Hinz, T. Strunskus, V. Zaporojtchenko, H. Biederman and F. Faupel.
"*Huge increase in gas phase cluster generation by reactive pulsed DC sputtering*".
Submitted (2013).

vii. N. Alissawi, T. Peter, T. Strunskus, C. Ebbert, G. Grundmeier and F. Faupel.
"*Adjusting the silver ion release properties of Ag/PTFE nanocomposites by use of plasma-polymerized HMDSO barriers with different oxygen content*".
In preparation (2013).

viii. B. Henkel, S. Zabel, T. Peter, J. Xiong, T. Strunskus and F. Faupel.
"*Experimental and Methodical Review of Methylene Blue Degradation Test for Quantization of Photocatalytic Efficiency, Indicating Suggestions for Improvement Concerning the Existing Norm*".
In preparation (2013).

ix. B. Henkel, S. Zabel, T. Peter, O. Polonskyi, T. Strunskus and F. Faupel.
"*Comparison of Different Photocatalytic Behavior of Dense Pulsed DC Magnetron Sputtered versus Highly Porous Cluster Source TiO2 Thin Films, resulting in a Proposal of a Synergetic Composite Approach to TiO2 Thin Films for Photocatalysis*".
In preparation (2013).

x. A. Ahadi, V. Zaporojtchenko, T. Peter, O. Polonskyi, T. Strunskus and F. Faupel.
"*Role of reactive gas on stabilization of clusters deposition prepared by gas aggregation chamber*".
Submitted (2013).